8-8-2009

High-spin triaxial strongly deformed structures and quasiparticle alignments in 168Hf

Ram Babu Yadav

HIGH-SPIN TRIAXIAL STRONGLY DEFORMED STRUCTURES AND QUASIPARTICLE ALIGNMENTS IN ^{168}Hf

By

Ram Babu Yadav

A Dissertation
Submitted to the Faculty of
Mississippi State University
in Partial Fulfillment of the Requirements
for the Degree of Doctor of Philosophy
in Physics
in the Department of Physics & Astronomy

Mississippi State, Mississippi

August 2009

HIGH-SPIN TRIAXIAL STRONGLY DEFORMED STRUCTURES AND QUASIPARTICLE ALIGNMENTS IN ^{168}Hf

By

Ram Babu Yadav

Approved:

Wenchao Ma
Professor of Physics
(Director of Dissertation)

Jeff A. Winger
Professor of Physics
(Committee Member)

Anatoli Afanasjev
Associate Professor of Physics
(Committee Member)

James A. Dunne
Associate Professor of Physics
(Committee Member)

Radhakrishnan Srinivasan
Assistant Research Professor of
Agricultural & Biological Engineering
(Committee Member)

David L. Monts
Professor of Physics
(Department's Graduate Coordinator)

Lori M. Bruce
Associate Dean for Research & Graduate Studies

Name: Ram Babu Yadav

Date of Degree: August 8, 2009

Institution: Mississippi State University

Major Field: Physics

Major Professor: Dr. Wenchao Ma

Title of Study: HIGH-SPIN TRIAXIAL STRONGLY DEFORMED STRUCTURES AND QUASIPARTICLE ALIGNMENTS IN ^{168}Hf

Pages in study: 190

Candidate for Degree of Doctor of Philosophy

This dissertation research consists of two parts: (i) investigation of quasiparticle alignments at high-spins and (ii) identification of triaxial strongly deformed structures in ^{168}Hf. A γ-ray spectroscopy study was carried out, as well as lifetime measurements using the Doppler-shift Attenuation Method. Two data sets were obtained from experiments at Argonne National Laboratory employing the reaction ^{96}Zr(^{76}Ge, 4n). The decay γ-rays were measured with the Gammasphere Compton-suppressed Ge spectrometer array. A self-supporting ^{96}Zr foil ("thin target") was used in the first experiment, while in the second experiment the ^{96}Zr target material was evaporated onto a thick Au backing ("backed target" or "thick target") to stop the recoiling nuclei for lifetime measurements.

All previously known rotational bands have been extended to higher spins. Seven new normal-deformed bands, of which three are high-K bands, have been discovered. Neutron alignments were observed in all bands, and the proton alignments observed in several bands at the highest spin region (rotational frequency 0.55 - 0.6 MeV).

The results are interpreted within the framework of the cranked shell model (CSM). Intrinsic configurations for the new bands, up to six quasiparticles, are proposed. The co-existing coupling schemes, deformation and rotation alignment, involving identical orbitals at high spin are discussed for the high-K bands.

Possible decay pathways associated with three previously proposed candidates for triaxial strongly deformed (TSD) structures in ^{168}Hf have been investigated. The spin and excitation energy of the bandhead for the strongest band, TSD1, were determined approximately based on γ-ray coincidence relationships. Discrete links were established for the second band. The overall agreement between the observed properties of the bands and cranking calculations using the Ultimate Cranker code provides strong support for an interpretation where band TSD1 is associated with a TSD minimum, $(\varepsilon_2, \gamma) \sim (0.43, 20^\circ)$, involving the $\pi(i_{13/2})^2$ and the $\nu(j_{15/2})$ high-j orbitals. This constitutes the first identification of a TSD band in Hf isotopes, long-predicted by theoretical studies. The second band is understood as being associated with a near-prolate shape and a deformation enhanced with respect to the normal deformed bands. It is proposed to be built on the $\pi(i_{13/2}h_{9/2}) \otimes \nu(i_{13/2})^2$ configuration.

DEDICATION

To my parents, Ramsakhi Devi and Laxman Yadav, who supported, guided and loved me.

ACKNOWLEDGMENTS

This degree is not only mine, but also belongs to all my friends, instructors, and family members who have been there for me over the years.

First of all, I am most grateful to my advisor, Dr. Wenchao Ma, for his guidance, encouragement, support, and patience during my years at Mississippi State University. Personally, I would like to thank him for sharing his knowledge which has enriched my study in Nuclear Physics. His resourcefulness, keen constructiveness and wisdom were of immense importance for my achievement. I was pleased with the fact that he entrusted me with the flexibility to pursue my studies in my own style and methods. At crucial times, Dr. Ma has helped to keep me on the right track towards the completion of my dissertation, several talks and a recent paper. My dissertation committee members deserve much credit for their help, invaluable advice and encouragement.

I would like to acknowledge two former post-doctoral research associates, Dr. David G. Roux and Dr. Emmanuel Ngijoi-Yogo, for their informative and resourceful suggestions throughout this project. Dr. Roux, I miss those moments I shared with you during my early days at Mississippi State. Thank you for explaining the process of data analysis and the concept of gamma-ray spectroscopy. I would like to thank Dr. Ngijoi-Yogo for sharing his insights on lifetime measurement work. Thanks to my fellow ex-student, Dr. Yanci Zhang for his help, suggestions and expertise in making

the computer work properly. I also want to thank all the students of the nuclear group for good company, encouragement and spirit - Sergey Ilyushkin and Quarat-Ul-Ann Ijaz.

I would like to acknowledge other faculty members of the Physics Department for their cooperation. I would be failing in my duty if I did not mention the laboratory and administrative staff for all their hard work that they do day after day. Susan Galloway, I have appreciated your smile, constantly helping students with administration and for many friendly chats about life and the non-physics world. A sincere thanks goes out to our department veteran, Connie Vaughn who constantly made sure all students signed their offer letters in time. Robertsen Riehle, I greatly appreciate the patience shown by you when answering my silly Linux questions, solving all my computer problems, and for many friendly conversations about politics and life. The Physics Department is a much better place because of all of you.

Finally and most of all, I would like to thank my families for their constant love and support. My wife, Punita Goit and daughter, Rhea Yadav deserve special recognition. Obtaining a Ph.D. in Physics was not only difficult for me but also for my family. I am grateful that my wife has stood by me all these years. Without her support, I doubt that I would have successfully made it to the end. As I have watched my daughter grow from an infant to a happy, intelligent four year-old child, I have been inspired even more to complete this arduous journey. Thank you Punita and Rhea for being there for me during this ordeal.

TABLE OF CONTENTS

Page

Page

Page

Page

LIST OF TABLES

TABLE Page

LIST OF FIGURES

FIGURE Page

Page

Page

Page

Page

Page

CHAPTER I

MOTIVATION OF THIS DISSERTATION RESEARCH

The experimental nuclear structure group at Mississippi State University has actively studied the normal and highly deformed structures in A $\simeq$ 152-170 heavy rare-earth region. The nucleus $^{168}Hf_{96}$ is one of the first nuclei studied up to spins above $30\hbar$. This nucleus, with Z=72 and N=96, is a typical mid-shell nucleus with stable quadrupole deformation and is a very good candidate for testing the shell model at high spin. There are two major previous studies for ^{168}Hf: one for normal deformed (ND) high spin states by E.M. Beck *et al.* [1] and another for superdeformed (SD) bands by our group [2]. Two experiments by our group, the first using a thin target and another using a thick target, were performed at the Argonne National Laboratory (ANL), USA. The current dissertation work is based on data analysis obtained from the same two experiments. Moreover, the goal of this work was three fold: (a) to study normal deformed high-spin structures in ^{168}Hf with both thin and thick target data, (b) to perform lifetime measurements using the Doppler Shift Attenuation Method (DSAM) for a normal deformed band with thick target data, and (c) to investigate possible decay pathways of three triaxial strongly deformed (TSD) bands with thin target data.

The previous experimental study of ^{168}Hf presented in Ref. [1] was performed at the Lawrence Berkeley National Laboratory, USA. In this experiment, high-spins states of ^{168}Hf were populated by the reaction ^{124}Sn(^{48}Ti, 4n) at beam energies of 210

and 215 MeV, using a beam provided by the 88-inch cyclotron. The target consisted of a stack of three tin foils of $\sim$0.45 mg/cm^2 stacked together as a target so that the evaporation residues recoiled into vacuum. The γ-rays emitted by the highly excited nuclei were measured with the Berkeley High Energy Resolution Array (HERA), which consisted of 21 Compton-suppressed Ge detectors. The detectors were gain matched on-line to compensate for the Doppler shifts of the rays. A total of $\sim$2.8 $\times 10^8$ three- and higher-fold events was recorded on tape of which approximately half came from the 4n channel. A level scheme of ^{168}Hf, shown in Figure 1.1, was extracted from this experiment. In this figure, an energy in parentheses indicates a tentative transition, and a spin in parentheses indicates that the multipolarity of the line could not be firmly determined. The positive-parity band crossing the ground-state band is the AB band. The two strongest negative-parity bands are AE and AF, respectively. This was also concluded by Chapman et al. [3]. In this notation, A, B, C and D are the lowest positive(unique)-parity single particle orbitals ($i_{13/2}$ neutrons for this nucleus) in the cranking model; E and F are the lowest two negative(natural)-parity orbitals (derived from the $h_{9/2}$ and $f_{7/2}$ neutrons for this nucleus). This labeling scheme will be described in Section 6.1 in more detail.

^{168}Hf is one of the best rigid rotors which can be populated at very high spins [1, 3]. Being a typical mid-shell and well-deformed nucleus, it is interesting that ^{168}Hf can exhibit rotational band structures ($E_\gamma \propto I$) without any reduction in collectivity up to spins above 30. The study of its normal deformed states has provided evidence for the occurence of both spin alignments and the validity of the coupling scheme in general. This nuclide also shows superdeformation at very high spin [2].

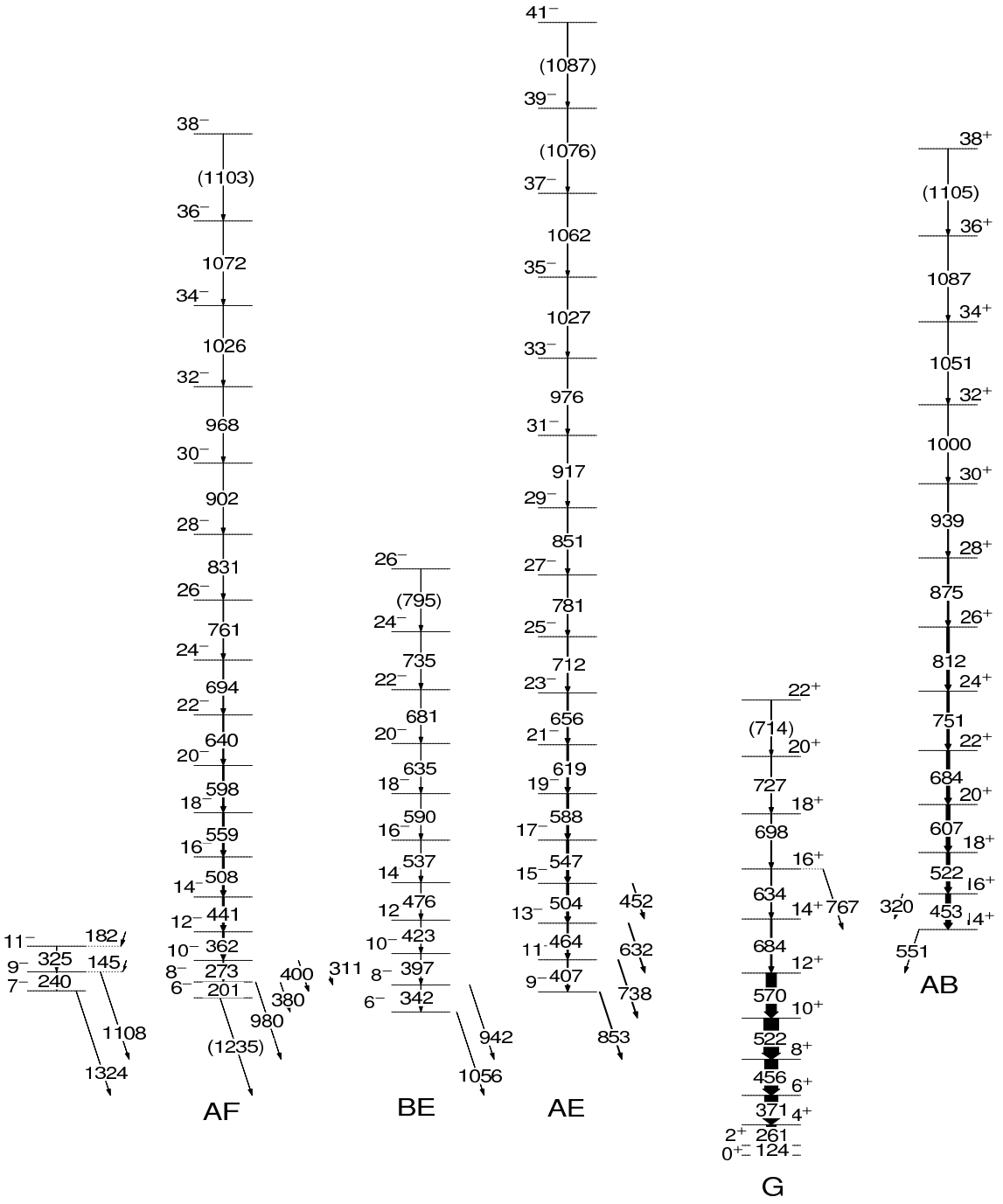

Figure 1.1: The level scheme of ^{168}Hf by E.M. Beck *at.el.* [1].

Detailed knowledge of the normal deformed states is crucial to understand the decay pathways of superdeformed states. These normal deformed high spin states in ^{168}Hf have previously been studied by E.M. Beck *et al.* [1].

In two previous studies [1, 4], an irregularity or second band crossing was observed and suggested to be caused by the $i_{13/2}$ or $h_{9/2}$ proton alignment. High-spin γ-ray spectroscopy in other isotopes [5-13] also revealed that neutron $i_{13/2}$ and proton $h_{11/2}$ and $h_{9/2}$ orbitals play a crucial role for alignment gain.

In this thesis research, we further studied high-spin structures in ^{168}Hf with the Gammasphere array. The previously known level scheme of ^{168}Hf [1] has been extended considerably. Seven new bands were found. In addition, the six previously known bands have been extended to significantly higher spins. Three of the seven new bands are high-K bands. Spin and parities of the new bands have been determined based on the measurements of directional angular correlations from oriented states (DCO ratios). Theoretical calculations have been performed employing the Ultimate Cranker (UC) code. Possible intrinsic configurations were suggested for the new bands and compared with neighboring nuclei. Notably, high-K bands are suggested to be built on proton excitations and have been confirmed from B(M1)/B(E2) ratios. Since the quasiparticle excitations and collectivity are interrelated to deformation, we also measured quadrupole moments through the lifetime experiment of yrast states using the Doppler shift attenuation method. The results were compared with predictions from Total Routhian Surface (TRS) and UC calculations.

Chapter 2 incorporates nuclear shapes and various nuclear models. Chapter 3 discusses the concept of lifetime measurements using the Doppler Shift Attenuation Method. The experimental methods and techniques is thoroughly discussed in Chapter 4 while Chapter 5 deals with data analysis. Chapter 6 and Chapter 7 contain

information and discussion of the normal, and superdeformed bands respectively. Finally, a brief conclusion to this thesis is presented in Chapter 8.

CHAPTER II

THEORETICAL BACKGROUND

2.1 Introduction

The nucleus is a complex, many-body, quantum system in which the interaction of the nucleons determines the properties of the nucleus. Except for the lightest systems, nuclear properties cannot be calculated directly from first principles because of the great computational power required for a system with tens to hundreds of interacting protons and neutrons. The nuclear landscape exhibits striking elegance in what could be a jumble of thousands of varied systems which is, in practice, not easily solved. Nonetheless, there has been considerable success in describing the nucleus using various approximations or models.

The nucleus continues to fascinate and surprise physicists throughout time. The early Greek society was one of the first to speculate about the discrete nature of matter and the possibility that it was composed of atoms. During the past 100 years, our understanding of matter has greatly improved and scientists continue to study their structure.

The history of nuclear physics began with the discovery of three radiations (*i.e.* α, β and γ) by Antoine Bequerel, Marie and Pierre Curie in the 1890's [14]. After Ernest Rutherford discovered nucleus in 1911, J.J. Thomson found that there could

be several isotopes of a given element. In spite of these remarkable discoveries, still little was known about the structure of the atom. In 1913, Niels Bohr published his theory of atomic structure which was only fully understood after the development of quantum mechanics in the 1920's [14]. In 1924, Wolfgang Pauli suggested that the nucleus, apart from spherical, could exist in different shapes (*e.g.* prolate, oblate) depending in its mode of excitation [15]. Bohr and Kalckar later proposed that these non-spherical nuclei can be studied by measuring γ-ray transitions. When a nucleus is excited in a nuclear reaction, it will "cool" down by emitting particles and then γ-rays such that it will eventually reach a ground state. With this concept in mind, heavy-ion accelerators and γ-ray detectors were developed for the γ-ray spectroscopy.

In 1959, Maria Mayer and Hans Jensen came with the idea of the shell model [16, 17] which could help to explain radioactive stability. Aage Bohr, Ben Mottelson, and James Rainwater later discovered the phenomenon of collective and single-particle rotational motion in nuclei. Many features of nuclear rotation were discovered and understood in terms of the coupling between rotational and other nuclear degrees of freedom. In 1970 while studying high-spin structures, the phenomenon of back-bending was discovered which has been understood as the rotational alignment of a certain pair of nucleons. Since the γ-ray detectors of that time were not very powerful enough, many γ-ray detector arrays, *e.g.* Gammasphere and Microball, were developed around the world in 1980's and 1990's. As a result, many new and fascinating phenomena were discovered and out of which superdeformation is one of the most important.

Superdeformation is not a new phenomenon as it is well known that the fission isomers [18, 19] in the A $\sim$ 240 actinide region correspond to second minimum potential energy states with a 2:1 axis ratio in their ground states. Theorists predicted yrast[1] superdeformed states at high spins in the 1970's [20, 21]. In 1984, the University of Liverpool, Daresbury Laboratory, and the Niels Bohr Institute using the TESSA2 array [22] found the first experimental evidence of a superdeformed structure in the nucleus ^{152}Dy [23]. Recent studies show how nuclei exhibit various symmetries including spherical, prolate, oblate, octupole and triaxial asymmetric shapes. The nuclear high-spin γ-ray spectroscopy strives to answer some of questions regarding nuclear shapes and the forces which cause them by studying the γ-ray decay from an excited nucleus.

A good measure for how well the nuclear system is understood may be seen by how well theoretical models reproduce experimentally observed effects. Nuclear Models are attempts at exploiting the similarities in behavior between the nucleus and some other less complex physical system that can be more easily explained mathematically. For a model to be considered "good", one should be able to use it to successfully calculate some nuclear properties. Sooner or later though, a model may be found to be inadequate because there may be some aspects of the nucleus with which it cannot deal. With this in mind, one must carefully choose the model that is best suited to describe the phenomena being studied. While it is not possible to discuss all nuclear models in detail, the author has chosen to discuss those models that are useful when explaining the main features of the present work, namely, triaxial superdeformation and collective rotation.

[1]Yrast is referred to a line on a plot of spin versus energy which connects the states with the lowest energy for a given spin. Consequently no states exist below this line.

2.2 Early Models of the Nucleus

It was Hans Bethe who first proposed that the Nucleus can be treated as a system of non-interacting particles held together by a common potential [14]. This single-body potential not only acts on nucleons bound by the nucleus, but ones near it as well. Such an approach or "model" provided the means by which the very first detailed calculations of scattering cross-sections, for particles incident on a nucleus, were performed. The resulting cross-sections calculated using this approach tended to vary quite smoothly with beam energy. However, it was later found that cross-sections are not smooth and instead have irregular resonance structure. These resonances tend to be narrow, with widths of a few electron volts (eV). It turns out that lifetimes (Δt $\sim \hbar/\Delta$E $\sim 10^{-15}$ seconds) corresponding to these widths are usually on the order of a few femto-seconds. These lifetimes are very much longer than the time it takes a projectile to simply pass by a nucleus (10^{-22} seconds). Initially this phenomenon created some confusion, but its explanation led to a drastically new approach in understanding the nucleus.

In order to explain these resonances, Neils Bohr proposed that a compound nucleus is formed when a nucleus captures an incident particle. The resulting compound system lives for a relatively long time before decaying via one of a number of different reaction channels. The incident particle is attracted to the nucleus and strongly interacts with all the nucleons in the nucleus. The particle's energy is then shared with all the nucleons it encounters until some equilibrium is reached. Subsequently, this energy is transferred throughout the system by further collisions until a particle near the surface of the nucleus receives sufficient energy to escape.

The resulting process takes about 10^{-15} to 10^{-18} seconds and corresponds nicely with the observed resonance widths. During this entire process the nucleus can be considered as a *drop of liquid* [14, 24, 25, 26]. In this approach, the nucleus is treated as a constant density ellipsoid. Any energy is shared throughout the system and can lead to evacuation on its surface. Like a liquid drop, the nucleus is held together by surface tension resulting from the mutual attraction between all the nucleons in the nucleus. Since this drop contains charge, any internal oscillations tend to be destabilizing. This characteristic makes heavy nuclei somewhat unstable and is responsible for them breaking into fragments (i.e. fission). In 1939, Bohr and Wheeler [27] performed the first detailed calculations of the fission process using this model. The liquid drop model has also been somewhat successful in calculating binding energies [28, 29] and the bulk properties of the nucleus [30].

In spite of its great success, the liquid drop model could not explain many phenomenon. Many of the properties calculated using this model tend to vary smoothly as a function of proton (Z) and neutron (N) numbers. However, this is not what is observed experimentally. As it turns out, many nuclear properties behave in a discontinuous manner and always tend to occur for nuclei with certain numbers of Z and N. This discontinuities occur when Z or N have values of 2, 8, 20, 28, 50, 82, and 126. These numbers of protons and neutrons are commonly known as the *magic numbers*. In fact, this behavior is very similar to what is observed in the ionization potentials for atoms. This similarity immediately suggests that, like atoms, nuclei have some type of shell structure. The liquid-drop and Fermi-gas models predict that the properties of the nuclei vary smoothly with the mass and other parameters. However, experiments show that this is not the case. Large splitting occurs between the nucleon energy levels for the magic numbers 2, 8, 20, 28, 50, 82 and 126.

Nuclei with the number of protons, Z, and/or neutrons, N, equal to the magic numbers have higher binding energy than otherwise. This is similar to the shell structure of the electrons in the atom, obtained by solving the Schrödinger equation for the Coulomb potential. Compared to the atomic electrons, the nucleons have different magic numbers, which could not result from the same potential since other forces are active in the nucleus, primarily the strong force, and therefore a new potential had to be used. Many different potentials were examined, but the breakthrough came first when a spin-orbit term, $V_{so}(r)\ \ell\cdot\sigma$, was introduced.

2.3 The Spherical Shell Model

One basic feature of the shell model approach is the use of an attractive central potential [14, 31]. Since the allowed energy shells and their associated quantum numbers in a given potential can be obtained quantum mechanically, the Schrodinger equation is written as

$$H\psi = \left[-\frac{\hbar^2}{2m}\Delta^2 + V(r)\right]\psi_{nlm}(\mathbf{r}) = E_{nlm}\psi_{nlm}(\mathbf{r}) \tag{2.1}$$

As the attractive force depends on the radial distance from the origin, the angular dependence of the wave function describing a given particle is separable from the radial term. Thus, the wavefunction can be written as

$$\psi_{nlm}(\mathbf{r}) = \psi_{nlm}(r,\theta,\phi) = \frac{R_{nl}\psi_{nl}(\theta,\phi)}{r} \tag{2.2}$$

The orbital angular momentum $(l)^2$ is a constant of the motion. Therefore, l is a good quantum number and all states with a different projection of $\mathbf{l}$ on the z-axis are

[2]The shell label represents the orbital angular momentum l (*i.e.* s, p, d, f, g, h, i,.. correspond to l=0, 1, 2, 3, 4, 5, 6,..., respectively).

degenerate (i.e. they all have the same energy). So including the spin degeneracy, there are $2(2l+1)$ states in each level. As in the case of atomic structure, each level can be filled with $2(2l+1)$ particles, as allowed by the Pauli exclusion principle, and thus, one can obtain the magic numbers for a given potential.

The simple Harmonic oscillator potential is a commonly used, highly degenerate nuclear potential [14, 31] which is given by

$$V(r) = \frac{1}{2}M\omega^2 r^2 + V_o \tag{2.3}$$

and yields nucleon energy states of

$$E = \left(N + \frac{3}{2}\right)\hbar\omega + V_o \tag{2.4}$$

with N = 2(n-1) + l where n and l are integers. The corresponding energies are displayed on the far left side of Figure 2.1. It is important to note that the sequence of magic numbers produced using this potential (2, 8, 20, 40, 70, 112) does not match those observed experimentally. At this point, it is obvious that either a different nuclear potential should be chosen or some modifications to this potential must be made. One possible modification, or correction, would be the addition of an $\vec{l}^2$ attractive potential to the above Hamiltonian. Thus, any particle with large amounts of orbital angular momentum would effectively experience a stronger attractive force that lowers its energy. In other words, the addition of an $\vec{l}^2$ term is equivalent to a more attractive potential at large radii and comes closer to reproducing the constant interior potential. This modification, however, still fails to reproduce the experimental magic numbers and additional corrective terms must be added.

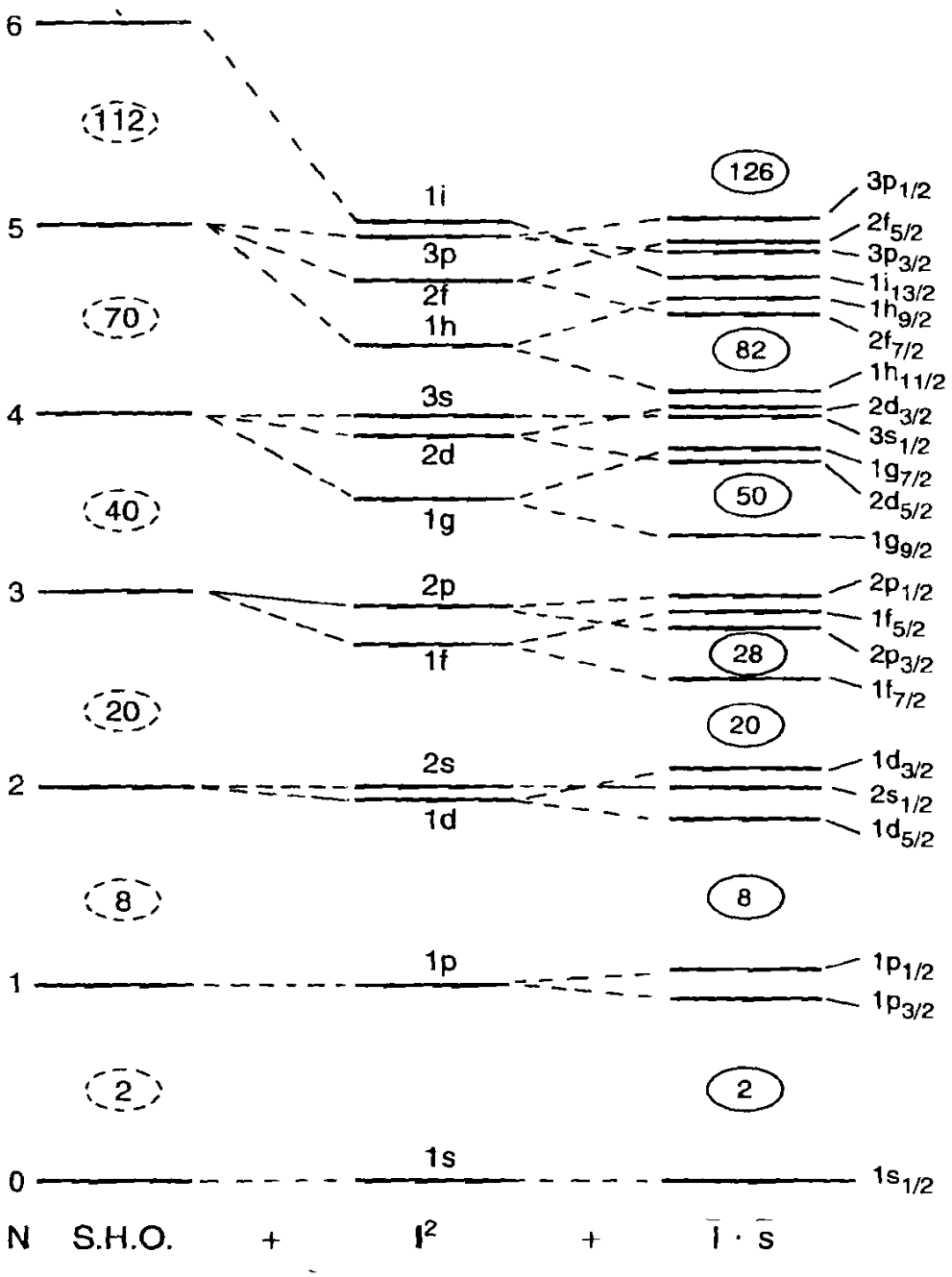

Figure 2.1: Single-particle energies for a simple harmonic oscillator (SHO), a modified harmonic oscillator with l^2 term, and a realistic shell model potential with l^2 term and spin orbit *(l.s)* terms. Taken from Ref. [31].

In 1949, following a suggestion by Fermi, Mayer and Jensen [32] proposed that the potential should include a component dependent upon the intrinsic spin and orbital angular momentum of a given nucleon. This spin-orbit potential is of the form

$$V(r) = -V_{ls}(r)\mathbf{l.s} \tag{2.5}$$

and has eigenvalues of l/2 and -(l+1)/2 depending on whether the spin and orbital angular momentum vectors are coupled to yield $j = l+1/2$ or $j = l-1/2$, respectively. This in turn splits each $l > 0$ state into two components. Thus, for example, the g state ($l = 4$) is split into the $g_{7/2}$ and $g_{9/2}$ orbitals, with the half-integer subscripts being the total angular momentum **J**. Now **J** is the only good quantum number and each level has (**2J+1**) degeneracy. Since the spin-orbit interaction is attractive, the energy of those particles whose intrinsic spin and orbital angular momentum are parallel is lowered. Likewise, for particles whose spin and orbital angular momentum are antiparallel, their energy is raised. This modification successfully reproduces the known experimental magic numbers (see Figure 2.1).

2.4 Deformed Shell Model

Even though the spherical shell model has been able to successfully predict various properties (*i.e.* ground state spins and excitation energies for nuclei which possess a closed shell or nearly closed shell of nucleons), it fails when there are many nucleons outside a closed shell or core. These exterior or valence nucleons not only interact amongst themselves but with the entire core as well. These interactions tend to deform the core and lead to a variety of phenomena such as rotational bands, enhanced transition probabilities B(E2), and large quadrupole deformations. Since these phe-

nomena cannot be explained using the spherical shell model, a different framework, one that considers an average deformed nuclear potential, is required.

A deformed nuclear potential leads to various collective degrees of freedom as well as influences the motion and energy levels of individual single-particles. One major and important consequence of the non-spherical nuclear shape is that rotational motion can be defined in quantum mechanical terms. Up to date, the most successful deformed shell models are the Nilsson [33, 34] and Wood-Saxon models [35, 36, 37].

2.4.1 Nuclear Deformation

In order to characterize the deformation of a nucleus, deformation parameters describing the shape of the nucleus have been introduced. In one description, these are denoted by β_2 , β_4 and γ. The β_2 deformation parameter describes the quadrupole deformation of the nucleus, and the β_4 deformation parameter gives the hexadecapole deformation of the nucleus, and γ describes its nonaxiality. The mapping of these shapes as a function of γ and β is shown in Fig. 2.2, using the Lund convention [20].

The shape of the nucleus is said to be prolate when two of its principal axes have the same length, and the third axis is longer. If the third axis instead is shorter, the shape is called oblate .

For well-deformed nuclei, axially symmetric shapes often give a good description of the nuclear properties, although some exceptions probably exist. For nuclei that are not so strongly deformed, a triaxial shape sometimes is introduced. The size of this axial asymmetry is described by the γ deformation parameter.

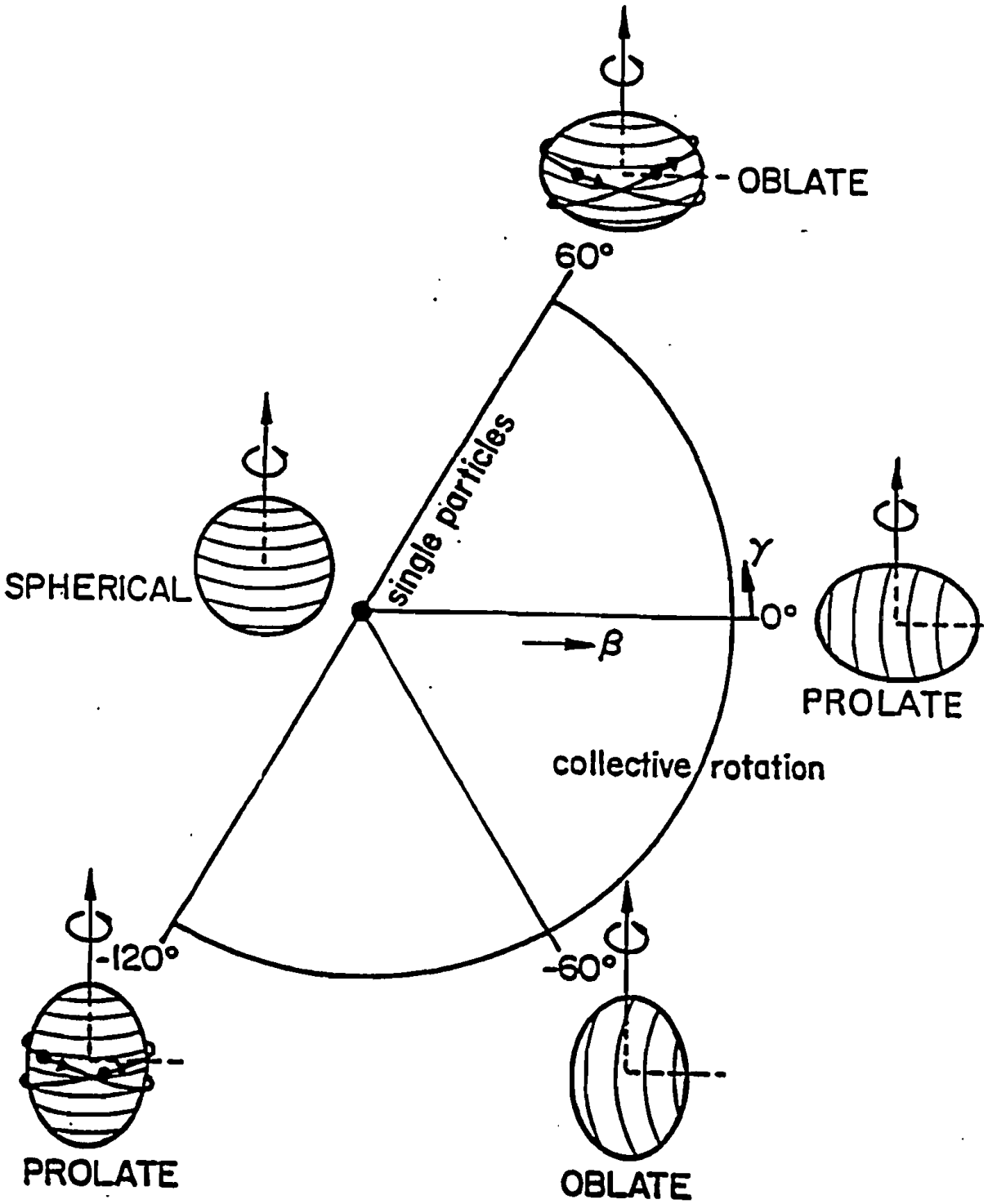

Figure 2.2: The nuclear deformations described in the Lund convention. Adapted from Ref. [20].

Some nuclei far from regions with filled shells are permanently deformed in their ground states, *i.e.* they are non-spherical. In the simplest case - that is when a nucleus has a shape that can be approximated by an ellipsoid - the surface can be described in terms of the spherical harmonics by

$$R(\theta, \phi) = R_{av}(1 + \beta_2 Y_{20}(\theta, \phi)) \tag{2.6}$$

Here, $\beta_2 > 0$ or $\beta_2 < 0$, the nucleus has the form of a prolate (elongated) or oblate (flattened) ellipsoid, respectively. Usually the average radius, R_{av}, is approximated with

$$R_{av} \approx R_0 A^{1/3}; R_0 = 1.2fm \tag{2.7}$$

When the deformation is more complex, the shape can be described by a series of spherical harmonics

$$R(\theta, \phi) = R_{av}(1 + \sum_{\lambda=1}^{\infty} \sum_{\mu=-\lambda}^{\lambda} \alpha_{\lambda\mu} Y_{\lambda\mu}(\theta, \phi)) \tag{2.8}$$

or a simplification of this expression. Equation 2.6 is one version of Equation 2.8 where $\beta_2 = \alpha_{20}$, valid for cases with axial symmetry.

2.4.2 Triaxiality

We know that the shape of a nucleus can be either deformed or spherical. In most deformed nuclei the quadrupole deformation is dominant, and, so far, nuclear spectra have been mostly associated with axially symmetric deformed shapes, *i.e.*, with either prolate or oblate deformation. However, triaxial deformation (for example, a nuclear shape with parameters: $\epsilon_2 > 0$ and $|\gamma| \sim 20°$), *i.e.*, deformation implying the breaking

of axial symmetry, has attracted much attention over the past decades since it opens a new dimension to study collective nuclear rotation in the sense that the rotation of axially symmetric nuclei becomes a limit to a more general description. Triaxiality relates to a nucleus with a shape characterized by three unequal principle body-fixed axes, like a kiwi fruit. Its occurence in nuclei has been a longstanding prediction of nuclear structure theory. In such triaxial nuclei, the mass distribution and, therefore, the moment of inertia is different along each of the three principal axes.

Experimental signatures for a triaxial shape are difficult to establish, and, as a result, conclusive evidence has only appeared in the last few years, although the pheneomenon was predicted more than 25 years ago. Triaxiality has now been invoked to described various phenomena, including so-called chiral bands and wobbling bands. Both types of collective structures are now widely accepted as unique fingerprints for triaxiality.

2.4.3 Woods-Saxon and Harmonic Oscillator (Nilsson) Potentials

A highly effective deformed shell model is the Woods-Saxon model [37]. In this model, a realistic potential often used is the Woods-Saxon potential with rounded edges:

$$Vo(r) = -\frac{V_0}{1 + e^{(r-R)/a}} \tag{2.9}$$

where 'R' is about the half-density radius of the nucleus and 'a' is the diffuseness parameter. The form of this potential is between a simple harmonic oscillator and a square well potential. The total nuclear potential thus becomes

$$V(r) = V_o(r) + V_{so}(r)\ell \cdot \sigma \tag{2.10}$$

This is the foundation for the shell model for spherical nuclei, which has been very successful in describing nuclei near closed shells, especially at low excitation energies. A second effective deformed shell model is obtained by using the the Nilsson potential which is given by:

$$V(r) = \frac{1}{2}M{\omega_0}^2 r^2 - C\ell \cdot \sigma - D(\ell^2 - < \ell^2 >_N) \tag{2.11}$$

The first term in Equation 2.11 gives an anisotropic oscillator potential, the second term accounts for the spin-orbit interaction. The third term was introduced to lower the energy of one-particle states at large values of ℓ, the orbital angular momentum, to make the potential fit more accurately to observations. The expression $<\ell^2>_N = \frac{N(N+3)}{2}$ denotes the average value of ℓ^2 taken over each N-shell, and is added in order to avoid a general compression of the shells. The constants C and D are positive and are obtained by fitting to levels in well-known nuclei.

2.4.4 Nilsson Model

The Nilsson Model is a shell model for deformed nuclei [31, 38]. This model describes the motion of a single particle in a non-spherical potential. The most basic form of the Nilsson model incorporates only axially-symmetric quadrupole deformed shapes. The Nilsson potential (Equation 2.11) can easily be extended to three dimensions, allowing a deformed nucleus with axes of different lengths:

$$V(r) = \frac{1}{2}M({\omega_x}^2 x^2 + {\omega_y}^2 y^2 + {\omega_z}^2 z^2 - C\ell \cdot \sigma - D(\ell^2 - < \ell^2 >_N) \tag{2.12}$$

In the case of axial symmetry, the particle frequencies of the two axes perpendicular to the symmetry axis are equal, $\omega_x = \omega_y = \omega_\perp$. Introducing the elongation parameter as $\epsilon = (\omega_\perp - \omega_z)/\omega_0$ which is related to the deformation parameter β_2 by

$$\epsilon = \frac{3}{2}(5/4\pi)^{1/2}\beta_2 \tag{2.13}$$

Quantum numbers from the Nilsson model are often used to characterize wave functions in deformed nuclei, even though the calculations are based on another model.

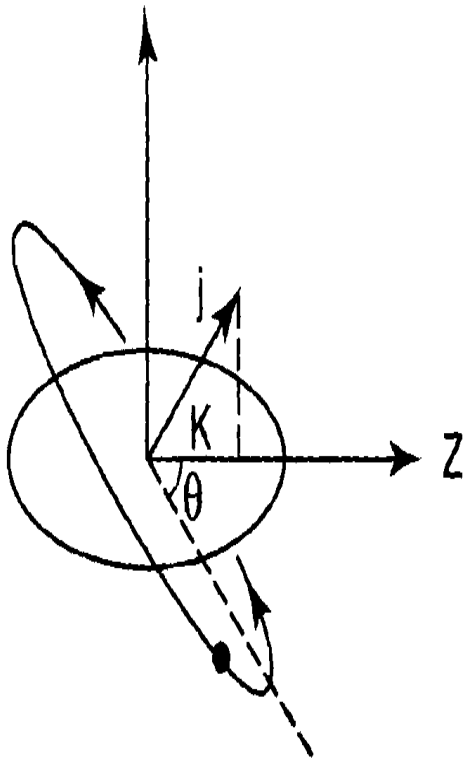

Figure 2.3: A nucleon orbiting an axially symmetric deformed nucleus (K = Ω). The diagram also defines the quantities j, K and θ for the Nilsson model. Adopted from Ref. [31].

2.4.5 Single-Particle Energy Diagrams

In order to develop single-particle energy diagrams in both the Nilsson and Wood-Saxon frameworks, one needs a single-particle potential with quadrupole deformation and a short-range attractive nuclear force. Let's consider a single valence nucleon orbiting a prolate deformed nuclear core as shown in Fig. 2.3. Since the core is deformed, the valence nucleon experiences a prolate deformed potential. The closer the nucleon's orbit comes to the core (and the rest of the nuclear matter), the lower its total energy. Thus, the particle's energy depends on the orientation of its orbit with respect to the symmetry axis (z-axis). This state is contrary to the spherical shell model where there is no preferred orientation. This orientation or magnetic substate of the nucleon, commonly referred to as **K**, is simply the projection of the total angular momentum of the single particle on the symmetry axis (Fig. 2.3). Thus, low **K** values correspond to single-particle motion along the symmetry axis near the bulk of the nuclear matter for a prolate deformed core.

Using Figure 2.3, we can calculate the classical orbit angle θ corresponding to different **K** values using the expression

$$\theta = \arcsin\left(\frac{\mathbf{K}}{j}\right) \tag{2.14}$$

So, for example, the $\imath_{13/2}$ orbital ($\jmath = 13/2$) has **K** substates of 1/2, 3/2, 5/2, 7/2, 9/2, 11/2 and 13/2 with corresponding orbital angles θ of 4.4°, 13.3°, 22.6°, 32.6°, 43.8°, 57.8°, and 90°, respectively. Note that θ changes slowly for low **K** values, but more rapidly for higher ones. Thus, one should expect that the energy difference between orbitals with small **K** values is somewhat less than that for the large **K** orbitals. With this in mind, one can begin to develop the single-particle energy diagram for

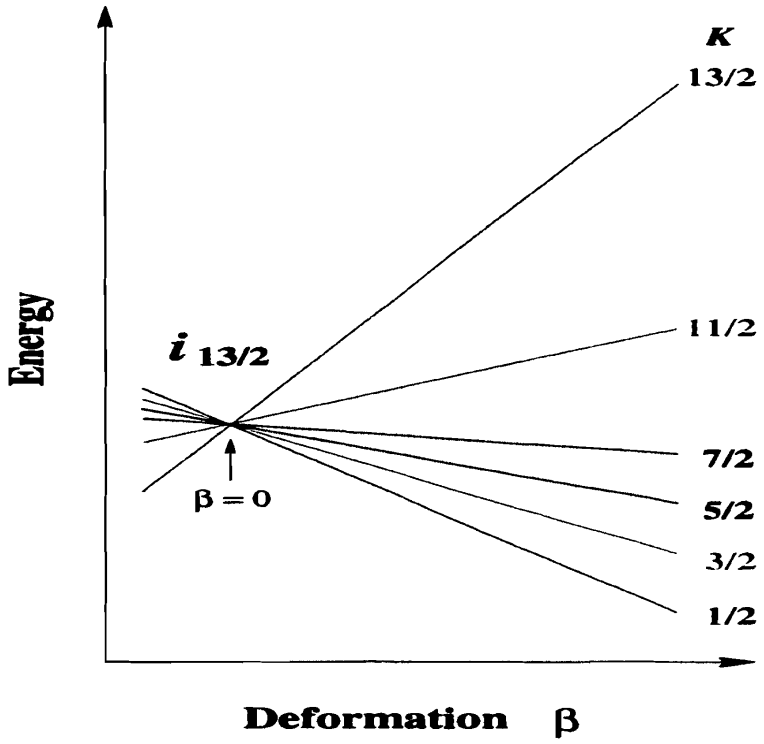

Figure 2.4: Splitting of $i_{13/2}$ orbital as single-particle energy varies with K ($\beta > 0$, prolate, to the right). Modified from Ref. [31].

the $\imath_{13/2}$ orbital in the region where $\beta > 0$ (Fig. 2.4). It is interesting to note that the separation of adjacent states sharply increases with **K**. For those orbitals with low **K** values, their energy decreases very rapidly with increasing β. The more downward sloping low **K** orbitals are commonly known as *intruder* orbitals because they intrude into the lower shells. On the other hand, for those orbitals with high **K** values their energy increases rapidly with increasing β. The more upward sloping of these orbitals are referred to as *extruder* orbitals.

The last step needed to fully develop the entire single-particle energy diagram (β>0) is to combine all the orbitals with different $\jmath$ values. Since the dominant feature of a deformed field is the single-nucleon mixing of different $\jmath$ values, one must

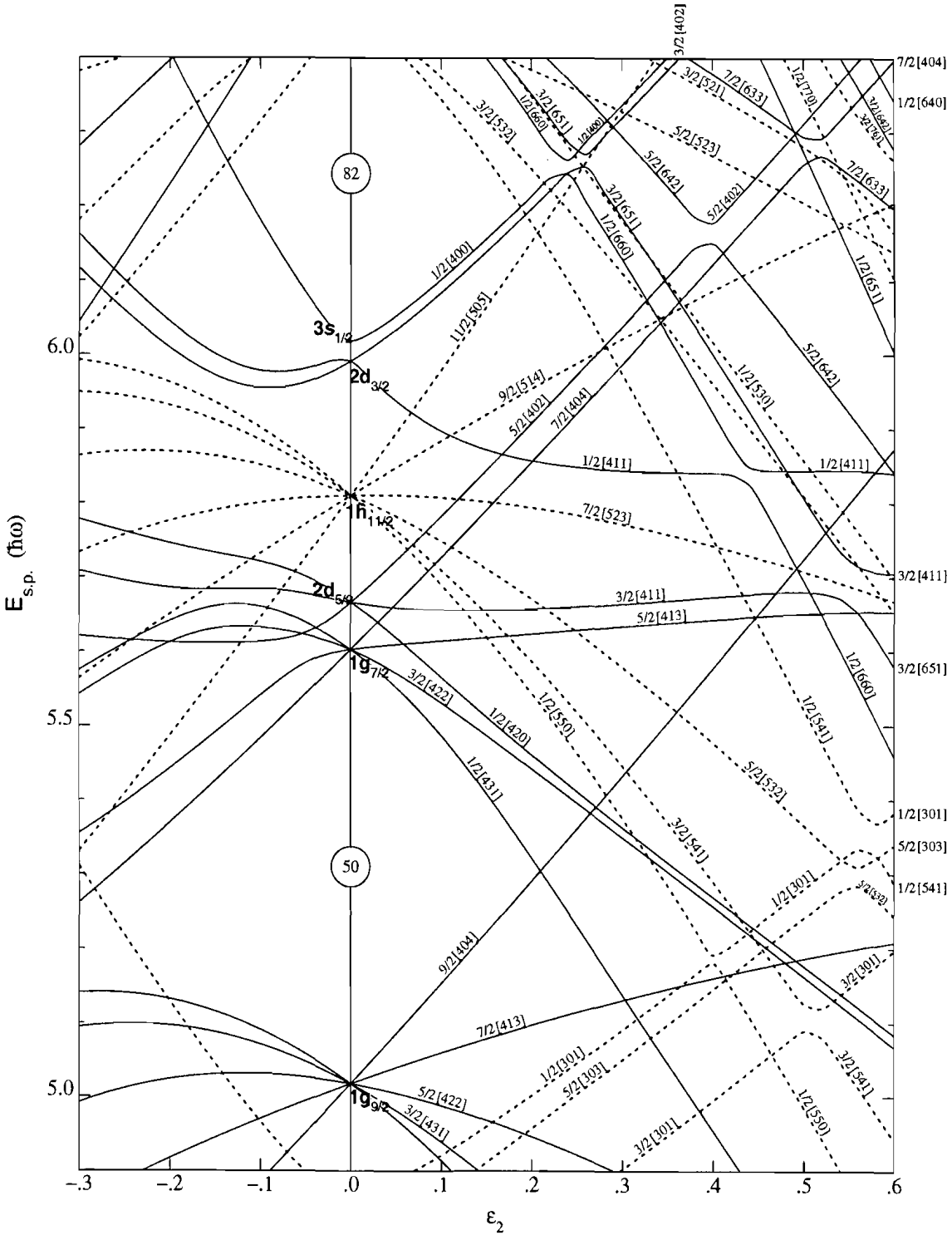

Figure 2.5: Nilsson diagram for protons, $50 \leq Z \leq 82$ ($\epsilon_4 = {\epsilon_2}^2/6$) [33, 34].

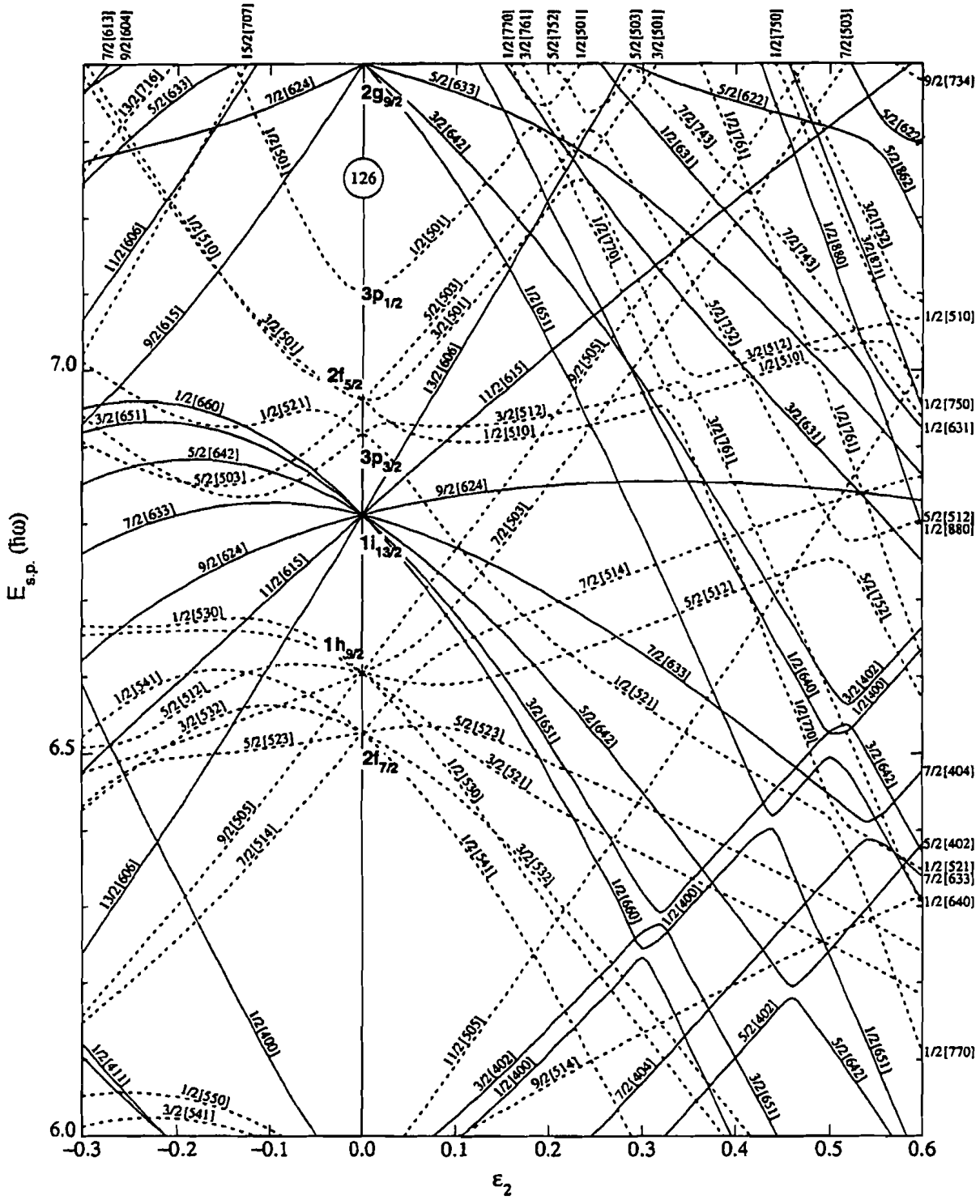

Figure 2.6: Nilsson diagram for neutrons, $82 \leq N \leq 126$ ($\epsilon_4 = {\epsilon_2}^2/6$) [33, 34].

superimpose it with the **K** splitting. Now recalling that no two orbitals with the same quantum numbers may cross and since the remaining good quantum number describing the orbit is **K**, then no two orbitals with the same **K** values (and parity π)[3] may cross. Thus, if two orbitals with the same **K** approach each other, an infinitesimal interaction will cause them to repel each other. When one incorporates many different j orbitals and considers realistic deformations where energies of different orbits intermingle, the entire single-particle energy diagram can be constructed. The single-particle energies for protons and neutrons calculated using a Nilsson potential [33, 34], are shown in Figures 2.5 and 2.6. Notice that each orbital corresponding to a given shell converges at spherical shape, $\epsilon_2 = 0$ ($\epsilon_2 = 0.95\beta_2$) and then slopes according to the angle of the orbit relative to the mass of the core. Also, notice that each orbital starts to curve when it approaches another level with the same **K** and π. Thus, the shape of orbitals in the diagram relies on 3 factors, **K** splitting, level-level repulsion, and input single-particle shell model energies.

2.4.6 Orbital Labeling Convention

In the both Nilsson [33, 34] and Woods-Saxon [35, 36, 37] models, orbitals are labeled using the following convention [31]:

$$\mathbf{K}^{\pi}[N, n_z, \Lambda] \tag{2.15}$$

The first term, **K**, is the projection of the total angular momentum **J** along the symmetry (z) axis. The parity of the state is given by π. The principal quantum number N represents the number of quanta associated with the simple harmonic

[3]Parity is associated with symmetry properties of the nuclear wavefunction under spatial inversion and is defined by $\pi = (-1)^l$ where l is the orbital angular momentum.

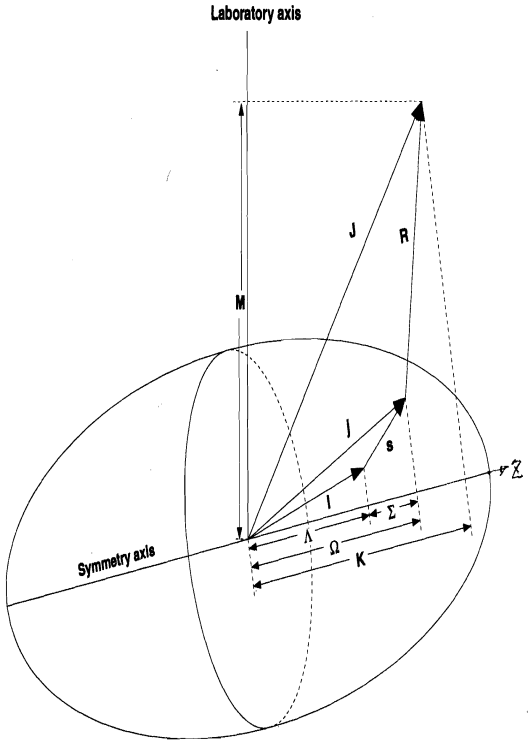

Figure 2.7: Asymptotic quantum numbers for the Nilsson model.

oscillator shell (see Fig. 2.1). The number of nodes in the wavefunction in the z direction is given by n_z. The last term, Λ, represents the component of the orbital angular momentum ℓ along the symmetry (z) axis. By definition, $\mathbf{K}$ and Λ are related by

$$\Lambda = \mathbf{K} \pm \frac{1}{2} \tag{2.16}$$

depending on whether the intrinsic and orbital angular momenta are parallel or antiparallel. Thus, each orbital is two-fold degenerate in $\mathbf{K}$. The asymptotic quantum numbers for the Nilsson model are shown schematically in Fig. 2.7.

2.5 Nuclear Excitations and Collective Rotation

In general, the lowest energy excitations of the nucleus can be simply explained when the nucleus is separated into those nucleons which are actively engaged in its equilibrium properties and various modes of excitation, the valence nucleons, and those nucleons which are largely bystanders, the mostly inert closed-shell core. The lowest energy excitations reflect occupation of orbits which are most accessible, generally those nearest the Fermi surface. The relative spacing between orbits, shown up to magic number 126 on the right of Fig. 2.1, and the filling on the last major shell provide information about the simplest expectations for nuclear excitations. The relative spacing between orbits within a major shell is a few hundred keV while the relative spacing between major shells is much larger - up to 1 MeV or more. Excitations between major shells require more energy than excitation within a major shell. The spacing between orbits and shells and the number of valence particles are useful starting points for interpreting the structure of the nucleus.

2.5.1 Single Particle Excitations

For simplicity, consider the ground state of a nucleus with an odd number of nucleons. Due to the short range residual interactions and the Pauli Principle, pairs of like nucleons in the same orbit prefer to couple to spin-parity $J^{\pi} = 0^{+}$. The spin of the ground state will be given by the sum of the angular momenta of all the nucleons, all but one of which are coupled to spin $J^{\pi} = 0^{+}$. Therefore, the ground state spin J of the nucleus is equal to the angular momentum j of the last nucleon. Excited states may be formed by promoting the odd particle to a higher energy orbit, leaving the underlying paired particles nearly undisturbed. The energy of this state approximately corresponds to the difference in energy between the orbits,

and the state is said to have a different configuration from that of the ground state. Additional configurations can be formed if a pair of nucleons is broken and these nucleon's angular momenta are coupled to various nonzero values determined by the Pauli principle. In the case of a doubly odd nucleus, one containing odd numbers of protons and neutrons, either or both of the unpaired particles may be promoted to higher energy orbits. Pairs of particles may also be moved to higher energy orbits.

While single particle excitations can occur in any nucleus, they are particularly prevalent at low energies near closed shells. Nuclei near closed shells generally do not have enough valence particles to facilitate collective motion at low energies, their structure can be interpreted in terms of single particle excitations. This idea is pivotal to the trans-lead region. It must be noted that the Shell Model is a greatly useful, simplifying approach to a small portion of nuclei, specifically those near closed shells. As valence particles are added, the shell model wave functions become extremely complicated in terms of the various amplitudes of the nuclear wavefunction, and a collective description of the nucleus becomes more appropriate.

2.5.2 Quasiparticle Excitations

In nuclei with large numbers of valence particles, such as nuclei in the rare earth region, excited states may be formed by promoting multiple quasiparticles to higher energy orbits. Such excitations differ from single particle excitations in that the nuclear wavefunction is not necessarily dominated by one amplitude. In deformed nuclei, the Nilsson Model gives the applicable single particle levels. Though it describes nuclei with many valence nucleons, the Nilsson Model recovers the single particle picture by ignoring the complexity of the underlying even-even system. Only excitations relative to the Fermi surface are considered. Some of the 0^+ states could be explained by

considering quasiparticle excitations, particularly two- and four-quasiparticle excitations [39] where the spins are coupled to $J^{\pi} = 0^{+}$. In general quasipartcle excitations lie higher in energy than typical collective excitations.

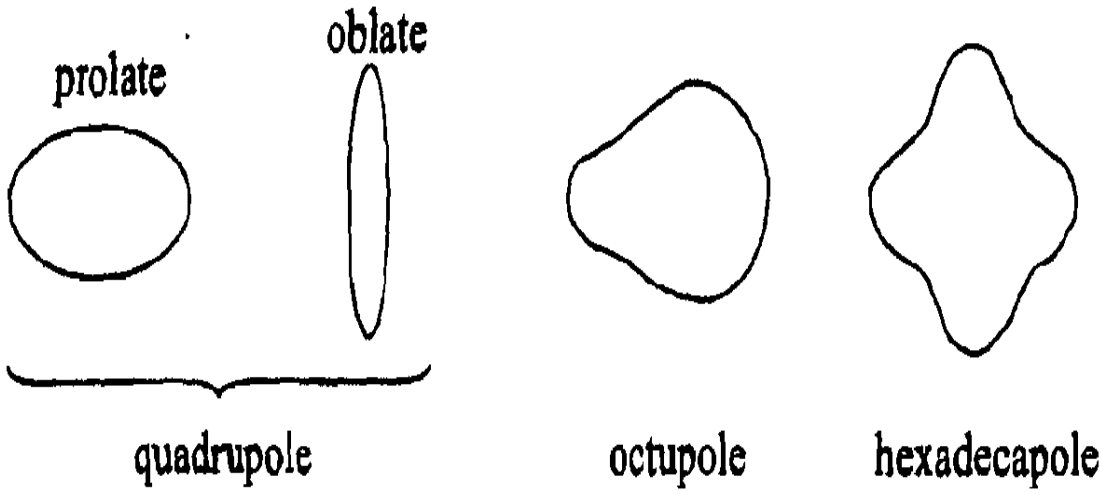

Figure 2.8: The normally deformed nucleus can take on various deformations such as an quadrupole, octupole, and hexadecapole.

2.5.3 Collective Excitations

Only non-collective excitations have been discussed up to this point. However, when the components of nuclear wavefunction add coherently, the nucleus may undergo collective motion. These collective phenomena, including vibrations and rotations, incorporate varying numbers of nucleons. Collectivity and the onset of deformation are commonly described geometrically in terms of the equilibrium shape of the nucleus, requiring a paradigm shift from the microscopic description of valence nucleons to the macroscopic picture of fluctuations about the equilibrium shape described by the degree and spatial orientation of the deformation. The macroscopic spherical shapes come from a uniform occupation of magnetic substates (microscopic). Con-

versely, deformed shapes stem from a nonuniform occupation of magnetic substates. The description of deformation, closely linked to collectivity, is extremely important in the geometric picture, and three basic shapes emerge from it: spherical, axially symmetric rotor, and axially asymmetric rotor. Axially asymmetric nuclei are often called gamma-soft, referring to the gamma degree of freedom, or the axial asymmetry. The shape of the deformed nucleus takes on many forms as depicted in Figure 2.8. Most deformed nuclei take on a quadrupole deformation. However, octupole and hexadecapole deformations can also exist in nuclei. The most common quadrupole deformations can be understood by stretching and squashing a spherical shape in any of three directions. The prolate nucleus, reminiscent of an American football, is elongated in one direction and squashed in the other two directions. The oblate nucleus, similar in shape to a frisbee, is stretched in two directions and squashed in one direction. Most nuclei are prolate deformed. The parameter β describes the degree of quadrupole deformation. In spherical nuclei, the nuclear potential well is centered at zero while in deformed nuclei, the potential well is centered around some finite value of β.

Deformation requires both valence protons and valence neutrons and can be estimated by the numbers of these valence particles [40]. The spacing of energy levels decreases as deformation increases, and deformation in transitional nuclei is commonly estimated by the ratio of the energies of the first 4^+ state to the first 2^+ state, or $R_{4/2}$. For nuclei at or near closed shells, the $R_{4/2}$ is near 1. As valence particles are added, the nucleus becomes more collective, and the $R_{4/2}$ for vibrational nuclei is ~ 2. Near midshell, with a maximum number of valence particles and deformation, the $R_{4/2}$ approaches 3.33 for rotational nuclei. These are ideal limits; ratios for real nuclei lie in the vicinity of these values.

The ideal limits give benchmarks for what would be structurally expected in nuclei falling near the limits. Deviations from the structures expected for these ideal limits give a great deal of insight into the structure of the nucleus. In the vibrational limit, the nucleus is spherical and can undergo quadrupole vibrations in which the surface of the nucleus expands and contracts. These phonons give rise to a regularly spaced set of harmonic levels.

When the nucleus is deformed, it may vibrate about the deformed equilibrium shape or rotate. Two types of quadrupole vibrations are possible. In the $\mathbf{K} = 0$ vibration, commonly but somewhat mistakenly referred to as the beta vibration, the nucleus vibrates along the symmetry axis, much like the case of the spherical nucleus. In the gamma vibration, the nucleus vibrates about the symmetry axis. Gamma vibrations occur in both axially symmetric and axially asymmetric nuclei. Though gamma vibrations are time dependent deviations from the symmetry in the axially symmetric case, the average shape of the nucleus remains axially symmetric. Rotational and vibrational modes can be superposed, giving rotational bands built upon vibrational states.

2.5.4 Gamma Decay

An excited nucleus may decay by emitting some kind of particle, undergoing fission, or by rapidly emitting a sequence of γ-rays. In these processes, the nucleus loses not only energy, but also angular momentum. In the last case, it is favorable for the nucleus to send away γ-rays with a large energy, but with as little angular momentum as possible. By this one can conclude that the most favorable way for the nucleus to decay is along the so called yrast line, which is defined as a sequence of all the states with the highest angular momentum for a given energy.

A γ-ray transition is characterized by the change in spin and parity of the nucleus caused by it, and it can be of electric or magnetic type. The multipolarity, the angular momentum carried away by the emitted photon for a transition between an initial state and a final state, is denoted by λ. If there is no change in parity and is even, the transition is of electric type, as well as when there is a change in parity and λ is odd. Otherwise, the transition is of magnetic type.

A transition of multipolarity λ is denoted by Eλ if it is electric and Mλ if it is magnetic. The picture is somewhat complicated by the fact that a transition can have mixed multipolarity. The admixture must be of higher multipole order and have the same correct change in parity. For example, a M1 transition can have an admixture of E2. The mixing ratio describes the amount of the admixture. As stated above, the lowest possible multipole order dominates. Furthermore, an E transition is more probable than a similar M transition. As a result of this, the aforementioned E2/M1 mixture is quite common, but a M2 transition is too weak to compete with an E1.

2.5.5 Collective Rotation Motion

An important consequence of deformation is the fact that rotational motion is a possible mode of excitation. In the spherical case, it is not possible to observe the collective rotation about an axis of symmetry, since the different orientations of the nucleus are quantum-mechanically indistinguishable. In the case of an axially symmetric nucleus, there is a set of axes of rotation, perpendicular to the symmetry axis. The rotational angular momentum, $\vec{R}$, is generated by the collective motion of many nucleons about this axis. Additional angular momentum can be generated by the intrinsic angular momentum of any valence nucleons, $\vec{J}$. The total angular momentum, $\vec{I}$, of the nucleus is then

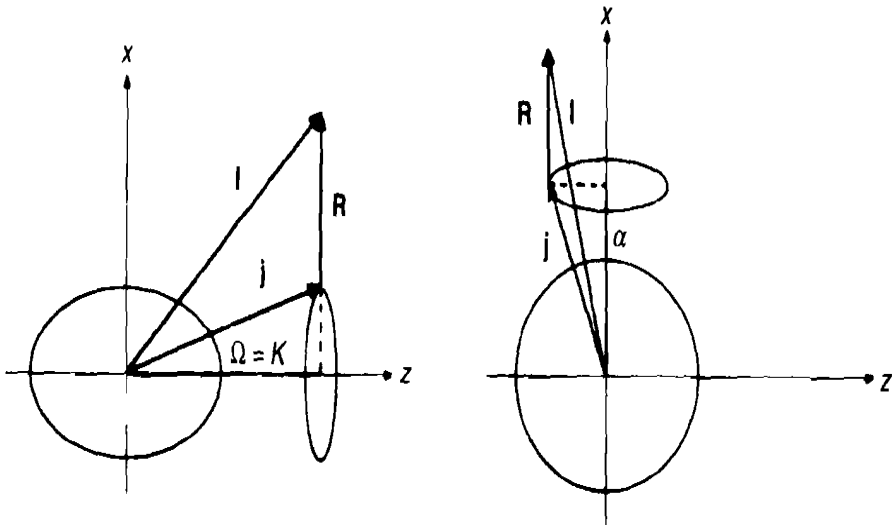

Figure 2.9: Schematic of the coupling of the collective angular momentum, $\vec{R}$ and the intrinsic angular momentum of the valence nucleons, $\vec{J}$. The left figure illustrates the coupling scheme for deformation alignment and the right for rotation alignment [38]. The projection of the total angular momentum, $\vec{I}$, onto the symmetry axis is K.

$$\vec{I} = \vec{R} + \vec{J} \tag{2.17}$$

This angular momentum coupling is shown schematically in Figure 2.9. The intrinsic angular momentum of the valence nucleons, $\overrightarrow{J}$, is the sum of the angular momenta of the individual valence nucleons, i.e. $\vec{J}=\sum_{i=1}^{A}\vec{j_i}$. The projection of the total angular momentum onto the symmetry axis is K, and is the same as the projection of $\vec{J}$. The projection of the angular momentum, $\vec{J}$, of a valence nucleon is $\vec{\Omega}$; thus $\vec{\Omega}=\sum_{i=1}^{A}\vec{\Omega_i}$. In the ground-state rotational band of an even-even nucleus, the valence particles are paired such that $\vec{J}= 0$, and the total angular momentum $\vec{I}=\vec{R}$.

The collective rotational energy can be determined through analogy with a classical rotating rigid body. The angular momentum of the rotating rigid body is I=$\Im$ and hence its classical kinetic energy is

$$E = \frac{I^2}{2\Im} = \frac{1}{2}\Im\omega^2 \tag{2.18}$$

where $\Im$ is the moment of inertia and ω is the rotational frequency. By analogy to the quantum mechanical case, this becomes

$$E = \frac{<\hat{I}^2>}{2\Im}; \quad <\hat{I}^2> \quad = \quad \hbar^2 I(I+1) \tag{2.19}$$

Thus the rotational motion of the nucleus leads to a sequence of states with energy

$$E = \frac{\hbar^2 I(I+1)}{2\Im_0}; \tag{2.20}$$

In the above equations $\Im_0$ is the static moment of inertia. It should be noted that the nucleus, however, is not a rigid body, and measured moments of inertia are somewhat less (30 to 50%) than rigid body values at low spin. This is due to the effects of the pairing interaction, which make the nucleus behave like a super fluid (Pairing is discussed in Section 2.7). Experimental moments of inertia are also larger than those calculated for the rotation of a super fluid, showing that the nucleus is somewhere between these two extremes. As the nucleus rotates, it is found that the moment of inertia changes as a function of spin.

The ratio $\frac{\hbar^2}{2\Im}$ is called the rotational energy constant. The excitation energies corresponding to $I^\pi = 0^+, 2^+, 4^+, 6^+, 8^+$, etc. form a so-called rotational band sequence. In terms of the rotational energy constant the excitation energies are

$$\begin{aligned} E(0^+) &= 0 \\ E(2^+) &= 6(\tfrac{\hbar^2}{2\Im}) \\ E(4^+) &= 20(\tfrac{\hbar^2}{2\Im}) \\ E(6^+) &= 42(\tfrac{\hbar^2}{2\Im}) \\ E(8^+) &= 72(\tfrac{\hbar^2}{2\Im}) \end{aligned} \tag{2.21}$$

The γ-ray energy for an I→I - 2 transition thus becomes

$$E_{I\to I-2} = \frac{\hbar^2}{2\Im}(I(I+1) - (I-2)(I-2+1)) = \frac{\hbar^2}{\Im}(2I+1) \tag{2.22}$$

As can be seen, the γ-ray energy increases regularly for higher spin and excitation energy.

In the cranked shell model, also called the cranking model, the rotation vector is assumed to coincide with one of the symmetry axes of the nucleus. The nucleons can be described as independent particles moving in a rotating potential. One of the simplest potentials is the Nilsson potential (Section 2.4.3). It doesn't describe the nuclear properties as well as the Woods-Saxon potential, but its simplicity makes it possible to find analytical expressions for the interesting variables.

2.5.6 Moment of Inertia

The rotating nucleus can be described in terms of its angular rotational frequency, ω. Classically, this is

$$\omega = \frac{dE}{dI} \tag{2.23}$$

The quantum-mechanical analogue of this is given by

$$\hbar\omega = \frac{dE(I)}{d\sqrt{I(I+1) - K^2}} \tag{2.24}$$

where $\mathrm{d}\sqrt{I(I+1) - K^2}$ is the projection of the total angular momentum onto the rotational axis, known as the aligned angular momentum, I_x. For a K=0 rotational band of stretched transitions, this can be approximated by

$$\hbar\omega = \frac{E_I - E_{I-2}}{\sqrt{I(I+1)} - \sqrt{(I-2)(I-1)}} \approx \frac{E_\gamma}{2} \quad when \quad I >> K \tag{2.25}$$

Rotational energy spectra can be discussed in terms of two spin-dependent moments of inertia, which are related to the first- and second-order derivatives of the excitation energy with respect to the aligned angular momentum, I_x. The first order derivative is the kinematic moment of inertia,

$$\Im^{(1)} = I_x \left(\frac{dE}{dI_x}\right)^{-1} \hbar^2 \quad = \quad \hbar\frac{I_x}{\omega} \tag{2.26}$$

The kinetic moment of inertia can be related to the transition energy, E_γ, through Equation 2.22. For a rotational band,

$$E_\gamma = \frac{\hbar^2}{2\Im^{(1)}}(4I - 2) \tag{2.27}$$

The second order derivative is the dynamical moment of inertia,

$$\Im^{(2)} = \left(\frac{d^2E}{dI_x^2}\right)^{-1}\hbar^2 \quad = \quad \hbar\frac{dI_x}{d\omega} \tag{2.28}$$

The dynamical moment of inertia can be related to the difference in transition energy of consecutive γ-rays,

$$\Delta E_\gamma = \frac{4\hbar^2}{\Im^{(2)}} \tag{2.29}$$

Thus, if the dynamical moment of inertia were a constant, the transition energy difference would be the same for all values of spin. Often this is not true and $\Im^{(2)}$ is found to increase with increasing spin. In the limit of rigid rotation, $\Im(2) = \Im(1)$, the two moments of inertia can be related as:

$$\Im^{(2)} = \frac{dI_x}{d\omega} = \frac{d}{d\omega}\left(\omega\Im^{(1)}\right) = \Im^{(1)} + \omega\frac{d\Im^{(1)}}{d\omega} \tag{2.30}$$

2.6 The Cranking Model

The cranking model describes the rotation of a deformed nucleus around one of its principal axes. In this model, the nucleons can be described as indepedent particles moving in a rotating potential,e.g. the Nilsson potential.

The coordinates in the laboratory system are denoted by x, y, z, and those in the rotating frame of reference x', y' and z'. The nucleus is assumed to rotate around

the x-axis, with an angular velocity ω. The rotational transformation between the laboratory and the intrinsic coordinate system of the nucleus is then given by:

$$\begin{aligned} \text{x'} &= \text{x} \\ \text{y'} &= \text{y cos}\omega\text{t} + \text{z sin}\omega\text{t} \\ \text{z'} &= \text{-y sin}\omega\text{t} + \text{z cos}\omega\text{t} \end{aligned}$$

The Schrdinger equation in the time-dependent laboratory system is written as:

$$i\hbar\frac{\partial\psi_{lab}}{\partial t} = H_{lab}\psi_{lab} \tag{2.31}$$

A transformation to the rotating system is made by introducing the rotation operator $\Re$:

$$\Re = e^{-iJ_x\omega t} \tag{2.32}$$

where $\text{J}_x = \text{J}'_x$ is the component in the x-direction of the angular momentum operator. The transformation is given by:

$$\begin{aligned} \psi_{lab} &= \Re\psi_{intr}\Re^{-1} \\ H_{lab} &= \Re H_{intr}\Re^{-1} \end{aligned} \tag{2.33}$$

This inserted in Equation 2.31 gives:

$$i\hbar\frac{\partial\psi_{lab}}{\partial t} = (H_{intr} - \hbar\omega J_{x'})\psi_{intr} \tag{2.34}$$

where H^ω is called the cranking Hamiltonian, and is time independent. The eigenvalues of H^ω are called Routhians.

In addition to this average potential that determines the single-particle orbitals, a pairing force must also be included. The lowering of the moment of inertia with the introduction of pairing is discussed in Section 2.7.

H^{ω} from the cranking model is invariant with respect to a rotation with an angle π around the rotational axis, as well as under space inversion (parity), but not with respect to similar rotations around the other axes.

The operator corresponding to rotation around the x-axis with an angle π is denoted by $\Re_x = \Re'_x$:

$$\Re_{x'} = e^{-i\pi J'_x} \tag{2.35}$$

The eigenvalues of $\Re_x$ are denoted by $r = e^{-i\pi\alpha}$. Both r and α are defined to as the signature quantum numbers. The relation between spin and signature is:

$$I = \alpha(mode2) \tag{2.36}$$

The only quantum numbers that are conserved in the cranking model are those of parity and signature. The parity can be positive or negative, and the signature (α) can take the values of 0 or 1 for nuclei with even nucleon number, and can be $+\frac{1}{2}$ or $-\frac{1}{2}$ for an odd-A nucleus.

The states in a rotational band have, as stated above, an energy that depends on the nuclear spin as $E \propto I(I+1)$. From equation (2.36), one can conclude that the signature will alternate between two possible values, if I is increased one unit at a time. In fact, the original rotational band will be split into two parts, where the transitions within one part are of E2 type, and the transitions between the parts are of type M1. The parts have the same moment of inertia, and differ only in signature.

2.7 Pair Correlations

Fermions (e.g. protons and neutrons) tend to pair with similar fermions. These pairing correlations were first introduced by Bardeen, Cooper, and Schrieffer (BCS) [41] in their microscopic theory of superconductivity. The BCS theory was immediately incorporated into nuclear structure theory [42] as experimental evidence greatly supported the need for pairing correlations. The most well known evidence for pairing is that all even-even nuclei have $I^{\pi} = 0^{+}$ ground states. Accordingly the ground states in even-even nuclei are normally $\sim$ 1-2 MeV below any excited particle state. The odd-even mass difference, which indicates large gain in binding energy when an even-even nucleus is formed compared to its neighboring odd mass nuclei, also pointed towards the necessity of pairing. Other features, which were seen in retrospect, such as the nuclear moment of inertia being $\sim$ 30% of the rigid rotor moment of inertia in deformed nuclei and lower than expected band head energies of excited particle states in odd mass nuclei, could be explained with the use of BCS theory.

The qualitative description of two like nucleons pairing is shown in Fig. 2.10. Two partcles pair by orbiting in the same $\jmath$ shell and **K** orbital, but in opposite directions. The pair's angular momentum sums to zero and thus all even-even nuclei will have a 0^{+} ground state since all the nucleons will be paired initially. A collision will occur between the two and they will scatter into another equal and opposite orbit. The interplay between paired nucleons is known as time reversed orbits. A pair orbiting in a particular $\jmath$ state has an equal chance to scatter back into the same or different $\jmath$ state. This is actually a crucial point for if the pair were confined to remain in the same j orbit, then excited states could occur simply by raising both particles to the next unoccupied orbit. This would imply that the pairing gap observed in even-even

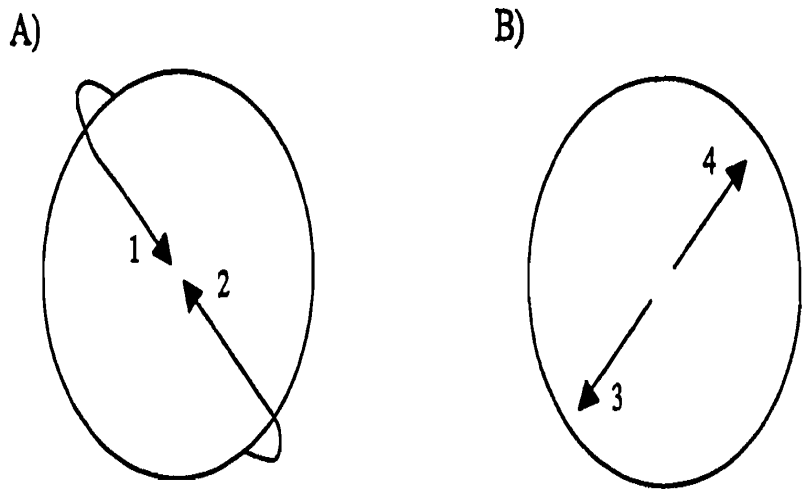

Figure 2.10: Two particles in a time reversed orbit associated with pairing correlations. Particles in orbits 1 and 2 collide and scatter into orbits 3 and 4. Adopted from Ref. [43].

nuclei would approximately be equal to twice the energy needed to raise a particle from $\jmath$ to $\jmath'$. On average, the gap in even-even nuclei would only be twice the energy of the excited band heads seen in their odd-A neighbors and not five to ten times as large as observed experimentally. Instead, by allowing pairs to scatter from $\jmath$ to $\jmath'$, the 0^+ levels mix and thus drive the ground state in even-even nuclei to lower energies and creates a partial occupancy of levels near the Fermi surface. This partial occupancy radically changes the concept of particle and hole excitations as will be shown below.

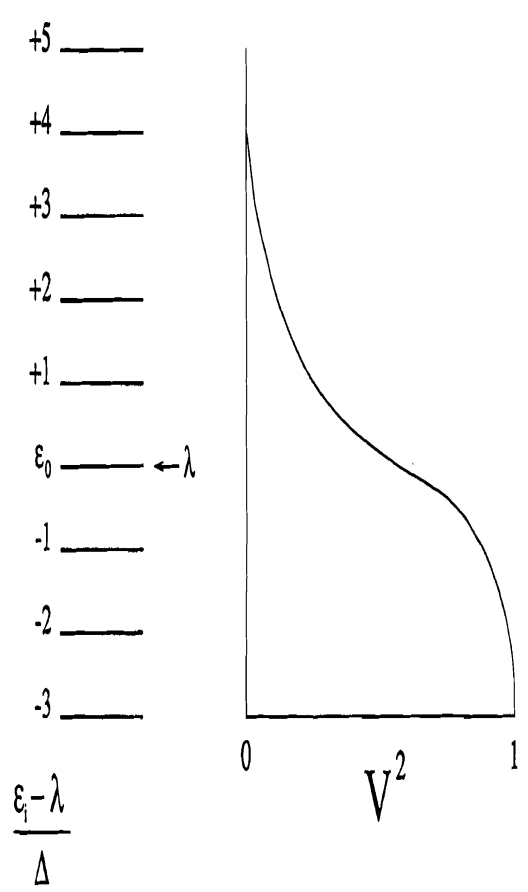

Figure 2.11: Partial level occupancy, resulting in a quasi-particle state, due to pairing. An ideal set of shell model levels are shown (left) and the resulting occupancy (right). Adopted from Ref. [31].

To continue the discussion, let's refer to the Fig. 2.11 where the Fermi level is denoted by λ and the single-particle energies ϵ_i, ϵ_o being reserved for the level nearest the Fermi surface. The pairing gap parameter, Δ, is defined in terms of a sum over orbits $\imath$, $\jmath$ as

$$\Delta = G \sum_{\imath,\jmath} U_\imath V_\jmath \tag{2.37}$$

where U and V are known as the emptiness and fullness factors, respectively and are expressed by

$$U_i = \frac{1}{\sqrt{2}}\left[1 + \frac{(\epsilon_i - \lambda)}{\sqrt{(\epsilon_i - \lambda)^2 + \Delta^2}}\right]^{\frac{1}{2}}, V_i = \frac{1}{\sqrt{2}}\left[1 - \frac{(\epsilon_i - \lambda)}{\sqrt{(\epsilon_i - \lambda)^2 + \Delta^2}}\right]^{\frac{1}{2}} \tag{2.38}$$

The G factor in Eqn. 2.37 is known as the pairing strength which is dependent on whether the nucleon is a proton or neutron and the total mass A of the nucleus. Commonly used values of $G_p = 17/A$ and $G_n = 23/A$ are used. A plot of the ratio $(\epsilon_i\text{-}\lambda)/\Delta$ versus V^2 is shown on the right hand side of Fig. 2.11. One may note $V^2 \rightarrow 1$ for $(\epsilon_i\text{-}\lambda) \ll 0$ and $V^2 \rightarrow 0$ for $(\epsilon_i\text{-}\lambda) \gg 0$. Since U^2 acts oppositely to the same conditions and that $U^2 + V^2 = 1$, ${U_i}^2$ may be regarded as the probability the i^{th} orbital is empty and ${V_i}^2$ is the probability it is filled. Therefore, in the presence of pairing, the amount of energy needed to promote a particle to a higher single-particle state $(\epsilon_i\text{-}\lambda)$ is replaced by the energy, E_i, necessary to excite a quasiparticle given by

$$E_i = \sqrt{(\epsilon_i - \lambda)^2 + \Delta^2} \tag{2.39}$$

It is no longer proper to speak of the particles and holes now, but rather *quasiparticles* partially filling levels.

The big energy gap between the ground state and the first two-quasiparticle structures in even-even nuclei is now precisely described by Equation 2.39. A two-quasiparticle state would require an excitation of

$$E^{e-e}_{x_{ij}} = \sqrt{(\epsilon_i - \lambda)^2 + \Delta^2} + \sqrt{(\epsilon_j - \lambda)^2 + \Delta^2} \tag{2.40}$$

A minimum of 2Δ in energy is required before any simple two-quasiparticle excitation may be obsrved in even-even nuclei. In fact, most two-quasiparticle structures occur at $\sim$ 1.5-2.0 MeV and typical values of Δ for even-even nuclei range from 0.7-1.0 MeV. The reason for the lower than the expected band head states from particle excitation in odd-A nuclei may also be empirically seen by Equation 2.39. The excitation energy for an excited quasiparticle state will be

$$E^0_{x_\imath} = E_\imath - E_0 = \sqrt{(\epsilon_\imath - \lambda)^2 + \Delta^2} - \sqrt{(\epsilon_0 - \lambda)^2 + \Delta^2} \tag{2.41}$$

where $\mathrm{E}_0(\epsilon_0)$ is the quasiparticle (single-particle) energy of the orbit nearest the Fermi level. The effect lowers the excitation energies of orbitals near the Fermi surface and actually decreases quasiparticle excitations by Δ at $(\epsilon_\imath - \lambda) \gg \Delta$.

2.7.1 The Coriolis Anti-Pairing (CAP) Effect

The Coriolis force is produced by a body moving with a velocity $\vec{v}$ on a rotating system animated by an angular velocity $\vec{\omega}$. The effect of the Coriolis force is an apparent deflection of the path of this object, which does not actually deviate from its path, but rather appears to do so because of the motion of the coordinate system. Since we live on the earth - a rotating planet, the Coriolis effect is very common. The resulting ocean currents, weather patterns and the vortices formed during the draining of our bathtubs are accepted consequences of these forces. Nevertheless, the forces are generally weak, and they do not affect our human activities. This is probably the reason why only advanced studies in Physics deal with this phenomenon.

It turns out that nuclear rotation generates inertial forces, which simulate the effects of electric and magnetic fields. As in the case of any rotating system, the

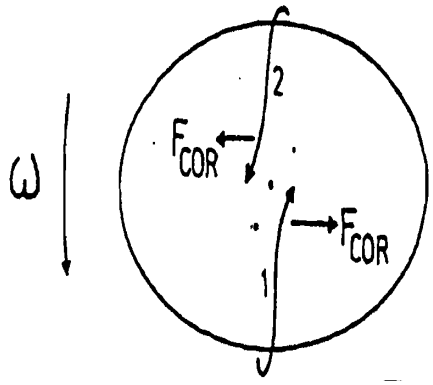

Figure 2.12: The classical picture of the Coriolis force on two nucleons (1 and 2) moving in a rotating system.

inertial forces can be separated into centrifugal and Coriolis forces. The former act radially and result in a stretching of the nucleus. The effect is analogous to the stretching of a polar molecule by the application of an electric field. The Coriolis force takes the form:

$$\mathbf{F}_{Cor} = -2m\vec{\omega} \times \vec{v} \tag{2.42}$$

where m is the mass (i.e. nucleon in our case) and $\vec{v}$ the velocity of the moving object (nucleon). This expression inescapably reminds us of the force $e\vec{v}\times\vec{\mathbf{B}}$ on an electric charge e, moving with velocity $\vec{v}$ in a magnetic field $\vec{\mathbf{B}}$. Thus, the effects of these forces are similar to those induced by electric and magnetic fields [44].

At low spins($\sim 10\hbar$) the nucleus displays well established superfluid properties with nucleons teaming up in time reversed orbits, or "Cooper pairs". For two nucleons paired together in time reversed orbitals, an increase in rotational frequency ω will increase the Coriolis interaction, which acts in opposite directions for each nucleon, as shown in Fig. 2.12. When the Coriolis force becomes greater than the pairing energy for two nucleons, at a certain critical rotation frequency (ω_c), the pairing cor-

relations will be quenched completely. This process is the analogue of the quenching of superconductivity by a sufficiently high magnetic field, and it is called the Coriolis Anti-pairing (CAP) effect, first discussed by Mottelson and Valatin in 1960 [45]. This can be interpreted as the breaking of the nucleonic pair, aligning the spins of both nucleons with that of the collective motion, so that the nucleons give a non-vanishing contribution to the total angular momentum of the nucleus. This effect is known as backbending and denotes a change in the intrinsic structure of the nucleus. In fact, in 1971 Johnson et al. [46] found, for the first time, a sudden change (*i.e.* backbending) in the ground-state rotational bands of ^{162}Er and ^{158,160}Dy.

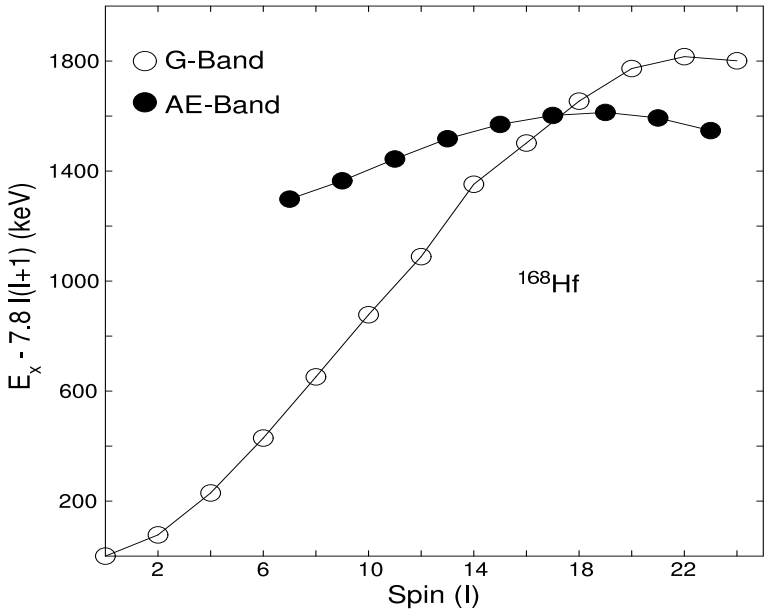

Figure 2.13: An example of band crossing in ^{168}Hf. The figure depicts excitation energies of bands G and AE as a function of spin relative to a rigid-rotor reference.

In the region between 10 and 20 units of angular momentum ($\hbar$), the backbending anomaly can be observed in the transition energies of the ground-state rotational bands of many deformed nuclei. The nuclear excitation energy is observed to deviate

from the expected rigid rotor I(I+1) dependence. If we look at a certain plot (Fig. 2.13) of spin against frequency, the curve will be found to move backwards (to the left) in the crossing spin region. But at a higher frequency, the curve again moves to the right. The term backbending arose from the "S" shape of the curve seen in the plot, since the moment of inertia bends back and up.

2.7.2 Theoretical Quasipartcle Energy Diagrams

The quasipartcle Routhian with pairing is given as

$$h'_{q.p.} = h'_{s.p.} - \Delta(P^+ + P) - \lambda\hat{N} \tag{2.43}$$

where the single-particle Routhian

$$h'_{s.p.} = h_{s.p.}(\beta) - \omega j_x \tag{2.44}$$

contains the single-particle angular momentum and the single-particle Hamiltonian $h_{s.p.}$ which in this case has the Nilsson potential. The Nilsson potential is described by a set of deformation parameters represented by β. The operator P^+ creates a pair field with a fixed strength defined by the pairing strength parameter Δ. The chemical potential λ determines the expectation value of the particle number $\hat{N}$ which is fixed to the number of protons or neutrons of the nucleus under consideration.

2.7.3 Shape Vibrations

Vibrations, in addition to rotation, are also one of the collective excitation modes of the nucleus. One of the bands of this work (BE) has the nature of octupole vibrations in ^{168}Hf. It corresponds to a type of oscillation of the shape of the nucleus.

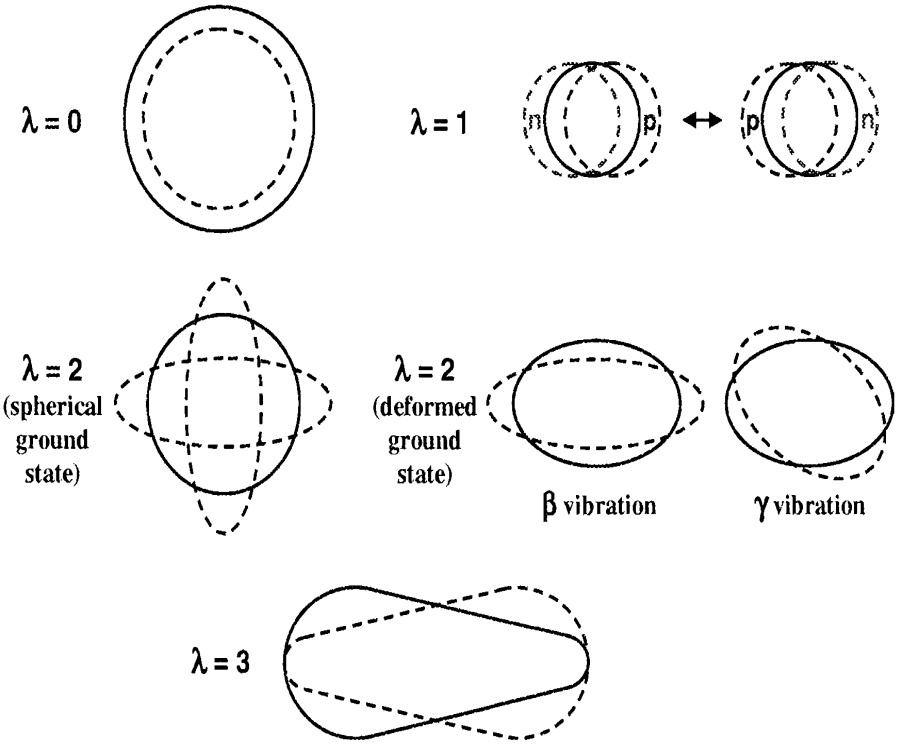

Figure 2.14: Schematic of the different modes of nuclear vibration.

When a spherical nucleus absorbs small amounts of energy, its density distribution can start to vibrate around the spherical shape. The magnitude of this vibration can be described by the coefficients $\alpha_{\lambda\mu}$ defined in Equation 2.8 in section 2.4.1. For small amplitude vibrations, the Hamiltonian for a vibration of multipole order λ, which is actually the difference between the energy of the deformed shape corresponding to the vibration and the energy of the nucleus at rest, can be written as:

$$H_\lambda = \frac{1}{2}C_\lambda \sum_\mu \left|\alpha_{\lambda\mu}\right|^2 + \frac{1}{2}D_\lambda \sum_\mu \left|\frac{d\alpha_{\lambda\mu}}{dt}\right|^2 \tag{2.45}$$

With the assumption that the different modes of vibrational excitation are independent from one another, the classical equation of motion can be obtained from the above Hamiltonian,

$$D_\lambda \frac{d^2\alpha_{\lambda\mu}}{dt^2} + C_\lambda \alpha_{\lambda\mu} = 0 \tag{2.46}$$

Therefore, a small vibration can be considered as an harmonic oscillation with the amplitude, $\alpha_{\lambda\mu}$, and the angular frequency, $\omega_\lambda = \left(\frac{C_\lambda}{D_\lambda}\right)^{1/2}$. The vibrations are quantized where the quanta are called phonons, and $\hbar\omega_\lambda$ is the quantity of vibrational energy for the multipole λ. Each phonon is a boson carrying angular momentum $\lambda\hbar$ and a parity $\pi = (\text{-}1)^\lambda$. The different modes of low order vibrational excitation ($\lambda =$ 0, 1, 2, 3) are illustrated in Fig. 2.14.

2.8 Electromagnetic Properties of Deformed Nuclei

2.8.1 Electric Quadrupole Moment

The nuclear quadrupole moment is one of the most important properties of a deformed nucleus, and the observation of large quadrupole moments in nuclei away from closed shells is one of the best direct evidences for the existence of stable nuclear deformation. The intrinsic quadrupole moment, Q_0, in the body fixed frame of a deformed nucleus rotating about its z-axis can be defined in terms of the charge distribution in the nucleus, $\rho_e(r)$, and, hence, of the nuclear shape, as:

$$Q_o = \int (3z^2 - r^2)\rho_e(r) d^3r \approx \left(\frac{8Z}{5}\right)\left(\frac{a-b}{a+b}\right) r_o^2 \tag{2.47}$$

where a and b are the lengths of the major and minor axes of the nucleus, respectively, and $r_o = \frac{a+b}{2}$. Therefore, the nuclear quadrupole moment is a direct measure of the nuclear deformation, i.e., for a spherical shape, $Q_o = 0$; for a prolate shape, $Q_o >$

0; and for an oblate nucleus, $Q_o < 0$. The Q_o moment can also be related to the deformation parameter, β_2. In axially symmetric nuclei with quadrupole deformation only, the first order expression can be given as:

$$Q_o = \left(\frac{3Z}{\sqrt{5}\pi}\right) r_o^2 \beta_2 \tag{2.48}$$

Generally, the experimental quadrupole moments measured in the laboratory frame are the spectroscopic quadrupole moments, Q_{spec}. From Ref. [47], the intrinsic quadrupole moment, Q_o can be obtained by projecting the spectroscopic quadrupole moment onto the frame of reference fixed on the nucleus through the following relation:

$$Q_o = \frac{(I+1)(2I+3)}{3K^2 - I(I+1)} Q_{spec} \tag{2.49}$$

where K is the projection of I onto the symmetry axis, as described in Section 2.5.5. For a K = 0 band, such as the ground state band in even-even nuclei, this relation has the simpler form:

$$Q_o = \frac{(I+1)(2I+3)}{I(2I-1)} Q_{spec} \tag{2.50}$$

Moreover, the experimental transition quadrupole moment, Q_t, which can be derived from the measurement of the lifetime of a state , is related to the Q_o moment by the relation [48]:

$$Q_t(I+1) = \sqrt{Q_o(I) Q_o(I+2)} \tag{2.51}$$

2.8.2 Magnetic Moment

In contrast to the nuclear electric moment, the nuclear magnetic moment reflects the contribution of the individual nucleons inside the nucleus. It is convenient to separate the orbital and spin contributions of the neutrons and protons. The magnetic moment operator can be expressed as:

$$\hat{\mu} = \mu_N \sum_{i=1}^{A} [g_{li} l_i + g_{si} s_i] \tag{2.52}$$

where μ_N is the nuclear magneton, g_{li} and g_{si} are the orbital and the spin gyromagnetic ratios (the gyromagnetic ratio is the ratio of the magnetic dipole moment to the angular momentum of a nucleus), respectively. Besides this contribution, the rotation of the core as a whole, *i.e.*, the collective rotation, contributes to the nuclear magnetic moments. In units of the nuclear magneton, the latter contribution is proportional to the angular momentum of rotation, R. Combining all of the contributions together, the magnetic moment operator can be written, after some mathematical treatment, as:

$$\hat{\mu} = g_R I + [g_K - g_R] \frac{K^2}{I+1} \tag{2.53}$$

The observed nuclear magnetic moment is the expectation value of the magnetic moment operator on a nuclear state |I,K>:

$$\mu = \langle I, K | \hat{\mu}_z | I, K \rangle \tag{2.54}$$

where I is the total angular momentum, K is the projection of I onto the symmetry axis, and the z-axis is the axis of rotation.

2.8.3 γ-ray Angular Correlations and the DCO Ratio

A γ-ray with multipolarity λ is either electric (denoted by Eλ) or magnetic (denoted by Mλ), or a mixture of these. Emitting a γ-ray with multipolarity changes the spin I of the nucleus acccording to

$$|I_i - I_f| \leq \lambda \leq |I_i + I_f| \tag{2.55}$$

where the indices i and f denote initial and final, respectively. The change in parity π for Mλ and Eλ transitions is ruled by

$$\begin{aligned} \pi_i \cdot \pi_f &= (-1)^{\lambda}; \quad \text{for} \quad \text{E}\lambda \quad \text{transitions} \\ \pi_i \cdot \pi_f &= (-1)^{\lambda+1}; \quad \text{for} \quad \text{M}\lambda \quad \text{transitions} \end{aligned} \tag{2.56}$$

The angular intensity distribution, W(θ, ϕ), of the γ-rays depends on the multipolarity λ of a transition. Consequently, by analyzing the intensity at different angles the multipolarity can be determined, but not the electric or magnetic nature of the transition. For example, compare the angular distributions of the electric or magnetic fields from oscillating dipoles and quadrupoles. The analogy also explains why electric or magnetic transitions can not be distinguished because the far fields from electric or magnetic multipoles do not differ.

The angular distribution is only measurable when the emitting nuclei have some kind of non-uniform orientation. In heavy-ion collisions, the spin of the compound nucleus points in a direction perpendicular to the incoming beam.

The angular distribution of the photons will thus be symmetric in the forward and backward directions and independent of the azimuthal angle ϕ. For the perfect alignment of the nucleus, the angular distribution is

$$W(\theta, \phi) = W(\theta) = 1 + A_2 P_2(cos\theta) + A_4 P_4(cos\theta) + ... \tag{2.57}$$

However, in the real world the alignment of the spin is not perfect and the attentuation factors α_2 , α_4 , ... are introduced to deal with this. In heavy-ion experiments, the alignment is found to have a Gaussian distribution and thus the attentuation factors are uniquely dependent on each other. Higher orders of attentuation factors are normally negligible and the angular distribution becomes

$$W(\theta) = 1 + \alpha_2 A_2 P_2(cos\theta) + \alpha_4 A_4 P_4(cos\theta) \tag{2.58}$$

The coefficients A_2 and A_4 depend on the initial and final spin, the initial and final angular momentum of the transition and eventually the mixing ratio δ.

One way to utilize this concept to measure the multipolarity of a transition is to deduce what is known as its DCO (Directional Correlation of Oriented nuclei) ratio. In this case at least two detectors, placed at different angles, θ_1 and θ_2, are needed. Let I denote the intensity of a transition, γ the transition of which the multipolarity is to be measured and γ_G a transition with a known multipolarity. Then the DCO ratio can be expressed as:

$$R_{DCO} = \frac{I(\gamma \quad at \quad \theta_1 \quad gated \quad by \quad \gamma_G \quad at \quad \theta_2)}{I(\gamma \quad at \quad \theta_2 \quad gated \quad by \quad \gamma_G \quad at \quad \theta_1)} \tag{2.59}$$

The expected DCO ratios for transitions with a certain multipolarity can then be calculated as a function of θ_1 and θ_2.

CHAPTER III

LIFETIME MEASUREMENTS USING THE DOPPLER SHIFT ATTENUATION METHOD

3.1 Doppler-Shift Methods

Normal deformed (ND) states typically have mean lifetimes in the range of 0.1 ps to ∼1 ps, which are too short for direct electronic timing methods to apply. Electronic timing is able to measure lifetimes to only $\sim 10^{-11}$s. Lifetimes of excited nuclear states in the 10^{-14}s to 10^{-9}s range can be measured with Doppler-shift methods, the recoil distance plunger method (RDM) and the Doppler-shift attenuation method (DSAM). These techniques utilize the fact that, after a nuclear reaction has occurred, the velocity of a recoiling nucleus in an excited state may be obtained, at the moment of the γ-ray decay of that state, by measuring the Doppler energy shift of the γ ray.

In the RDM, after leaving a target, the nuclei excited by a reaction move freely in a vacuum until they are quickly stopped (< 0.5 ps) by a movable plunger. The plunger typically moves from 1 μm to 1 cm from the target. Because of the Doppler shift, the energies of the γ-rays emitted by the stopped and moving nuclei are different. Knowing the velocity of the recoiling ions and, consequently, the time it takes them to reach the plunger, makes it possible to obtain lifetimes in the range of 10^{-9}-10^{-12}s. Since the RDM was not used in this work, it will not be discussed further. In the

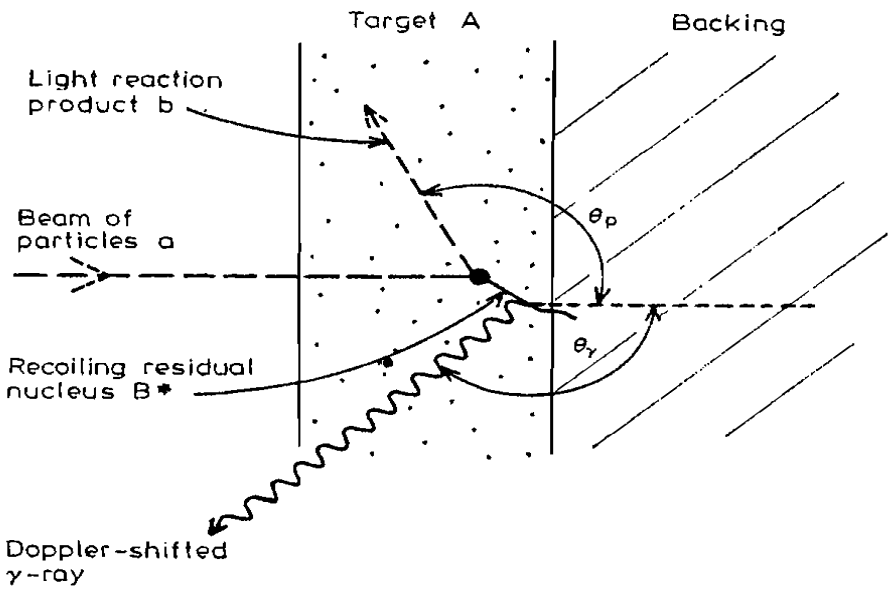

Figure 3.1: The principle of the Doppler shift attenuation method of measuring lifetimes in the residual nucleus B*, formed in the reaction A(a, b)B*. The recoiling nucleus B* slows in the material of the target and backing while emitting a γ-ray with the mean lifetime τ of the excited state. Adopted from Ref. [49].

DSAM the lifetime of a level emitting a γ-ray is typically compared with the slowing time of a recoiling nucleus in a target and backing. The basic method is illustrated in Fig. 3.1. A beam of incoming particles **a** impacts the target nuclei **A**. Reaction products **b** are emitted, leaving the final nucleus $\mathbf{B}^*$ in the excited state whose lifetime is to be measured. From an initial recoil velocity v_o the excited nucleus slows in the target and backing. When the mean recoil velocity has dropped to v, a γ-ray is emitted. v is determined experimentally by measuring the average Doppler shift of the emitted γ-rays. The Doppler shift is given by

$$E(\theta) = E_o\,(1 + \beta \cos\theta) \tag{3.1}$$

where $\beta = v/\mathrm{c}$, E is the average detected γ-ray energy at the angle θ, E_0 is the energy of the γ-ray in the reference frame of the nucleus, and θ is the angle of γ-ray emission with respect to the direction of the incoming beam of particles.

v now needs to be related to the time of emission. Knowing the stopping power of the target and backing material allows the determination of the velocity of the recoiling nucleus as a function of time from the force equation

$$\frac{dE}{dx} = -M\frac{dv}{dt} \tag{3.2}$$

In the above relation $\frac{dE}{dx}$ is the stopping power of the material in which the nucleus is traveling, M is the mass of the recoiling nucleus, and $\frac{dv}{dt}$ is the rate of change of the nucleus's velocity. Use of this equation provides a clock to measure time from the instant of compound nucleus formation until the nucleus either exists or stops in the backing.

3.2 Stopping Powers

The major systematic error in the DSAM depends on determination of stopping powers. The discussion of heavy-ion stopping powers can be separated into three velocity regions:

• Low velocity, where $\frac{v}{c} \leq 0.5\%$. Nuclear stopping is the dominant mechanism for energy loss.

• Medium velocity, where $0.5\% \leq \frac{v}{c} \leq 1.5\%$. Nuclear and electronic stopping are almost equal.

• High velocity, where $\frac{v}{c} \geq 1.5\%$. Electronic stopping is the dominant mechanism for energy loss.

Nuclear stopping results from the scattering of the recoiling nucleons by the Coulomb and nuclear fields of the nuclei in the stopping material. Since the recoiling nuclei and the nuclei with which they interact have comparable masses, there are relatively large energy losses and changes in direction per collision. However, only small amounts of experimental stopping power data are available in this velocity region, so it is conventional to use theoretical estimates of stopping cross sections when calculating the heavy-ion energy loss. The treatment of the slowing process for low- and medium-velocity ions by Lindhard et al. has been widely accepted [50]. Lindhard wrote the rate of energy loss in the form

$$\frac{dE}{dx} = \left(\frac{dE}{dx}\right)_e + \left(\frac{dE}{dx}\right)_n \tag{3.3}$$

where the subscripts e and n refer to the electronic and nuclear contributions to the stopping, respectively. The nuclear stopping power $\left(\frac{dE}{dx}\right)_n$ was calculated by Lindhard from numerical solutions of the Thomas-Fermi equation. An analytic expression that fit the nuclear stopping cross sections, obtained by Lindhard, was given by Winterbon et al. [51]. As previously mentioned, recoiling nuclei in the nuclear stopping regime experience large directional changes. Since DSAM measurements are interested in the component of velocity along the initial recoil direction, the equations of Lindhard and Winterbon must be modified. Blaugrund has given a formulation that takes the directional changes into consideration [52]. Currie [53] used a Monte-Carlo method that achieved essentially the same results as Blaugrund's approach. It has become commonplace to use $\left(\frac{dE}{dx}\right)_n$ as calculated by the Lindhard-Winterbon-Blaugrund formulation as the nuclear stopping power in the DSAM. Electronic stopping powers are then determined by more empirical methods, as discussed below.

Electronic stopping involves the interaction of the recoiling nuclei with atomic electrons. The recoiling nuclei are always much heavier than the electrons with which they interact. Consequently, it will take many collisions, resulting from the Coulomb forces, before the energy of a recoiling nucleus is lost. The electronic stopping process can therefore be regarded as continuous, with no change in direction of the recoiling nucleus.

Although it is relatively easy to measure heavy-ion stopping powers for the $\frac{v}{c} \geq 3\%$ region, only a few measurements have been made. Hence, to a lesser extent, the determination electron stopping powers again relies on the calculations of models. Northcliffe and Schilling [54] have compiled a semi-empirical table of stopping powers for heavy ions. The compilation was based on measured proton stopping powers, with the assumption of smooth variations between the measured points for different stopping materials. The stopping powers for ions other than protons were then derived by the introduction of an effective charge of the moving ion γZ_1

$$(\gamma Z_1)^2 = \gamma_p^2 \, (dE/dx)_{HI} \, / \, (dE/dx)_P \tag{3.4}$$

where $(dE/dx)_{HI}$ and $(dE/dx)_P$ are at the same velocity in the same material. γ_P is the effective charge of the proton and is unity for proton energies $\geq$0.5 MeV. The parametrization of Pierce and Blann [55] is often used for the effective charge

$$\gamma = 1 - e^{-0.95 v} R \tag{3.5}$$

where v_R is the reduced velocity $v/v_o {Z_1}^{2/3}$. With the aid of more extensive measurements on ^{4}He stopping powers, a typical expression for the effective charge parametrization became [56]

$$\gamma = 1 - A(Z_1)e^{-0.87v/(v_o Z_1^{0.65})} \tag{3.6}$$

with

$$A(Z_1) = 1.035 - 0.4e^{-0.16Z_1} \tag{3.7}$$

Ziegler and Chu [57] illustrated that ^{4}He stopping powers show a strong periodic dependence on the atomic number of the stopping materials Z_2. The stopping material exhibits a pronounced shell structure effect, which decrease with increasing incident particle energy. It becomes almost negligible for incident particle energies > 1 MeV/A. In light of the observed shell effects Ward [56] suggested that the Northcliffe and Schilling calculations be scaled to the measured ^{4}He stopping powers.

3.3 Sidefeeding

The in-band γ-ray intensity of ND cascades generally increases with decreasing transition energy until a plateau is reached. This means there are unobserved states that feed the in-band ND levels. When a ND state emits a γ ray, the velocity of the nucleus can be viewed as a function of that ND state's intrinsic lifetime and of all the lifetimes of the preceding states. The ND state's apparent lifetime reflects the time history of the feeding cascade, thus, the lifetimes of the unobserved sidefeeding states must be considered when calculating the in-band ND lifetimes. This unknown sidefeeding will introduce additional uncertainties into the calculated in-band ND lifetimes. However, the uncertainty can be reduced by analyzing spectra which are produced by gating on top of the ND band of interest. Gating-on top of a ND band

is a requirement that one or more of the γ rays detected in a coincidence event be at an energy equal to a high-energy transition in the ND cascade of interest. This basically constrains all intensity in the ND spectrum to pass through the high energy transitions upon which gates are set. Consequently, sidefeeding to ND states below the transition energies used for gating is eliminated.

Gating-on-top is possible with the largest and most modern γ-ray arrays, such as Gammasphere. Unfortunately, in this work, gating on top reduced the statistics such that Doppler-shift measurements could not be performed. Hence, the effect of the sidefeeding states is the main uncertainty in lifetime values for ^{168}Hf.

3.4 Lineshapes

To study lifetimes for the transitions of a rotational band, a Doppler-shift attenuation program "LINESHAPE" [58], developed by Bacelar et al. [59] and Gascon et al. [60], has been used. This program has been extensively modified and combined with the least- squares minimization routine MINUIT, written by James and Roos [61]. MINUIT includes minimization routines MIGRAD, SIMPLEX, and SEEK, and the error routine MINOS.

SIMPLEX, by Nelder and Mead [62], uses the simplex method for the minimization of a function of N parameters. The method depends on the comparison of the function values at the N+1 vertices of a general simplex followed by the replacement of the vertex with the highest value by another point. A simplex is the smallest N-dimensional geometrical figure with N+1 vertices: a triangle for N=2, a tetrahedron for N=3, etc. New simplices are formed by reflecting one point in the hyperplane of the other points.

The simplex adapts itself to the local landscape of the function, elongating down inclined planes, changing direction upon encountering a valley at an angle, and contracting in the neighborhood of a minimum.

MIGRAD, a gradient search method using Fletcher's switching variation [63] to the Davidon-Fletcher-Powell variable matrix algorithm [64], approaches a local minimum closely and generates parabolic error estimates, which would be true errors if the chi-square function were really quardatic with respect to each parameter.

SEEK performs a minimization using a Monte Carlo technique. The parameter values are chosen randomly according to uniform distributions centered at the best previous set of values. If chi-square is lower for these new values, they become the starting point for the next iteration, otherwise the previous set remains the starting point as the process is continued through a series of iterations.

MINOS finds the true positive and negative errors (confidence intervals) of a parameter by examining the behavior of chi square in the vicinity of the best value of the parameter. The value of the parameter of interest is varied in steps, both increasing and decreasing from its best value, and at each step, chi-square is reminimized by varying the N-1 remaining parameters. This process is continued until chi-square increases by one unit.

LINESHAPE calculates the γ-ray lineshapes and extracts lifetimes by fitting the experimental data. Detailed descriptions of the method and its application can be found in reports of recent lifetime measurements for Hf isotopes [65-67]. The magnitude and direction of the velocity, so-called "velocity profile", for the recoiling ions in the target and backing materials was calculated in a Monte Carlo fashion [53]. In the calculation for the slowing down process, both electronic and nuclear stopping powers were considered. For the electronic stopping power, the tabulated values of Ref.

[54], corrected for the α-stopping power [57], were used. For the nuclear stopping power, a multiple Coulomb scattering formalism was used [50]. From the velocity profile distribution, a set of γ-ray peak shapes at each time step was obtained for each γ-ray angle and were stored in a "shape-versus-time" matrix. To reproduce the lineshapes, the γ-ray yield per time step was calculated by using the solution of the Bateman's equation [68]. The calculated lineshapes were then obtained by summing the independent lineshapes at each time step, weighted by summing the γ-ray yield.

In order to fully analyse these lineshapes three gated γ-γ coincidence matrices were generated using the thick target data: one with coincidence events between the ten detectors at 50° and the other detectors; the second with the ten 130° detectors and others; and the third matrix with coincidence events between the 90° detectors and the others. In order to observe the Doppler shifted transitions, 1D spectra were obtained by gating the 2D matrices on lower states of a rotational band and summing over all the clean gates for the forward and backward angle detectors. Spectra from the 90° detectors also were obtained for comparison.

The LINESHAPE program assumes that a rotational band, with the known discrete-line energies and a set of rotational transitions with the same moment of inertia, precedes the highest-spin transitions. The lifetime τ of an E2 transition with energy E_γ is

$$1/\tau = 12.2{E_\gamma}^5 B(E2, I \rightarrow I-2), \tag{3.8}$$

$$\text{where} \quad E_\gamma = \frac{4I-2}{2J^{(2)}/\hbar^2}, \tag{3.9}$$

B(E2, I $\rightarrow$ I-2) is given in Equation 2.58 where τ is in ps, E_γ in MeV, and B(E2, I $\rightarrow$ I-2) in e^2b^2. A sidefeeding cascade with a constant moment of inertia is linked to

each level. For each level, the sidefeeding intensity is obtained experimentally and the sidefeeding time is controlled by a parameter, Q_s being included in the fit. Thus, the lifetime of a state and its corresponding sidefeeding times were fitted for each γ-ray transition, starting from the highest level to the lowest six.

CHAPTER IV

THE EXPERIMENTAL TECHNIQUES

4.1 The Fusion-Evaporation Reaction

A persistent technique in science to investigate a physical system is to view it under extreme conditions. For example, one of the ways of studying a nucleus is by observing how it responds to stress and stain, e.g. input angular momentum and excitation energy. The fusion-evaporation reaction has proven to be an extremely useful tool in the studies of nuclear structure physics. With heavy ions, this reaction imparts large amounts, up to the fission limit, of energy and angular momentum to the compound nucleus, and allows the observation of some unstable nuclei as well. However, the current sources of heavy ions (or stable ions) are abundant in nature and thus, only a limited number of nuclei can be produced in this fusion-evaporation reaction due to the lack of stable beams and targets. Currently, advanced radioactive beam facilities are under development and an incredible knowledge in nuclear structure physics can still be achieved.

In order to create a highly excited nucleus, a suitable ion beam and target material are chosen for fusion such that the beam must be high enough to overcome the Coulomb repulsion of two nuclei. A linear accelerator or a cyclotron are generally used for this task. Once a highly-excited and rapidly rotating compound nucleus

is formed, it decays, after about 10^{-19}s, by emitting protons, neutrons, and alpha particles. The so called emitted or evaporated particle not only loses most of the excitation energy, but also loses little ($\sim$ 1-2 $\hbar$) angular momentum. This process continues until the energy of the nucleus is about 10 Mev above the yrast line - a state at which the emission of γ rays begins.

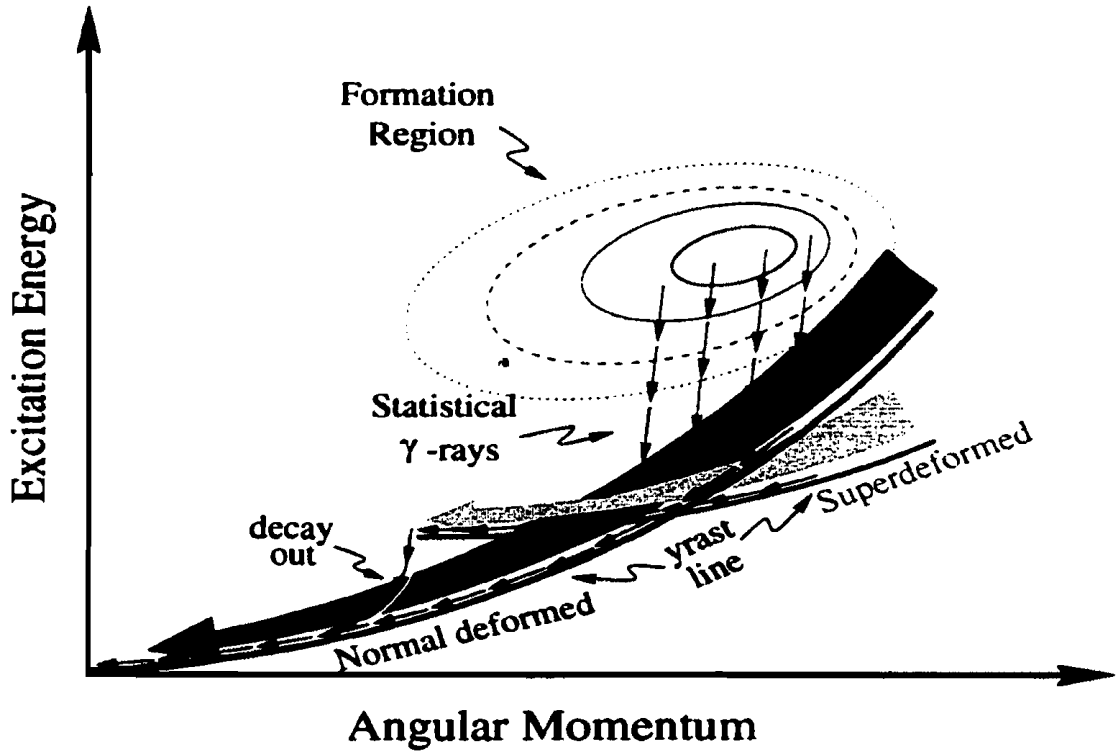

Figure 4.1: Diagram illustrating the de-excitation mechanism for a heavy ion fusion-evaporation reaction [69].

During the early stage (statistical cooling phase) of γ-ray emission, very strong electric dipole (E1) transitions are emitted from the "cooling" nucleus. [70]. As the nucleus approaches ($\sim$ 3 MeV) the yrast line, the nucleus de-excites mostly via higher multipole transitions [70]. At this final stage, the deformed nucleus emits discrete collective cascades, or bands, until both the excitation energy and angular

momentum are exhausted, (*i.e.* ground state), as shown in Fig. 4.1. The γ rays thus emitted from the de-exciting nucleus are then collected by detectors and later analyzed. This entire process, from the formation of the compound nucleus to decay to its ground state, takes about 10^{-9} seconds. Figure 4.2 illustrates the different stages of the fusion-evaporation reaction.

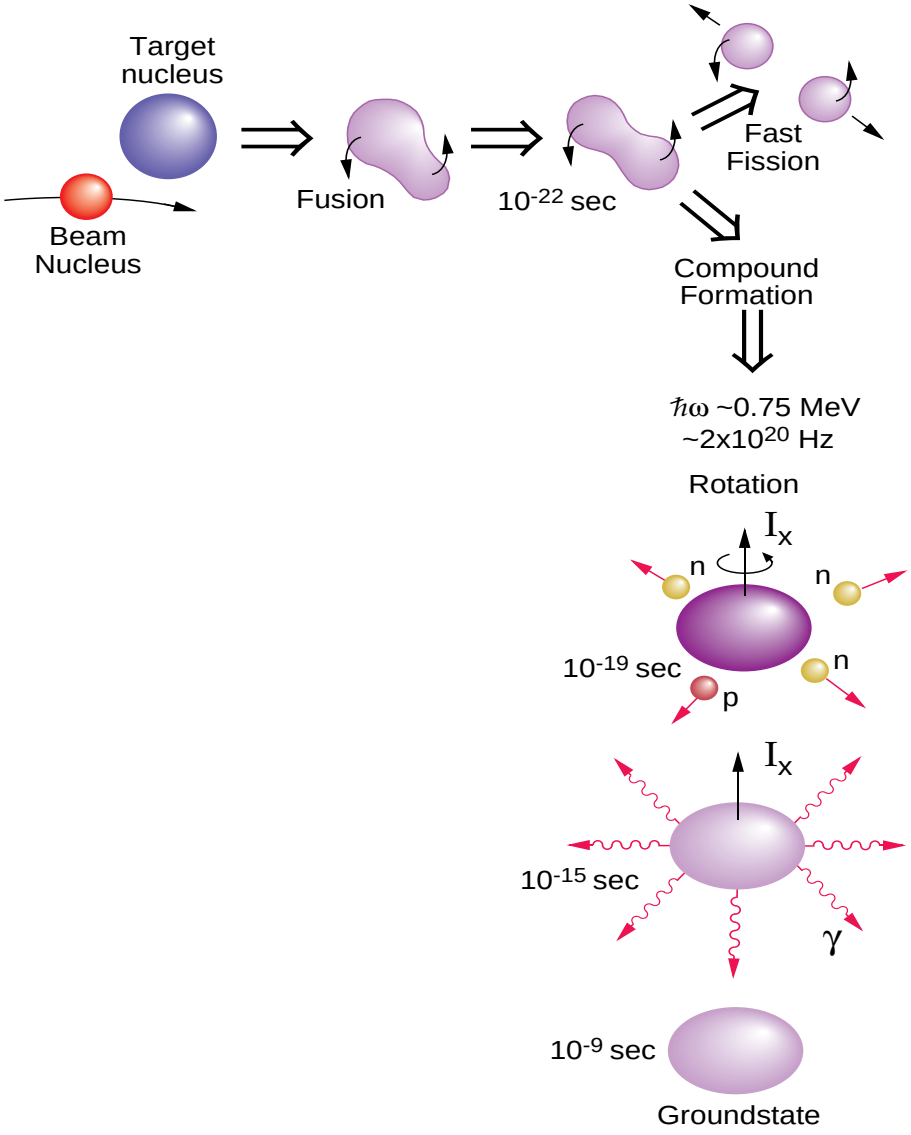

Figure 4.2: Diagram of the fusion-evaporation process [71].

4.2 Reaction Choice

While choosing a reaction, the physicist has to consider various factors, and the target is, of course, a major concern. It is very important that the target must be pure ($\sim$ 95 %), stable and available. Depending upon nuclear properties to be studied, the target may be either a thin self-supporting foil or a thick foil with Pb or Au backing. While a thin target ($\sim$ 500μg/cm^2) is chosen for coincidence γ-ray analysis to construct a decay or level scheme, a thick target ($>$ 1mg/cm^2) with a Pb or Au backing ($\sim$ 10 mg/cm^2) is preferred for lifetime measurements. For the thin target experiment, the peaks will suffer Doppler shifting while the thick target spectra may consists of both Doppler-broadened and non Doppler-broadened components, depending on the lifetimes of the corresponding states emitting the γ rays. One technique, *i.e.*, Doppler Shift Attenuation method to measure the lifetime from Doppler-broadened spectra, has been discussed in detail in Chapter III.

It is always advantageous for experimentalists to have high beam currents to record maximum counts, which is achieved from the proper combination of stable beam and target. Since the angular momentum and excitation energy introduced into the compound nucleus depend on the beam type, one must follow precaution while choosing a heavy or light beam. Generally, a computer code is employed in order to help choose a suitable beam and target combination. It is noted that using the heavier beam means the more spin to be introduced into the system. Once an appropriate beam-target combination is selected, the other task is to determine the minimum energy required for the beam-target fusion to occur.

The beam must have sufficient kinetic energy to overcome the Coulomb barrier, which can be calculated from the expression [72]:

$$V_c(R) = \frac{1}{4\pi\epsilon_o}\frac{Z_b Z_t e^2}{R} \tag{4.1}$$

where b and t represents the beam and target, respectively and

$$R = [1.36(A_b^{1/3} + A_t^{1/3}) + 0.5]fm. \tag{4.2}$$

Once the Coulomb barrier is found sufficiently low, the proper beam energy can be determined by doing calculations in detail.

4.3 Designing a Gamma-Ray Detector System

The Figures 4.3 and 4.4 illustrate a γ-ray detector system and its interior view, respectively. The most important properties of a γ-ray detector array are: (1) high efficiency[1] in detecting incident γ-rays, (2) high energy resolution resulting in very narrow energy peaks, (3) high ratio of full-energy to partial-energy events, and (4) high granularity to localize individual γ rays and reduce the probability of two γ-ray hits in one detector from the same event. For γ rays in the MeV range, by far the best combination of these properties is given by semiconductors made of high-purity germanium (Ge) crystals. The largest Ge crystals that can currently be produced commercially are cylinders about 10 cm in diameter and 10 cm long which, with about 30% relative efficiency for incident 1.3 MeV γ rays, produce a full-energy peak with a full width at half its maximum (FWHM) of about 2 keV at this energy. For

[1]The efficiency of a detector is defined as the ratio of number of counts in the 1332.5 keV peak from a ^{60}Co source placed 25 cm away to the number of counts observed in a 3" $\times$ 3" NaI crystal under the same conditions.

increases in both efficiency and granularity, these Compton-suppressed detectors are assembled into arrays. The first such array was set up in Europe in 1980 and consisted of five detectors whereas Gammasphere [73] has 110 Ge crystals, 70 of which have two independent elements, for a total of 180 separate detectors. Gammasphere will be discussed in detail in Section 4.6.

Figure 4.3: Gammasphere Detector Geometry [71].

4.4 Compton-Suppressed Ge Spectrometer

The dominant characteristic of Ge detectors is their excellent energy resolution[2] when applied to γ-ray spectroscopy. The great superiority of the Ge detector in energy resolution allows the separation of many closely spaced γ-ray energies, which remain unresolved in other detector system. Consequently, virtually all γ-ray spectroscopy that involves complex energy spectra is now carried out with Ge detectors. Of the various ways γ rays can interact in matter, only three interaction mechanisms have any real significance in γ-ray spectroscopy: (i) photoelectric effect (ii) Compton scattering, and (iii) pair production. Photoelectric effect predominates for low-energy γ rays (up to several hundred keV), pair production predominates for high-energy γ rays (above 5 - 10 MeV), and Compton scattering is the most probable process over the range of energies between these two extremes.

The photoelectric effect is an interaction in which the incident γ-ray photon is absorbed and a photoelectron is produced from one of the electron shells of the absorber atom with a kinetic energy given by the incident photon energy minus the binding energy of the electron in its original shell. Thus, the result of the photoelectric effect is the liberation of a photoelectron, which carries off most of the γ-ray energy, together with one or more low-energy electrons corresponding to absorption of the original binding energy of the photoelectron. If nothing escapes from the detector, then the sum of the kinetic energies of the electrons that are created must equal the original energy of the γ-ray photon. The photoelectric effect is therefore an ideal process if one is interested in measuring the energy of the original γ-ray.

[2]The energy resolution of a detector is defined as the ratio of the full width at half maximum (FWHM) to the mean or average pulse height, *i.e.* peak in the observed spectrum.

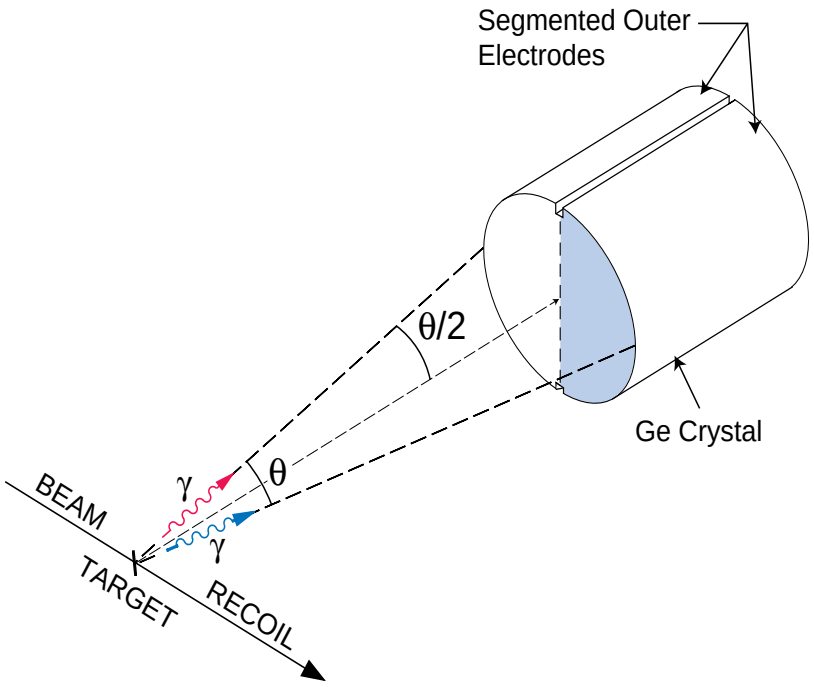

Figure 4.4: Segmented Ge crystal of Gammasphere [71].

Pair production is a nuclear process, which occurs when a high-energy photon, generally interacting with an atomic nucleus, produces a particle (electron) and an antiparticle (positron). It is the chief method by which energy from γ rays is observed in condensed matter.

The background of a γ-ray spectrum has two main sources. One stems from statistical decay of the hot nucleus and gives a quasi-continuum background. The other is caused by Compton scattering. Compton scattering is the process in which a photon scatters from an electron, thereby losing some of its energy. Because all angles of scattering are possible, the energy transferred to the electron can vary from zero to a large fraction of the γ-ray energy. When this occurs in a detector, the result is that the detected energy of the γ ray will be lower than the actual energy as a part of the γ ray escapes the detector. The Compton background can be substantially

reduced by detecting in the anti-Compton shield photons that are scattered out of the Ge detectors, and then discarding the corresponding Ge detector signals using anticoincidence.

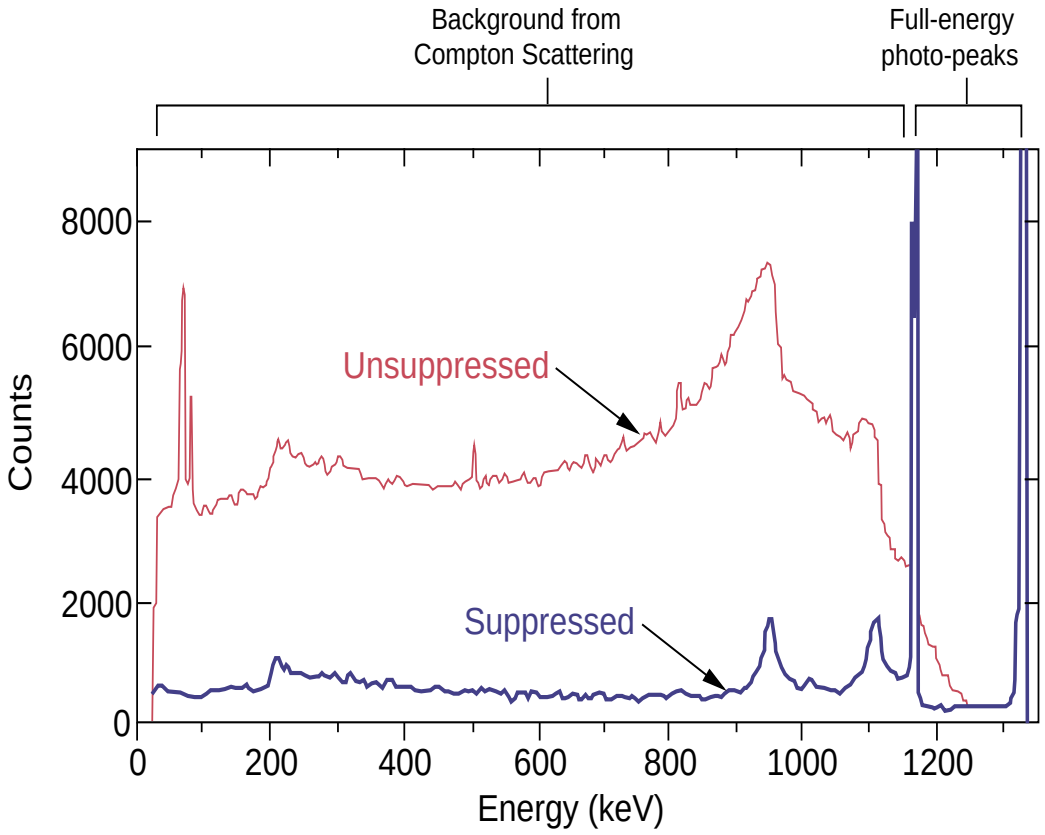

Figure 4.5: Effect of Compton background suppression [71].

Because of the cosmic radiation that can continuously bombard the earth's atmosphere and the existence of natural radioactivity in the environment, all radiation detectors record some background signal. The nature of this background varies greatly with the size and type of detector and with the extent of shielding that may be placed around it. Because the magnitude of the background ultimately determines the minimum detectable radiation level, it is most significant in those applications involving

radiation sources of low activity. However, background is often important enough in routine usage so that the majority of radiation detectors are provided with some degree of external shielding to effect a reduction in the measured level. Background radiations are conveniently grouped into five categories: (i) the natural radioactivity of the constituent materials of the detector itself, (ii) the natural radioactivity of the ancillary equipment, supports, and shielding placed in the immediate vicinity of the detector, (iii) radiations from the activity of the earth's surface (terrestrial radiation), walls of the laboratory, or other far-away structures, (iv) radioactivity in the air surrounding the detector and (v) the primary and secondary components of cosmic radiation.

4.5 The Principle of Compton Suppression

For a better ratio of full-energy to partial-energy events (called the peak-to-total, or P/T ratio), the Ge detectors are surrounded by a dense scintillator (bismuth germanate (BGO) being the most common), which detects γ rays Compton-scattered out of the Ge crystal and then electronically suppresses the partial-energy pulse left in the Ge detector (Figure 4.5). This results in an improvement in the P/T ratio for a 1.1 MeV gamma ray from about 0.25 for the bare crystal to about 0.6 when suppressed. This is an enormously important signal to background gain, without which high-fold[3] coincidence measurements would not be practical. For example, for a typical situation in Gammasphere when six γ rays hit separate Ge detectors, the fraction of events with full-energy photo-peaks rises by a factor of about 200 with Compton suppression.

[3]Fold is the number of γ rays detected in a given event.

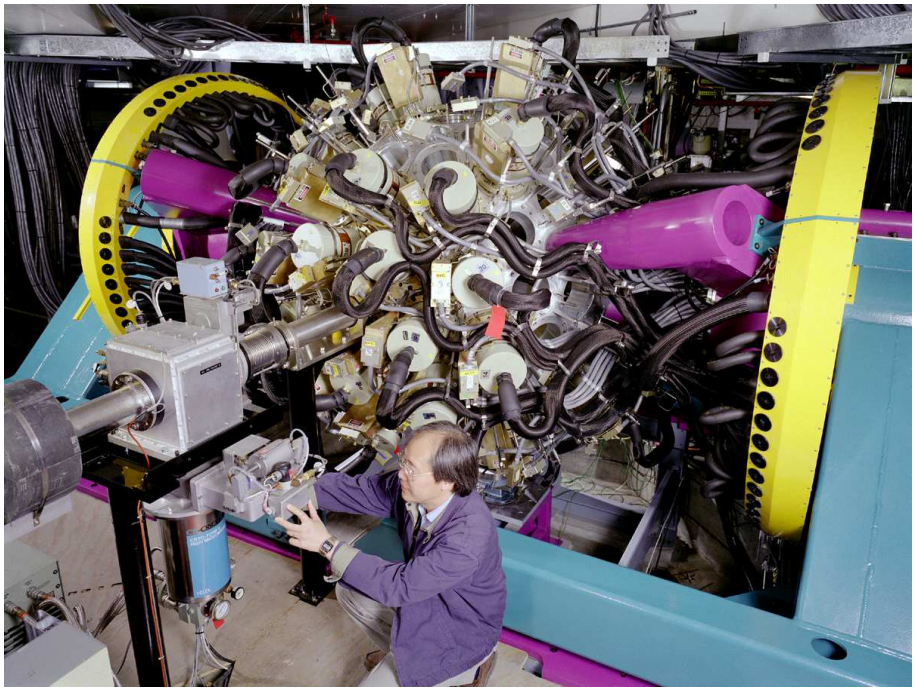

Figure 4.6: Gammasphere closed and ready for beam [71].

4.6 Gammasphere

Gammasphere is a γ-ray detector system that was designed to sensitively carry out high-fold γ-ray coincidence measurements. This gives a large resolving power, and makes it possible to identify weak cascades. The design goal was to achieve high efficiency, a good response function, high energy resolution and detectors resistant to neutron damage. The detector type that was chosen was a 4π array of n-type Ge detectors, mounted in 17 rings symmetric about the beam line, with BGO Compton suppressors. BGO (bismuth germanate $Bi_4Ge_3O_{12}$) is a very dense scintillation material. This makes it possible to detect a large fraction of the scattered γ rays, while the scintillator is kept small. The full energy efficiency of Gammasphere is about 9% at 1.3 Mev, which is a very high efficiency in this context, and its relative

energy resolution is around 0.2% at the same energy. The design of Gammasphere makes it possible to study nuclei at the limits of stability, e.g. nuclei near the drip lines or nuclei with high masses or angular momenta. Figure 4.6 shows a picture of Gammasphere. Detailed geometries of the detectors are listed in Table 4.1.

Table 4.1: Arrangement of detectors in Gammasphere.

Ring Number	Angle	Detectors
1	17.27	1,2,3,4,6
2	31.72	5,7,8,9,10
3	37.38	11,12,13,14,16
4	50.07	15,17,18,19,20,21,22,23,24,26
5	58.28	25,27,28,30,32
6	69.82	29,31,33,34,35,36,37,38,40,42
7	79.19	39,41,44,46,48
8	80.71	43,45,47,50,52
9	90.0	49,51,53,54,55,56,57,58,60,62
10	99.29	59,61,64,66,68
11	100.81	63,65,67,70,72
12	110.81	69,71,73,74,75,76,77,78,80,82
13	121.72	79,81,83,84,86
14	129.93	85,87,88,89,90,91,92,93,94,96
15	142.62	95,97,98,99,100
16	148.28	101,102,103,104,106
17	162.73	105,107,108,109,110

[a]The experiment performed with 101 Ge detectors in Gammasphere.
[b]Detectors 1 - 6, 10, 53, 58 were missing in this experiment.
[c]Detector # 36 removed after tape 4.

4.7 Technical Innovations-Electrically Segmented Detectors

For many of the Gammasphere experiments the energy resolution is dominated by the Doppler broadening due to the recoil motion of the nucleus emitting γ rays, which depends on the opening angle of the Ge detector. High granularity is needed to reduce this effect. To accomplish this, about 70 of the GAMMASPHERE detectors

have been electrically segmented into two D-shaped halves (Fig. 4.4). The high-resolution, total-energy signal is still read from a common electrode at the center of the detector while lower resolution signals can be read separately from each half thus indicating which side of the crystal was hit first. Thus, the effective angular size of the Ge detector is reduced by a factor of two. In typical experiments this improves the resolving power of Gammasphere by a factor of two. This innovation of creating electrically segmented Ge detectors, made by the Gammasphere collaboration, is now an established technique used by manufacturers around the world. This important technique has laid the technical foundation for the next generation of highly segmented detector arrays, "GRETA", the Gamma-Ray Energy Tracking Array, which is calculated to be about 1000 times more powerful than Gammasphere!

CHAPTER V

EXPERIMENTAL MEASUREMENTS AND RESULTS

5.1 Experiment Details

The two experiments by our group, the first using a thin target and the second using a thick target, were performed at the Argonne National Laboratory (ANL), USA.

In the experiment using the thin target, high-spin states in the nucleus ^{168}Hf were populated by the reaction ^{96}Zr (^{76}Ge, 4n) at a beam energy of 310 MeV. The beam was provided by the ATLAS accelerator at the Argonne National Laboratory. A self-supporting thin foil of ^{76}Zr (667 μg/cm^2) was used as a target such that the evaporation residues recoiled into vacuum. The γ rays emitted by the highly excited nuclei were measured with Gammasphere, which consisted of 101 Compton-suppressed detectors. The experiment lasted for about 96 hrs, and a total of 2.2 $\times$ 10^9 events were recorded on tape, with a requirement of $\leq$ 5 suppressed Ge detectors in prompt coincidence. Heavimet collimators were placed in front of the Ge spectrometers to reduce the background signals. A beam wobbling mechanism developed at ANL was used to deposit the beam particles to the target evenly in the area of 4 mm $\times$ 5 mm. This helped with the heat dissipation in the target, making it possible to use a higher than usual (typically $\sim$1.5 pnA) beam current of $\sim$5 pnA to obtain more data in a

limited time. In the case of the thin target, the compound nucleus is not stopped in the target, but continues to move, and decays during flight. The measured γ-ray energies from different detectors must therefore be corrected for the Doppler effect.

A thick target (a ^{96}Zr foil with thick Au backing, 21 mg/cm^2) was used in the second experiment. In both experiments, the γ rays emitted by the nuclei were detected using Gammasphere. Detector ID and γ-ray energies were recorded to magnetic tapes along with coincidence timing information. The information above allows for Doppler correction of the γ-rays in the off-line analysis. The coincidence information for the γ-rays was used to construct the level scheme of ^{168}Hf.

As mentioned earlier, the thin target data is good for coincidence analysis. The thick target data was mainly used for level lifetime analysis using the Doppler Shift Attenuation Method. It can also be used in the coincidence analysis for low-spin transitions, which are emitted after the recoiling nuclei completely stopped in the Au backing and form sharp peaks in the γ-ray spectra. Therefore, the thick target data may have better energy resolution than the thin-target data for low-spin transitions. It has been found that thin target data is pretty good for our analysis for decay-out transitions.

5.2 Off-line Data Analysis

This section briefly introduces the analysis process of the experimental data that leads to the ultimate goal of any γ-ray spectroscopy experiment: establishing a level scheme of the nucleus of interest. The analysis procedure starts by scanning the raw data tapes, followed by energy and efficiency calibration of the Ge detectors, and ends with building a coincidence cube or matrix.

Several software packages and scanning routines were used at each level of the analysis process. The function and use of software packages will be described in brief.

5.2.1 Data Base Construction

To perform data analysis, a database on the computer disk was constructed from the raw data on magnetic tapes by using the sorting program BDDB, developed at the Neils Bohr Institute (NBI). For each coincident event, only γ-ray multiplicity, detector IDs, and gamma energies were written into the database. The γ-ray energies detected by each detector were corrected for the Doppler shift before being written into the database.

If the source of the γ-ray photons is moving considerably compared to the speed of light, the γ-ray energies are subject to Doppler shifts when measured in the laboratory system. The measured energy of a Doppler shifted γ-ray is

$$E' = E_{\gamma,\beta} = \frac{1 + \beta \cos\theta}{\sqrt{1 - \beta^2}} E_o \tag{5.1}$$

where the θ is angle between the detector and the beam direction, β = v/c, v is the velocity of the recoiling nucleus and c the speed of light. The linear momentum (and thereby the β value) for each recoiling nucleus is a composition of the primary momentum transferred from the projectile, the momenta for the emitted particles and the momentum losses due to scattering in the target. Out of these effects, only the latter cannot be corrected for on an event-by-event basis. Momentum changes due to γ-ray emission can be neglected. The γ-ray energies were sorted into spectra corresponding to the detector rings in Gammasphere with different θ. The energy shifts of strong γ-ray lines were measured in these spectra and a β value of 4.09%

was obtained by fitting the data to Equation 5.1. The Doppler Correction of γ-ray energies corresponding to this value were then made event by event, based on the detector angle (ID).

5.2.2 Cube and Hypercube Construction

Two RADWARE programmes "incub8r" and "4play" were used to create a three-dimensional histogram (cube) and a four-dimensional histogram (hypercube) from the database for the analysis of γ-ray coincidence relationships.

When the γ-ray data are sorted into coincident histograms, γ-γ or γ-γ-γ, it includes background counts. The background counts are due to Compton-scattered γ-rays and quasicontinuum (unresolved) transitions. The procedure used in this analysis to subtract the background contribution in the gated spectra is described by Ref. [74]. This procedure consists of the following steps. (1) A one-dimensional projection of the higher dimensional histogram is obtained. (2) A background is drawn manually to the projected spectrum. (3) Software, either ESCL8R (γ-γ) or LEVIT8R (γ-γ-γ) [75], uses the prescription described in Ref. [74] with both the one-dimensional spectrum and the automatic smooth background in gated spectra [76]. The prescription is based in large part on the method of background subtraction developed by Palameta and Waddington [77] with extensions to higher fold, such as γ-γ-γ.

There are some additional background considerations to take into account depending on the reaction. For reactions in which several neutrons are evaporated, a "neutron-bump" can arise in the spectra. This bump results when inelastic neutron scattering in the Ge detectors excites the $2^+ \rightarrow 0^+$ transitions in ^{72}Ge or ^{74}Ge. In the reaction used for the present work, this bump was not visibly present in the projections of the 1D spectra and as such was neglected in the drawn background curves

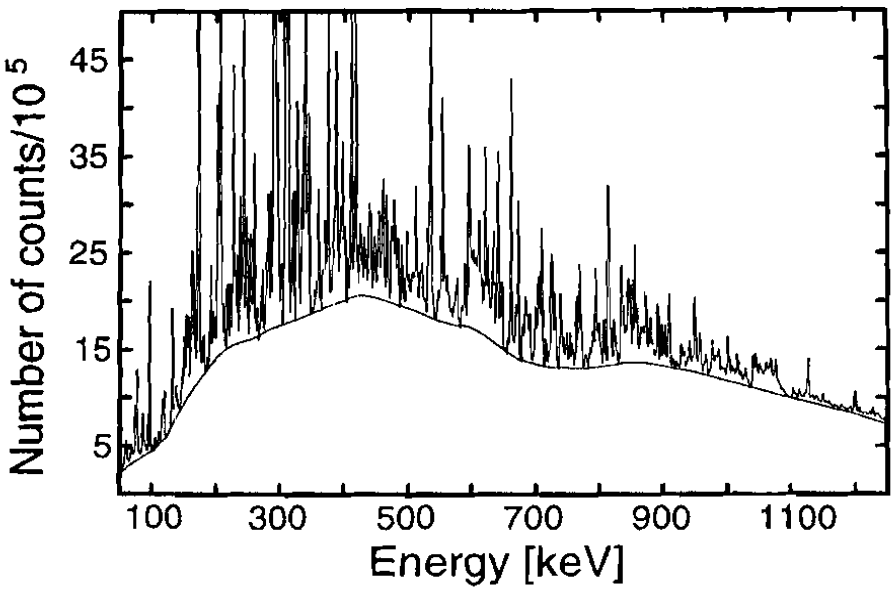

Figure 5.1: An example of background subtraction in γ-ray spectra. Taken from Ref. [76].

(see Fig. 5.1). The background should be approximately smooth and continuous for the entire spectrum. Also, a background spectrum which runs along the exact bottom of the peaks in the projection will tend to be too large. Depending on the overall statistics of the projected histogram, this maximum background should be reduced by 15 - 30% for triples (cubes). Experimentation with different background curves is often necessary to achieve the best results. The goal is to create a background spectrum, which when subtracted from the gated spectra in any dimensionality, gives a resultant spectrum that appears to have a background fluctuation around zero counts along the entire energy scale with the only significant non-zero counts in actual peaks.

5.2.3 Coincidence Analysis and Level Scheme Construction

For the analysis of prompt γ-ray cascades, the most common histograms are created by sorting γ-γ events into a two-dimensional energy spectrum (matrix). For

example, when two γ-rays γ_1 and γ_2 are detected simultaneously in a given event, then two histogram cells are incremented in the following way: (row, column) = (γ_1, γ_2). Therefore, scanning 2-fold γ-ray events using the previous procedure, results in a symmetric γ-ray matrix. An event containing three γ-rays would be resolved into three pairs ([γ_1, γ_2], [γ_1, γ_3], and [γ_2, γ_3]), and so on. If the nucleus of interest is formed in a charged-particle exit channel of a fusion evaporation reaction, then the use of charged-particle detectors to associate the emitted γ-rays with the corresponding charged-particle exit channel is essential. In this case, all γ-ray events sorted into matrices or cubes are essentially correlated with the emission of the charged-particle channel of interest. Large detector arrays, such as Gammasphere, have so many detectors that three and higher-fold Ge coincidences are common. In this case, cubes (3-D histograms) of γ-γ-γ events are typically created.

The code ESCL8R [75] was used to the analyze the γ-γ matrices from our two high-spin experiments. The code automatically keeps track of energy calibrations, efficiencies, and electron conversion coefficients. ESCL8R incorporates the background subtraction algorithm described in Ref. [75]. Once matrices are created, γ-γ coincidence relationships are studied by examining slices of these matrices. Slices, or gates, are created by summing the contents of a set of channels that represent a peak. The resulting one-dimensional histogram is then further analyzed to determine what events occurred in coincidence with the gated γ-ray. For a symmetric γ-γ matrix, a gate can be placed on either axis of the matrix at a particular energy. At the gating energy, all counts in matrix channels sharing the same coordinate (x) are projected on the other axis (y).

The width in channels for a given gate, *e.g.* γ_x, depends on the full width at half maximum (FWHM) of the peak determined by

$$FWHM(x) = \sqrt{f^2 + g^2\frac{x}{1000} + \left(h\frac{x}{1000}\right)^2} \tag{5.2}$$

where x is channel number, f is a constant due to noise in the detectors and amplifiers, g is from the statistics of the charge collection process, and h is due to Doppler-broadening of the peaks from the emitted γ rays of recoiling nuclei. Typical values for the parameters used in the above expression are approximately f = 3, g =1, and h = 4 for an energy dispersion of 0.5 keV per channel and a recoil velocity of $\sim 2.5\%$ of the speed of light.

The higher fold data (F $\geq$ 3) from large detector arrays demand a more complex analytical tool than the γ-γ matrix to fully extract all the information provided. For the Gammasphere experiment, the 2p channel data were sorted in a γ-γ-γ cube, which adds an additional axis of correlation. The code LEVIT8R [75] which is a three dimensional (3D) version of ESCL8R and thus works in a similar way, was used to inspect the cube. LEVIT8R offers the option of fitting the energies and intensities to a two dimensional projection or directly to the cube. Using an additional γ ray for gating can, in most cases, significantly enhance the resulting gated spectra. This double-gating technique on a given cube works exceptionally well at resolving coincidence relationships when one of the gating γ rays is an unresolved doublet, *i.e.* it appears in two or more bands.

An additional improvement over the cube is the hypercube as it can create four dimensional (4D) histograms. The code 4DG8R is a 4D version of LEVIT8R and is used to inspect hypercube. The 4D histograms greatly increase the peak to back-

ground ratio in bands that have (>> 4) γ-rays in coincidence. This is typical for superdeformed (SD) bands and are therefore more likely candidates for the use of 4D histograms. It is important to note that high statistics are necessary for the creation of a 4D data set: approximately 3 - 4×10^9 four-fold or higher multiplicity events. Also, these large histograms require a minimum of around 2.5 - 3 GB of hard disk space.

5.3 Experimental Results

5.3.1 Level Scheme

Figures 5.2 and 5.3 illustrate the final level scheme derived from this data. The current research work can be classified into two parts: Normal Deformed (ND) and Triaxial Strongly Deformed (TSD) structures.

The previous level scheme [1] was studied using the hypercube from the thin-target data and cubes from both thick and thin target data. As a result, the scheme has been extended at the low-spin region as well as to higher spins, and a total of seven new bands have been discovered. The Doppler-shift attenuation method was used to measure lifetimes of yrast states. The deformation extracted from this measurement has been compared with predictions from theoretical Total Routhian Surface calculations. In addition, three triaxial strongly deformed (TSD) bands previously reported by Ref. [2], have been investigated. The linking transitions to one of these bands was found. The spin and parity assignments in this work were derived from the DCO ratios and therefore should also be considered tentative for some transitions. It should be noted that the DCO measurements for the TSD bands were performed using skim tape, and another 3d cube from the skim tape was also used for γ-ray coincidence analysis. The programs "incub8r" for the cube data and "matdco" for the

DCO ratio were modified in accordance to skim data. In chapter VI and VII, we will discuss respectively ND and TSD structures in detail, and Chapter VIII summarizes the current work.

The new level scheme for ^{168}Hf deduced from this work is shown in Figures 5.2 and 5.3. In the present study, seven new bands, including three High-K bands, have been identified and many new transitions which link these bands and the known lower spin levels, have been established for both new and previously known bands. The DCO ratios have been measured for most γ-rays. The γ-ray energies, intensities and DCO ratios are listed in Table 5.1. Intensities were normalized to 100 for the 456-keV $8^+ \rightarrow 6^+$ transition in the ground state band (G).

5.3.2 Low-K Bands

5.3.2.1 Ground State Band (G)

This band was known up to $I^\pi = 22^+$ prior to this work [1] and has now been extended to 36^+. Six new linking transitions, namely 1012.0, 1323.4, 1357.3, 1385.5, 1429.3 and 1477.6 keV, feeding into the yrast band have been found. The measured DCO ratios varying from 0.90 to 1.15 confirm their stretched quadrupole nature.

5.3.2.2 Yrast (AB) Band

The band AB was previously known up to state 38^+ [1] and has been extended tentatively to 48^+. The band feeds the band G through two decay-out transitions, 551.3 and 319.8 keV. The DCO ratio of the 551.3-keV linking transition is consistent with what expected for an E2 multipolarity.

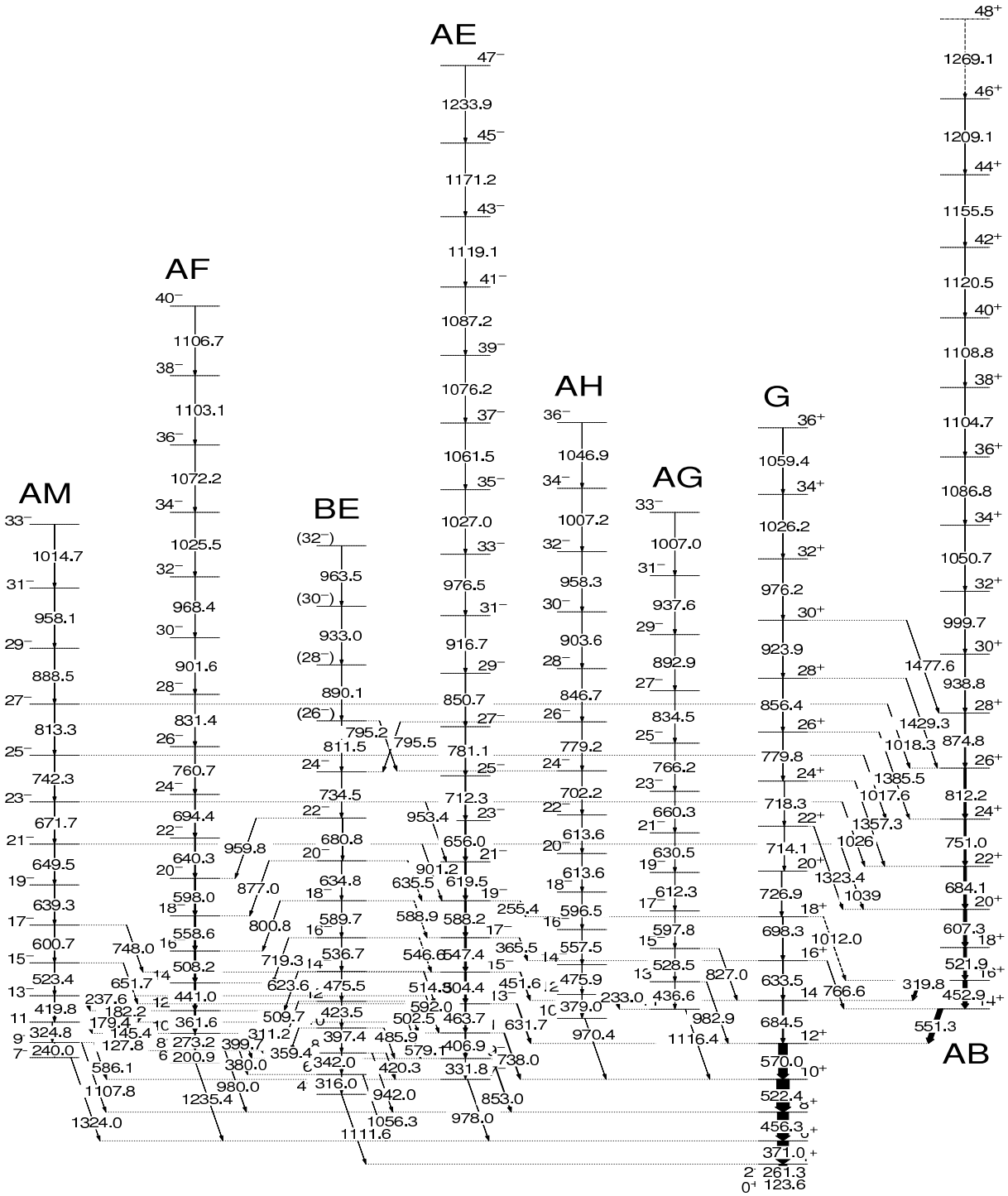

Figure 5.2: Partial level scheme of ^{168}Hf obtained from the present work. Transition energies are given in keV. Bands are labeled by their configuration using the cranking model notation (see Table 6.1).

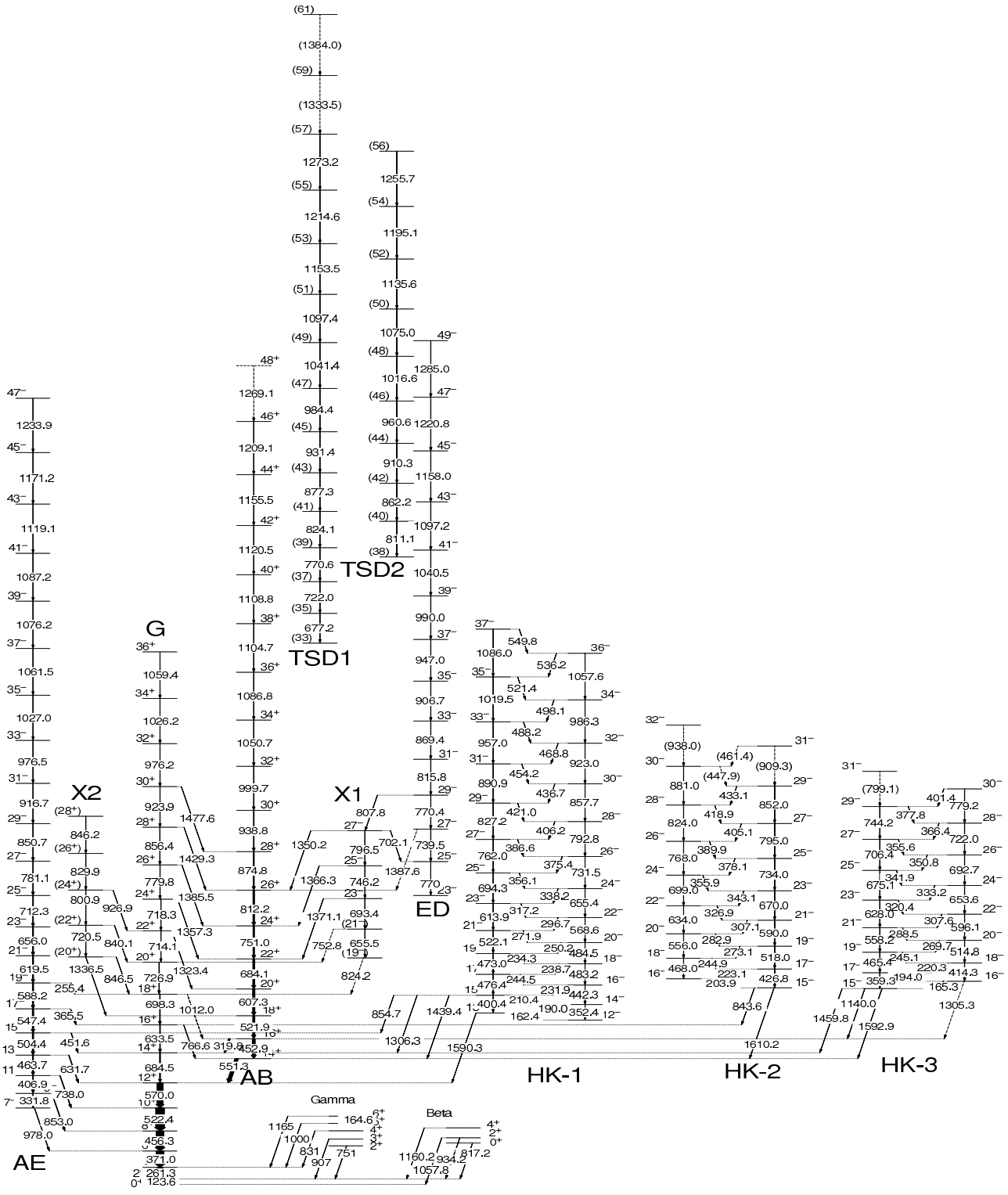

Figure 5.3: Partial level scheme of ^{168}Hf obtained from the present work.

5.3.2.3 Band AE

This negaitve-parity band has been extended from $I^{\pi} = 41^{-}$ to $I^{\pi} = 47^{-}$. Many new intra-band connections with bands BE, AF, AM and HK-1 and decay-out transitions have been observed. The stretched quadrupoles (ΔI=2) nature of all in-band transitions are confirmed and consistent with the previous study. The multipolarity of the decay-out transitions 853.0-, 738.0-, 631.7- and 365.5 keV are of E1 character.

5.3.2.4 Band AF

This band has been extended from $I^{\pi} = 38^{-}$ to $I^{\pi} = 40^{-}$. The band is fed by band BE through a number of intra-band transitions. The DCO ratios of the 1235.4-, 980.0-, 311.2-, 182.2- and 145.4-keV transitions reconfirmed the previous spin and parity assignments.

5.3.2.5 Band BE

This band has been extended from $I^{\pi} = 26^{-}$ to $I^{\pi} = 32^{-}$. The decay of this band is highly fragmented. It feeds band G as well as bands AE and AF. A number of new decay-out transitions have been found. Contrary to previous study which considers a 795 keV γ-ray as a member of this band with highest spin, we have assigned the 795.5 keV line as an intra-band transition depopulating the 26^{-} state of the AH band and interestedly, a 795.2 keV transition which connects the 26^{-} state of band BE and the 24^{-} state of band AH indicating the mixing of the two bands. Spin and parity assignments are confirmed based on the DCO ratios of the linking transitions 1111.6-, 502.5- and 485.9- keV, which are of M1 character, and are consistent with Ref. [1].

5.3.2.6 Band AG

This band is reported for the first time. Figure 5.4 shows the double gated spectra illustrating the in-band transitions. The band decays directly to band G through 1116.4-, 982.9- and 827.0 keV transitions. The spin and parity have been assigned based on the DCO ratios of 0.75(10) and 0.74(10) for 1116.4- and 982.9 keV, respectively, indicating E1 transitions to band G. The total intensity for this band accounts for only ∼1% of the total feeding to band G and thus it is a very weak band. The intensities of low spin transitions were measured along with linking transitions.

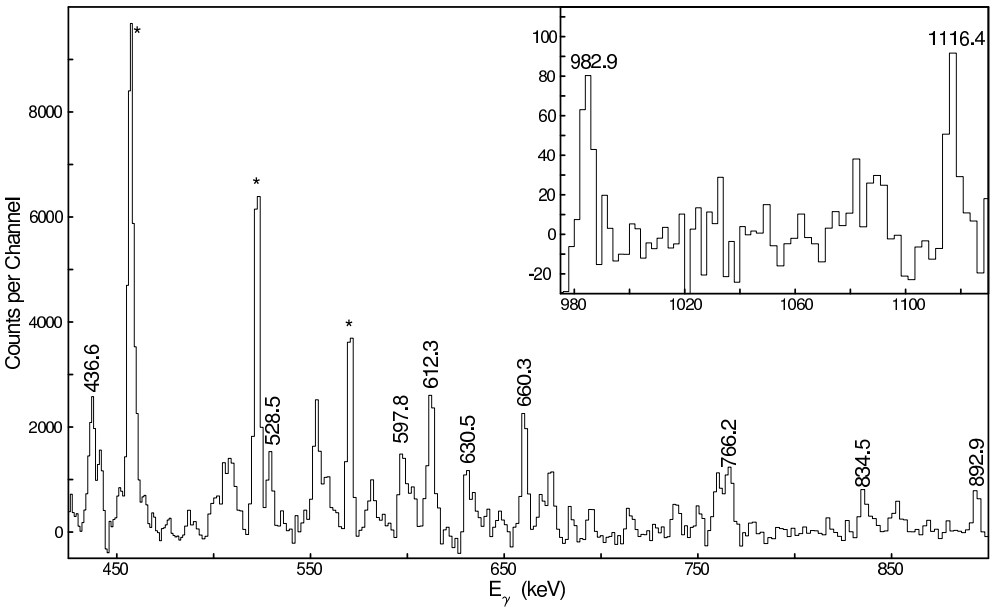

Figure 5.4: Gamma-ray coincidence spectrum of band AG, doubly gated by the band members which are labeled by γ-ray energies. The transitions marked with the stars belong to the ground state (G) band. The inset shows two decay-out transitions, 982.9- and 1116.4 keV.

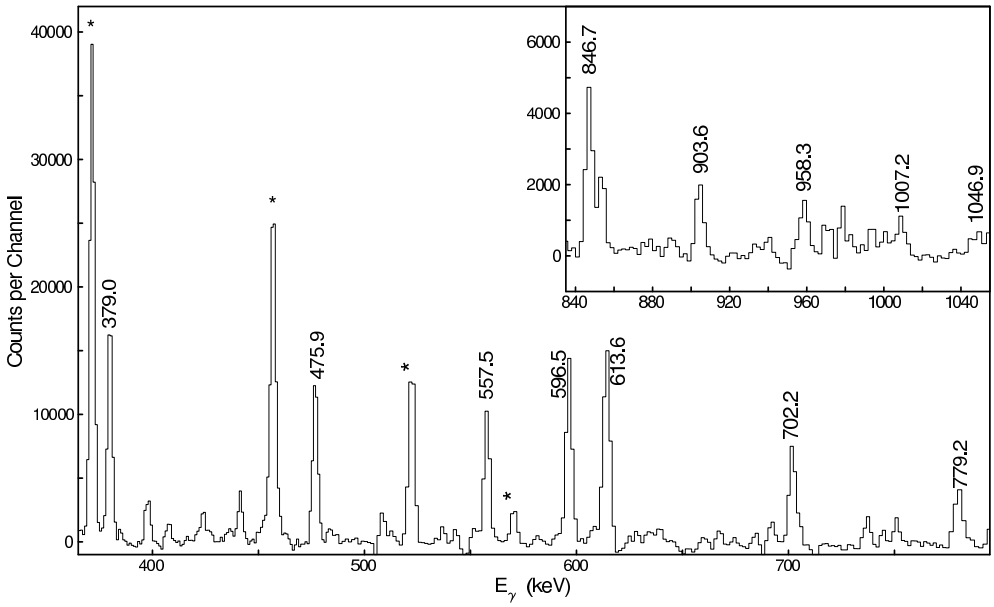

Figure 5.5: Double-gated spectrum for band AH showing the in-band transitions. The stars indicate transitions in band G.

5.3.2.7 Band AH

This band is also reported for the first time. Figure 5.5 shows the band members up to spin 36^-. This spectrum is a sum of double-gated spectra, where almost any two of the in-band transitions served as double gates. The band depopulates at the 12^- and 10^- states by 233.0 and 970.4 keV decay-out transitions, respectively. The spin and parity assignment is solely based on the DCO ratio of 0.87(13) for 970.4 keV γ-ray indicating an E1 transition to the 10^+ state in band G. The total intensity of this band accounts for only $\sim$1% of the total intensity of the band G. The intensities of 379.0 keV and 233.0 keV were measured relative to 456.3 keV in band G. Since the 475.9, 557.5 and 596.5 keV transitions are doublets with transitions in the BE and

AF bands, their intensities were estimated by comparing them with other transitions with similar energy and spin in other bands. The intensity of the 613.6 keV was not determined because of an energy doublet in the same band.

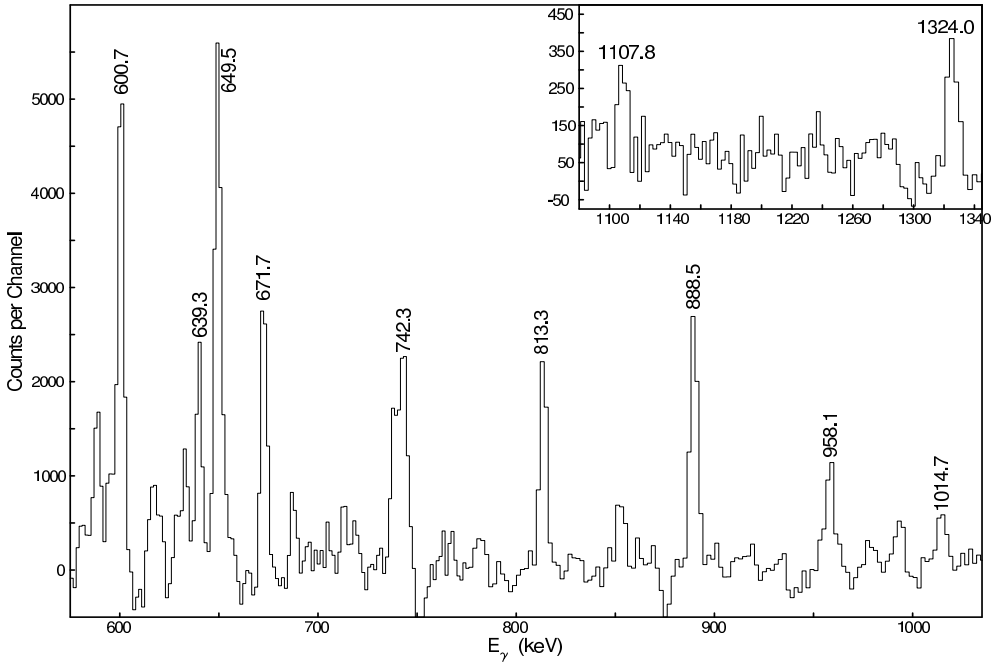

Figure 5.6: Double-gated spectrum for band AM showing in-band and decay out transitions. The inset shows higher energy decay-out transitions.

5.3.2.8 Band AM

This band has been extended significantly from $I^\pi = 11^-$ to $I^\pi = 33^-$, compromising of eleven new band members, see Fig. 5.6. Several linking transitions have been found feeding the ground state band G and yrast band AB. The DCO ratio measurements for 1324.0-, 1107.8- and 179.4 keV suggest that this is also a negative parity band.

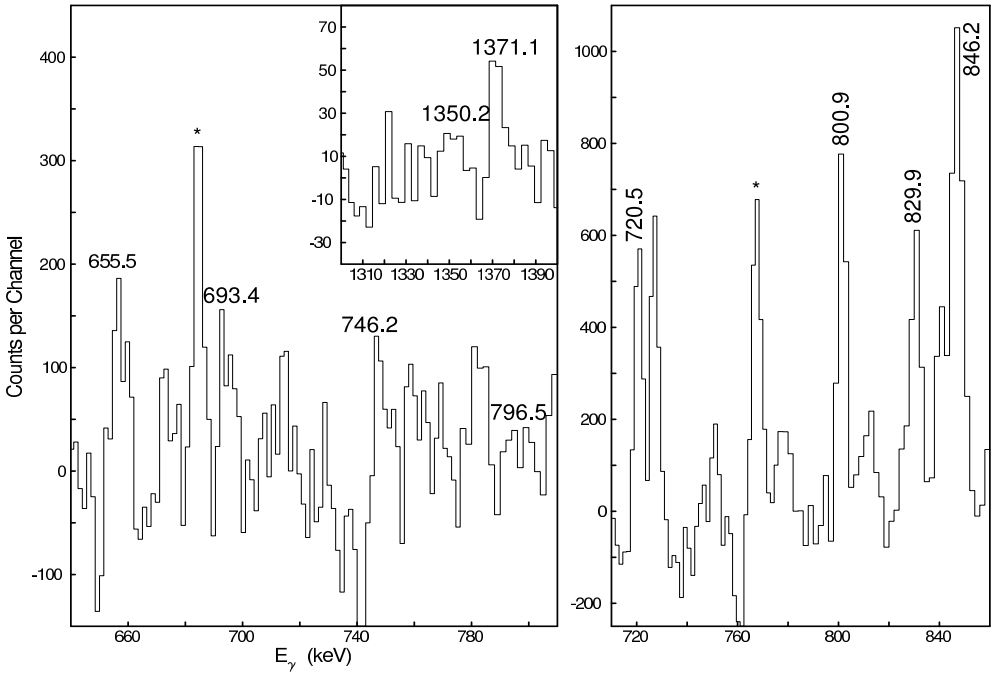

Figure 5.7: Double-gated spectra for the bands X1 (left) from a gate list containing 807.8- and 815.8 keV transitions, and X2 (right) from a gate list containing 720.5-, 800.9-, 829.9- and 846.2 keV transitions showing band members. The inset in the left figure shows decay-out transitions for X1. The transitions indicated by stars are from the band G.

5.3.2.9 Band X1

Band X1 with highly fragmented decay pathways to the AB and G bands is reported for the first time, see Fig. 5.7. The assignments of spin and parity for this band are based on a measured DCO ratios of 0.49(9) and 0.69(10) for the strongest decay-out transitions 1371.1 keV and 1366.3 keV to the 22^+ and 24^+ states of band AB, respectively, which suggests an E1 multipolarity. The three transitions from this band to other members of bands AB and G are too weak to provide reliable information for DCO ratios.

5.3.2.10 Band X2

Band X2 is also reported for the first time, see Fig. 5.7. Since the strongest decay-out transition (846.5 keV) from the bottom of the band and a band member at 846.2 keV are an energy doublet, the spin and parity are based on the measured DCO ratio of another depopulating transition 840.1 keV from the state 22^+ to the band G.

5.3.3 High-K Bands

Three high-K[1] bands are reported for the first time in ^{168}Hf, as shown in Fig. 5.3.

5.3.3.1 Band HK-1

The lowest state of the band has been assigned $I^\pi = 12^-$ based on the following arguments. Four γ-ray decay paths have been observed which link the 13^- and 15^- states into the known level scheme via 854.7-, 1306.3-, 1439.4- and 1590.3-keV transitions to states in bands G, AB and AE. The double-gated spectra presented in Fig. 5.8 illustrates some of these decay branches. The DCO ratio has been determined for the 1306.3 keV γ-ray, a transition to the 14^+ state of band G, to be of stretched dipole character. The other linking transition from the third state in this band must also be either E1 or M1 to compete with this decay. Since they go to the 14^+ state in band AB and 15^- in band AE, this limits the spin to 15. Consequently, band HK-1 has been assigned negative parity assuming that E1 is more probable than M1 nature for these high energy decay-out transitions.

[1]A high-K band has, as the name refers, a higher value of K. No or small signature splitting can be observed for these bands, and the band head may have a longer lifetime because they have very different intrinsic quasiparticle configurations from the lower-spin levels to which they decay. There is the appearance of strong intra-band M1 transitions.

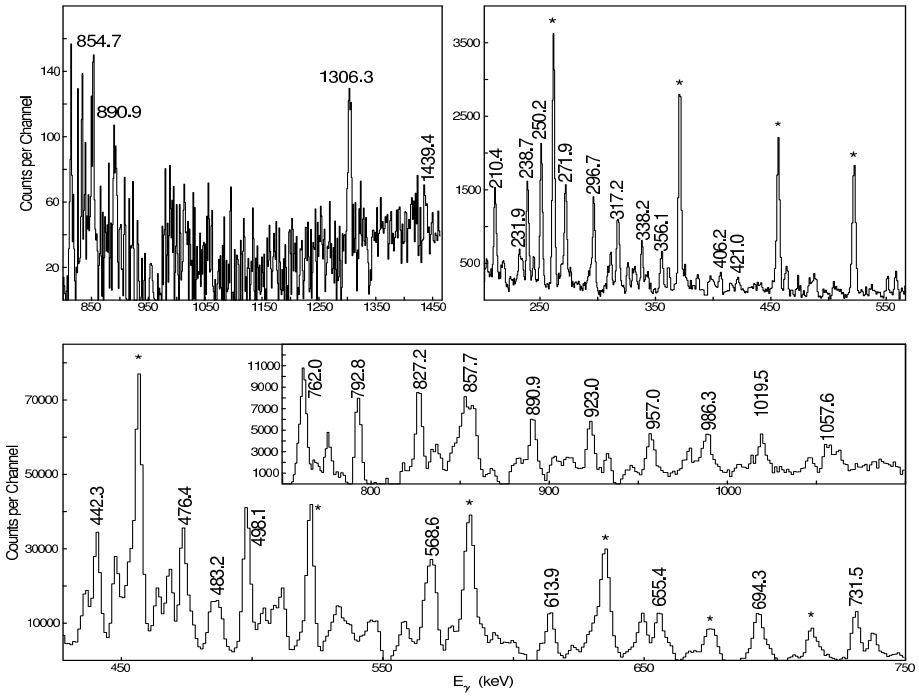

Figure 5.8: Double-gated spectra from a gate list consisting of M1 transitions for the band HK-1. Top: the left side illustrates decay-out transitions while the figure at right shows lower energy transitions. Bottom: shows the band members where higher energy transitions can be seen in the inset. The transitions marked with stars belong to the band G.

5.3.3.2 Band HK-2

The lowest state of the band has been assigned $I^{\pi} = 15^{-}$ based on the following arguments. This state decays to the known level scheme via 843.6- and 1610.2 keV transitions to the 16^{+} member of band G and the 14^{+} member of band AB, respectively. One expects either an E1 or M1 transition to depopulate the band head since there is a high probability of a lower lying state with a spin difference of 1 thus ruling out an E2 transition. This limits the spin to 15. The double-gated spectra presented in Fig. 5.9 illustrates some of these decay branches. The spin/parity is based on

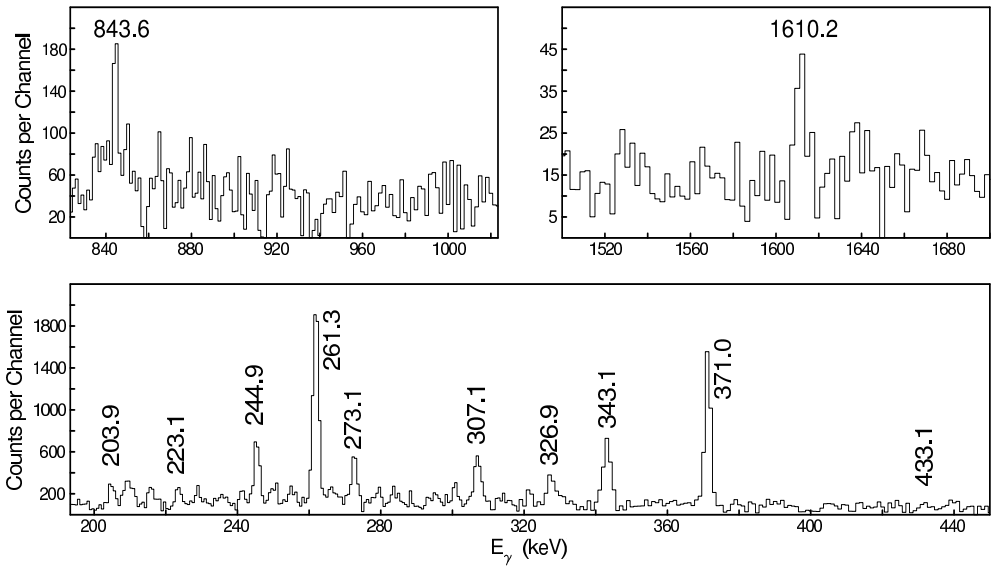

Figure 5.9: Double-gated spectra for the band HK-2 showing decay-out (top) and lower in-band transitions (bottom). The strong transitions 261.3- and 371.0 keV are from band G.

the DCO ratios of 0.93(15) and 1.08(12) for the 1610.2- and 843.6-keV decay-out transitions, respectively which are consistent with E1 transitions.

5.3.3.3 Band HK-3

The lowest state of the band has been assigned $K^\pi = 15^-$ based on the following arguments. It decays to the known level scheme via a 1459.8-keV transition from the band head to the 14^+ state in band G and 1140.0-, 1305.3-, and 1592.9-keV transitions from the first two band states to the 14^+ and 16^+ members of the band AB. The double-gated spectra presented in Fig. 5.10 illustrates some of these decay branches. Since E1 or M1 transitions are expected to dominate, this limits the spin

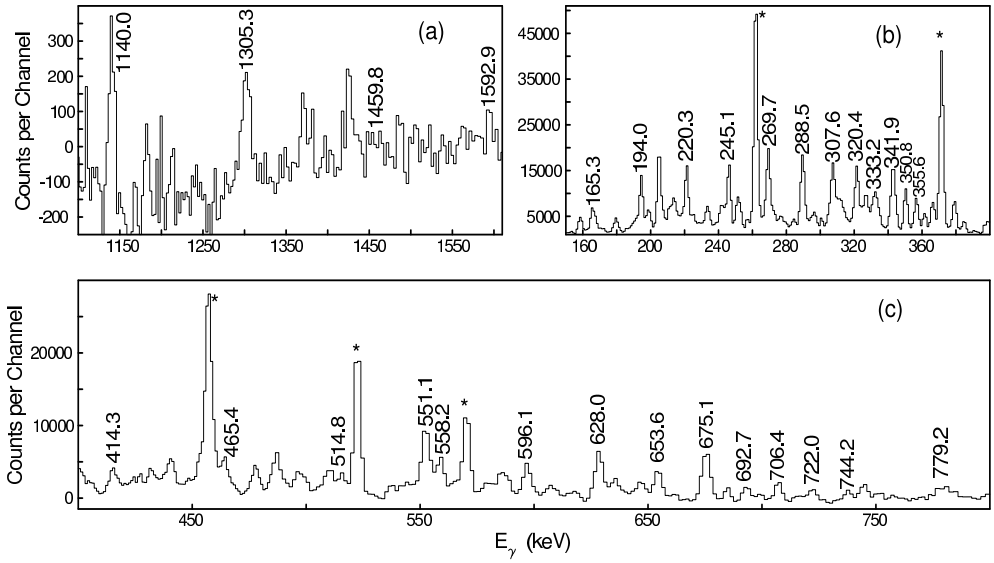

Figure 5.10: Double-gated spectra for the band HK-3. Top: the left side illustrates decay-out transitions while the figure at right shows very lower energy transitions. Bottom: it shows both the lower and higher energy transitions of the band. The transitions marked with stars belong to the band G.

to 15. The assignment of negative parity is based on the DCO ratio 0.98(14) for the 1140.0 keV transition from the band head to the 16^+ state in band AB and assumption that E1 is more probable than M1 nature for high energies.

Table 5.1: γ-ray energies, intensities and DCO ratios in ^{168}Hf.

I_i^π	E_i(keV)	E_γ(keV)[a]	I_γ[b]	R_{DCO}	Assignment
0^+	Band G: 0.0				
2^+	123.9	123.6	23(2)		E2
4^+	385.6	261.3	79(3)	1.09(10)	E2
6^+	756.8	371.0	86(3)	1.40(15)[c]	E2
8^+	1213.3	456.3	100(3)	1.42(16)[c]	E2
10^+	1735.6	522.4			E2
12^+	2305.7	570.0	70(3)	1.09(11)	E2
14^+	2990.1	684.5			E2
16^+	3623.6	766.6			E2
		633.5			E2
18^+	4321.9	1012.0			E2
		698.3	4.4(7)		E2
20^+	5048.8	726.9			E2
22^+	5762.9	1323.4			E2
		714.1			E2
24^+	6481.0	1357.3		1.02(17)	E2
		718.3	3.18		
26^+	7260.5	1385.5		0.94(12)	E2
		779.8			E2

Table 5.1 (Continued.)

I_i^π	E_i(keV)	E_γ(keV)[a]	I_γ[b]	R_{DCO}	Assignment
28^+	8116.8	1429.3			E2
		856.4			E2
30^+	9040.5	1477.6			E2
		923.9			E2
32^+	10016.7	976.2			E2
34^+	11042.9	1026.2			E2
36^+	12102.3	1059.4			E2
	Band AB:				
14^+	2857.0	551.3	45(2)	0.98(10)	E2
16^+	3309.9	452.9			E2
		319.8			E2
18^+	3832.0	521.9			E2
20^+	4439.5	607.3	19(2)	0.95(9)	E2
22^+	5123.8	684.1			E2
24^+	5875.0	751.0	15(1)		E2
26^+	6687.5	812.2			E2
28^+	7562.6	874.8			E2
30^+	8501.4	938.8			E2
32^+	9501.1	999.7			E2
34^+	10551.8	1050.7			E2
36^+	11638.6	1086.8			E2

Table 5.1 (Continued.)

I_i^π	E_i(keV)	E_γ(keV)[a]	I_γ[b]	R_{DCO}	Assignment
38^+	12743.3	1104.7			E2
40^+	13852.1	1108.8			E2
42^+	14972.6	1120.5			E2
44^+	16128.1	1155.5			E2
46^+	17337.2	1209.1			E2
48^+	18606.3	1269.1			E2
	Band AE:				
7^-	1734.9	978.0			E1
9^-	2066.6	853.0	6.2(7)	0.80(8)	E1
		331.8	0.72(6)	0.97(12)	E2
11^-	2473.6	738.0	8.4(8)	0.64(14)	E1
		406.9	3.6(4)	0.97(14)	E2
13^-	2937.3	631.7	9.8(9)	0.62(9)	E1
		463.7	13.5(9)	0.98(10)	E2
15^-	3441.7	504.4	16(1)	0.97(10)	E2
		451.6			E1
17^-	3989.1	547.4		1.03(10)	E2
		365.5		0.55(8)	E1
19^-	4577.3	588.2		0.99(5)	E2
		255.4			E1
21^-	5196.8	619.5		1.02(10)	E2

Table 5.1 (Continued.)

I_i^π	E_i(keV)	E_γ(keV)[a]	I_γ[b]	R_{DCO}	Assignment
23^-	5852.8	656.0		1.02(9)	E2
25^-	6565.1	712.3		1.03(9)	E2
27^-	7346.2	781.1		1.02(9)	E2
29^-	8196.9	850.7		0.93(8)	E2
31^-	9113.6	916.7		0.99(9)	E2
33^-	10090.1	976.5		0.99(9)	E2
35^-	11117.1	1027.0		1.06(7)	E2
37^-	12178.6	1061.5		1.09(10)	E2
39^-	13254.8	1076.2		0.96(12)	E2
41^-	14342.0	1087.2			E2
43^-	15461.1	1119.1		1.04(12)	E2
45^-	16632.3	1171.2		1.03(9)	E2
47^-	17866.2	1233.9			E2
	Band AF:				
6^-	1992.3	1235.4		0.85(11)	E1
8^-	2193.2	980.0	3.3(4)	0.84(10)	E1
		380.0	3.0(6)	0.91(12)	E2
		200.9	0.88(13)		E2
10^-	2466.4	399.7	0.53(14)		M1/E2
		311.2	2.0(2)	0.87(7)	E2
		273.2	5.9(6)	0.91(8)	E2

Table 5.1 (Continued.)

I_i^π	E_i(keV)	E_γ(keV)[a]	I_γ[b]	R_{DCO}	Assignment
		145.4	0.72(12)	0.41(7)	M1
12^-	2828.0	361.6	9.2(8)	0.93(9)	E2
		182.2	<0.5	0.59(8)	M1
14^-	3269.0	441.0	9.2(9)	0.98(8)	E2
16^-	3777.2	508.2		0.98(7)	E2
18^-	4335.8	558.6		1.08(7)	E2
20^-	4933.8	598.0	9.4(9)	1.05(8)	E2
22^-	5574.1	640.3		1.02(9)	E2
24^-	6268.6	694.4		1.03(9)	E2
26^-	7029.3	760.7		1.02(9)	E2
28^-	7860.7	831.4		1.02(10)	E2
30^-	8762.3	901.6		1.03(8)	E2
32^-	9730.7	968.4		1.02(10)	E2
34^-	10756.3	1025.5		1.14(14)	E2
36^-	11828.5	1072.2		0.96(12)	E2
38^-	12931.6	1103.1		1.02(10)	E2
40^-	14038.3	1106.7		0.99(12)	E2
	Band BE:				
4^-	1497.2	1111.6		0.88(12)	E1
6^-	1813.2	1056.3	2.2(3)	0.89(15)	E1
		316.0	0.5(2)		E2

Table 5.1 (Continued.)

I_i^π	E_i(keV)	E_γ(keV)[a]	I_γ[b]	R_{DCO}	Assignment
8^-	2155.2	942.0	1.0(1)	1.06(11)	E1
		420.3	1.5(2)		M1
		342.0	4.0(5)		E2
10^-	2552.6	485.9	0.6(2)	0.72(9)	M1
		397.4	2.5(3)	1.05(9)	E2
		359.4	1.01(8)		E2
12^-	2976.1	509.7			E2
		502.5	0.9(3)	0.73(10)	M1
		423.5	1.9(3)	0.98(11)	E2
14^-	3451.6	623.6			E2
		514.3			M1
		475.5	2.5(3)	1.06(9)	E2
16^-	3988.3	719.3			E2
		546.6			M1
		536.7		1.05(8)	E2
18^-	4578.0	800.8			E2
		589.7		1.04(10)	E2
		588.9			M1
20^-	5212.8	877.0		1.06(8)	E2
		635.5			M1
		634.8		0.99(11)	E2
22^-	5893.6	959.8			E2

Table 5.1 (Continued.)

I_i^π	E_i(keV)	E_γ(keV)[a]	I_γ[b]	R_{DCO}	Assignment
		680.8		1.03(10)	E2
24^-	6628.1	734.5		1.03(10)	E2
26^-	7439.6	811.5		1.02(10)	E2
		795.2		1.09(12)	E2
28^-	8329.7	890.1		0.94(9)	E2
30^-	9262.7	933.0		0.99(11)	E2
32^-	10226.2	963.5			E2
	Band AG:				
11^-	2852.0	1116.4	0.65(15)	0.75(10)	E1
13^-	3288.6	982.9	<0.5	0.74(10)	E1
		436.6	0.8(2)	0.92(14)	E2
15^-	3817.1	827.0	<0.5		
		528.5	1.5(2)	1.19(13)	E2
17^-	4414.9	597.8	0.5(1)	0.93(12)	E2
19^-	5027.2	612.3	1.3(3)	0.89(14)	E2
21^-	5657.7	630.5	0.9(2)	0.98(13)	E2
23^-	6318.0	660.3	1.3(3)	1.03(10)	E2
25^-	7084.2	766.2		1.05(13)	E2
27^-	7918.7	834.5			E2
29^-	8811.6	892.9		1.15(15)	E2
31^-	9749.2	937.6			E2

Table 5.1 (Continued.)

I_i^π	E_i(keV)	E_γ(keV)[a]	I_γ[b]	R_{DCO}	Assignment
33^-	10756.2	1007.0		1.11(16)	E2
	Band AH:				
10^-	2706.0	970.4		0.87(13)	E1
12^-	3085.0	379.0	0.9(2)	0.97(15)	E2
		233.0	<0.5	0.61(8)	M1
14^-	3560.9	475.9	0.87	0.98(11)	E2
16^-	4118.5	557.5	0.71	1.03(9)	E2
18^-	4715.0	596.5	1.0(2)	0.91(8)	E2
20^-	5328.6	613.6		1.04(13)	E2
22^-	5942.2	613.6			E2
24^-	6644.4	702.2		1.05(10)	E2
26^-	7423.6	795.5			E2
		779.2		0.94(13)	E2
28^-	8270.3	846.7		1.02(16)	E2
30^-	9173.9	903.6		0.89(13)	E2
32^-	10132.2	958.3		0.90(8)	M1/E2
34^-	11139.4	1007.2		0.89(11)	M1/E2
36^-	12186.3	1046.9			E2
	Band AM:				
7^-	2080.9	1324.0	0.9(2)	0.72(9)	E1
9^-	2321.0	1107.8	1.7(3)	0.65(8)	E1

Table 5.1 (Continued.)

I_i^π	E_i(keV)	E_γ(keV)[a]	I_γ[b]	R_{DCO}	Assignment
		586.1			E2
		240.0	1.0(2)		E2
		127.8			M1/E2
11^-	2645.8	579.1			E2
		324.8	1.5(2)	1.02(12)	E2
		179.4	<0.5		M1
13^-	3065.6	592.0			E2
		419.8	0.80(15)	0.93(11)	E2
		237.6			M1
15^-	3589.0	651.7			E2
		523.4			E2
17^-	4189.7	748.0			E2
		600.7		0.93(12)	E2
19^-	4829.0	639.3		1.09(11)	E2
21^-	5478.5	1039.0			E1
		901.2		1.04(13)	E2
		649.5		1.10(12)	E2
23^-	6150.2	1026.3			E1
		953.4		0.91(9)	E2
		671.7		0.93(10)	E2
25^-	6892.5	1017.6		1.06(10)	E1

Table 5.1 (Continued.)

I_i^π	E_i(keV)	E_γ(keV)[a]	I_γ[b]	R_{DCO}	Assignment
		742.3		1.06(8)	E2
27^-	7705.8	1018.3		0.89(10)	E1
		813.3		0.90(13)	E2
29^-	8594.3	888.5			E2
31^-	9552.4	958.1		0.91(11)	E2
33^-	10567.1	1014.7		0.94(11)	E2
	Band X1:				
19^-	5146.1	824.2			E1
21^-	5801.6	752.8			E1
		655.5			E2
23^-	6495.0	1371.1	<0.5	0.49(9)	E1
		693.4	<0.5		E2
25^-	7241.2	1366.3	<0.5	0.69(10)	E1
		746.2	<0.5		E2
27^-	8037.7	1350.2	<0.5		E1
		796.5	<0.5		E2
		702.1			E2
	Band X2:				
20^+	5168.4	1336.5			E2
		846.5		0.91(13)	E2
22^+	5888.9	840.1		0.93(13)	E2

Table 5.1 (Continued.)

I_i^π	E_i(keV)	E_γ(keV)[a]	I_γ[b]	R_{DCO}	Assignment
		720.5		1.10(12)	E2
24^+	6689.8	926.9		1.02(12)	E2
		800.9		1.15(12)	E2
26^+	7519.7	829.9			E2
	Band HK-1:				
13^-	3896.0	1590.3			E1
		162.4			M1
14^-	4086.0	352.4			E2
		190.0			M1
15^-	4296.4	1439.4			E1
		1306.3	<0.5	0.90(10)[c]	E1
		854.7			M1
		400.4			E2
		210.4	0.70(15)	0.96(11)[c]	M1
16^-	4528.3	442.3		1.39(16)[c]	E2
		231.9	1.0(2)	0.78(10)	M1
17^-	4772.8	476.4		1.49(15)[c]	E2
		244.5		0.76(10)	M1
18^-	5011.5	483.2		1.61(18)[c]	E2
		238.7		0.93(10)[c]	M1
19^-	5245.8	473.0		1.27(15)[c]	E2

Table 5.1 (Continued.)

I_i^π	E_i(keV)	E_γ(keV)[a]	I_γ[b]	R_{DCO}	Assignment
		234.3		0.65(9)	M1
20^-	5496.0	484.5			E2
		250.2	1.9(3)	0.74(8)	M1
21^-	5767.9	522.1		1.45(16)[c]	E2
		271.9	1.8(3)	0.70(8)	M1
22^-	6064.6	568.6			E2
		296.7	2.1(2)	0.75(10)	M1
23^-	6381.9	613.9		0.98(14)	E2
		317.2	1.5(2)	0.63(8)	M1
24^-	6720.0	655.4		1.37(15)[c]	E2
		338.2	1.1(3)	0.71(8)	M1
25^-	7076.1	694.3		1.05(11)	E2
		356.1		0.95(8)[c]	M1
26^-	7451.5	731.5		1.39(16)[c]	E2
		375.4		0.97(9)[c]	M1
27^-	7838.1	762.0		1.10(11)	E2
		386.6	1.7(2)	0.97(10)[c]	M1
28^-	8244.3	792.8		1.78(25)[c]	E2
		406.2	1.3(2)		M1
29^-	8665.3	827.2	1.2(3)		E2
		421.0	1.6(3)		M1
30^-	9102.0	857.7			E2

Table 5.1 (Continued.)

I_i^π	E_i(keV)	E_γ(keV)[a]	I_γ[b]	R_{DCO}	Assignment
		436.7			M1
31^-	9556.2	890.9		0.90(11)	M1/E2
		454.2			M1
32^-	10025.0	923.0			E2
		468.8	1.3(2)		M1
33^-	10513.2	957.0			E2
		488.2			M1
34^-	11011.3	986.3			E2
		498.1			M1
35^-	11532.7	1019.5			E2
		521.4			M1
36^-	12068.9	1057.6			E2
		536.2			M1
37^-	12618.7	1086.0			E2
		549.8			M1
	Band HK-2:				
15^-	4467.3	1610.2	1.0(2)	0.93(15)[c]	E1
		843.6	<0.5	1.08(12)[c]	E1
16^-	4671.1	203.9	<0.5	0.82(10)	M1/E2
17^-	4894.1	426.8			E2
		223.1	0.8(1)	0.70(8)	M1
18^-	5139.1	468.0			E2

Table 5.1 (Continued.)

I_i^π	E_i(keV)	E_γ(keV)[a]	I_γ[b]	R_{DCO}	Assignment
		244.9		0.78(10)	M1
19^-	5412.2	518.0			E2
		273.1		1.03(12)[c]	M1
20^-	5695.1	556.0			E2
		282.9		1.17(13)[c]	M1/E2
21^-	6002.2	590.0	0.95(11)		E2
		307.1	0.84(7)	0.63(7)	M1
22^-	6329.1	634.0		0.96(8)	E2
		326.9		0.61(8)	M1
23^-	6672.2	670.0		1.02(15)	E2
		343.1		0.77(9)	M1
24^-	7028.1	699.0		1.08(11)	E2
		355.9		0.94(11)[c]	M1
25^-	7406.2	734.0		1.33(22)[c]	E2
		378.1		1.02(11)[c]	M1
26^-	7796.1	768.0		1.11(16)	E2
		389.9		0.72(9)	M1
27^-	8201.2	795.0		0.92(11)	E2
		405.1			M1
28^-	8620.1	824.0		1.33(20)[c]	E2
		418.9			M1
29^-	9053.2	852.0			E2

Table 5.1 (Continued.)

I_i^π	E_i(keV)	E_γ(keV)[a]	I_γ[b]	R_{DCO}	Assignment
		433.1			M1
30^-	9501.1	881.0			E2
		447.9			M1
31^-	9962.5	909.3			E2
		461.4			M1
32^-	10439.1	938.0			E2
	Band HK-3:				
15^-	4449.9	1592.9			E1
		1459.8			E1
		1140.0	<0.5	0.98(14)[c]	E1
16^-	4615.2	1305.3	<0.5		E1
		165.3	<0.5	0.78(16)	M1
17^-	4809.2	359.3			E2
		194.0	<0.5	0.65(7)	M1
18^-	5029.5	414.3		1.32(13)[c]	E2
		220.3	<0.5	1.03(12)[c]	M1
19^-	5274.6	465.4			E2
		245.1		0.81(10)	M1/E2
20^-	5544.3	514.8			E2
		269.7		0.68(8)	M1
21^-	5832.8	558.2		1.67(20)[c]	E2

Table 5.1 (Continued.)

I_i^π	E_i(keV)	E_γ(keV)[a]	I_γ[b]	R_{DCO}	Assignment
		288.5		0.58(9)	M1
22^-	6140.4	596.1		0.96(13)	E2
		307.6		0.69(10)	M1
23^-	6460.8	628.0		1.02(11)	E2
		320.4		0.62(5)	M1
24^-	6794.0	653.6		1.02(13)	E2
		333.2		1.02(10)[c]	M1
25^-	7135.9	675.1		0.93(10)	E2
		341.9		0.69(7)	M1
26^-	7486.7	692.7			E2
		350.8		1.11(15)[c]	M1
27^-	7842.3	706.4		1.07(12)	E2
		355.6			M1
28^-	8208.7	722.0			E2
		366.4			M1
29^-	8586.5	744.2			E2
		377.8			M1
30^-	8987.9	779.2			E2
		401.4			M1
31^-	9385.6	799.1			E2
	Band ED:				

Table 5.1 (Continued.)

I_i^π	E_i(keV)	E_γ(keV)[a]	I_γ[b]	R_{DCO}	Assignment
25^-	7335.6	770.0			E2
27^-	8075.1	1387.6			E1
		739.5		0.93(14)	E2
29^-	8845.5	807.8	<0.5	0.91(11)	E2
		770.4	<0.5	1.10(16)	E2
31^-	9661.3	815.8		0.95(14)	E2
33^-	10530.7	869.4		1.02(7)	E2
35^-	11437.4	906.7		0.93(10)	E2
37^-	12384.4	947.0		1.06(11)	E2
39^-	13374.4	990.0		1.05(12)	E2
41^-	14414.9	1040.5		0.98(14)	E2
43^-	15512.1	1097.2		0.95(13)	E2
45^-	16670.1	1158.0			E2
47^-	17890.9	1220.8			E2
49^-	19175.9	1285.0			E2
	Band TSD1:				
(35)	12977.4	677.2		0.95(11)	E2
(37)	13699.5	722.0		1.09(12)	E2
(39)	14470.3	770.6		0.91(12)	E2
(41)	15294.5	824.1		0.89(11)	E2
(43)	16172.0	877.3		0.98(7)	E2

Table 5.1 (Continued.)

I_i^π	E_i(keV)	E_γ(keV)[a]	I_γ[b]	R_{DCO}	Assignment
(45)	17103.6	931.4		0.89(10)	E2
(47)	18088.2	984.4		1.02(10)	E2
(49)	19129.8	1041.4			E2
(51)	20227.5	1097.4			E2
(53)	21381.0	1153.5		1.05(15)	E2
(55)	22596.2	1214.6			E2
(57)	23869.4	1273.2			E2
(59)	25202.9	1333.5			E2
(61)	26586.9	1384.0			E2
	Band TSD2:				
	15070.0	811.1		0.89(11)	E2
	15932.2	862.2		0.93(12)	E2
	16842.5	910.3			E2
	17803.1	960.6		1.05(13)	E2
	18819.7	1016.6			E2
	19894.6	1075.0			E2
	21030.2	1135.6			E2
	22225.3	1195.1			E2
	23480.9	1255.7			E2

[a] Accuracy of γ-ray energies is $\sim$0.3 keV except for the weakest transitions where the uncertainties are larger.
[b] Intensities are mostly obtained from gated spectra and normalized to the 456.3 keV transition in band G, which has an intensity 100.
[c] DCO ratios obtained by gating on $\Delta I = 1$ transitions. All other DCO ratios are obtained by gating on stretched E2 transitions.

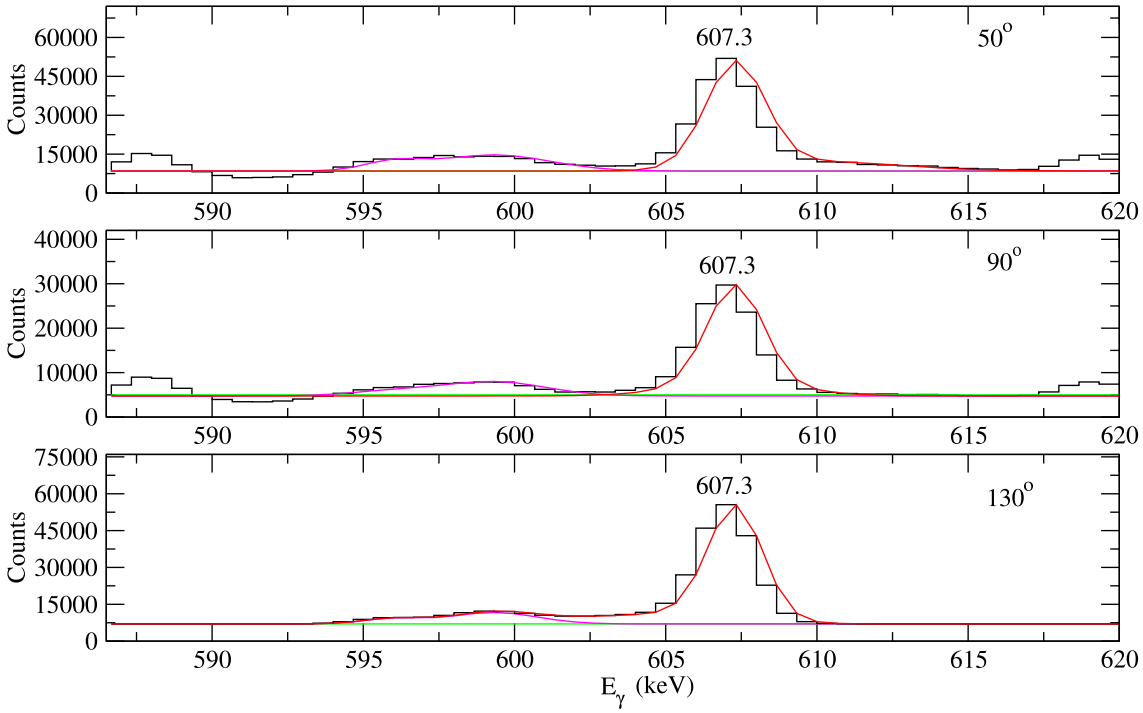

Figure 5.11: Line shapes of the E_γ = 607.3 keV transition in the band AB. Experimental data are shown as histogram, fitted shapes as red lines and the green lines show the fitted backgrounds with contaminants.

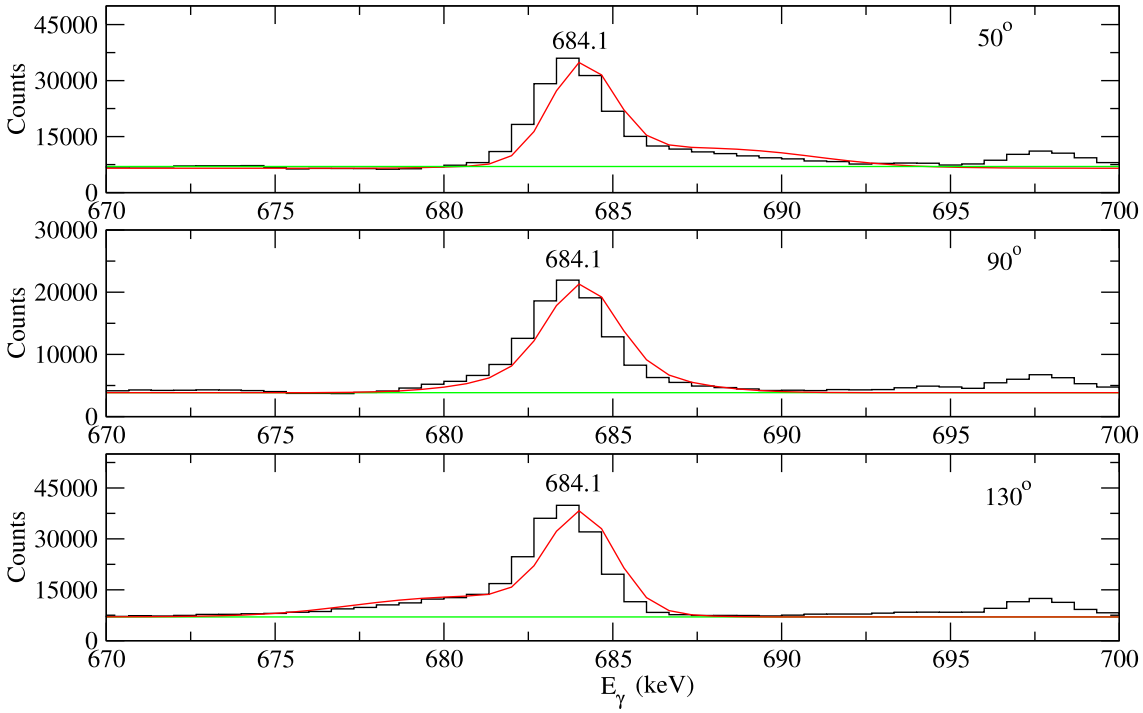

Figure 5.12: Line shapes of the E_γ = 684.1 keV transition in the band AB. Experimental data are shown as histogram, fitted shapes as red lines and the green lines show the fitted backgrounds with contaminants.

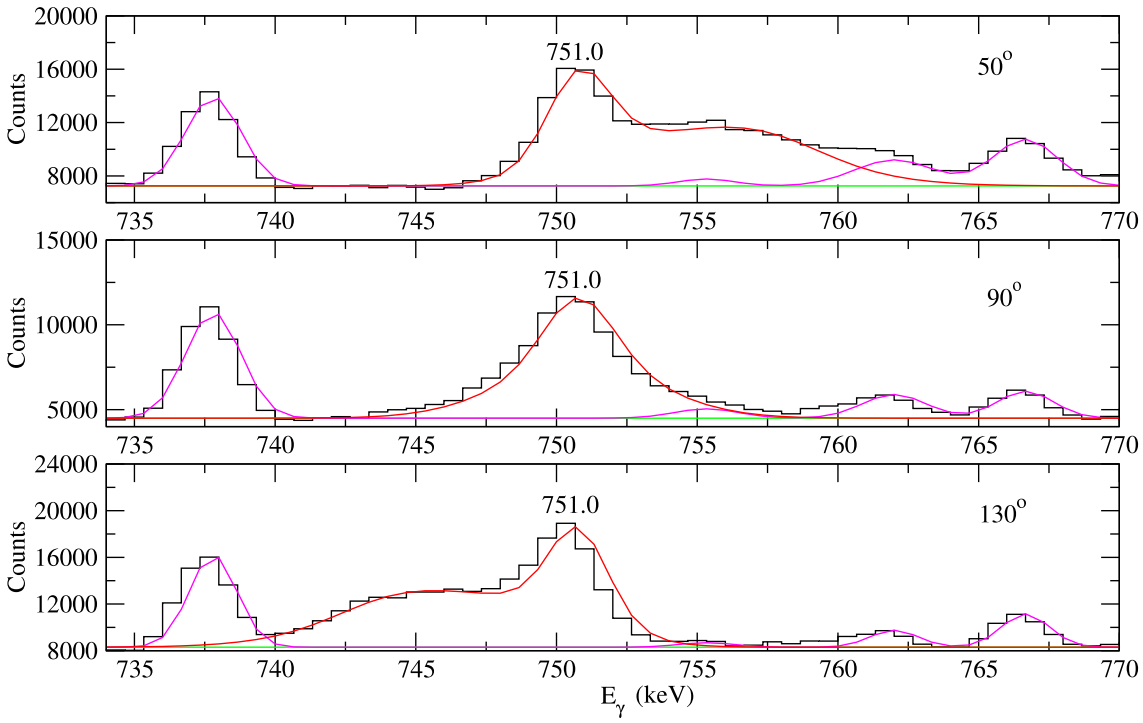

Figure 5.13: Line shapes of the E_γ = 751.0 keV transition in the band AB. Experimental data are shown as histogram, fitted shapes as red lines and the green lines show the fitted backgrounds with contaminants.

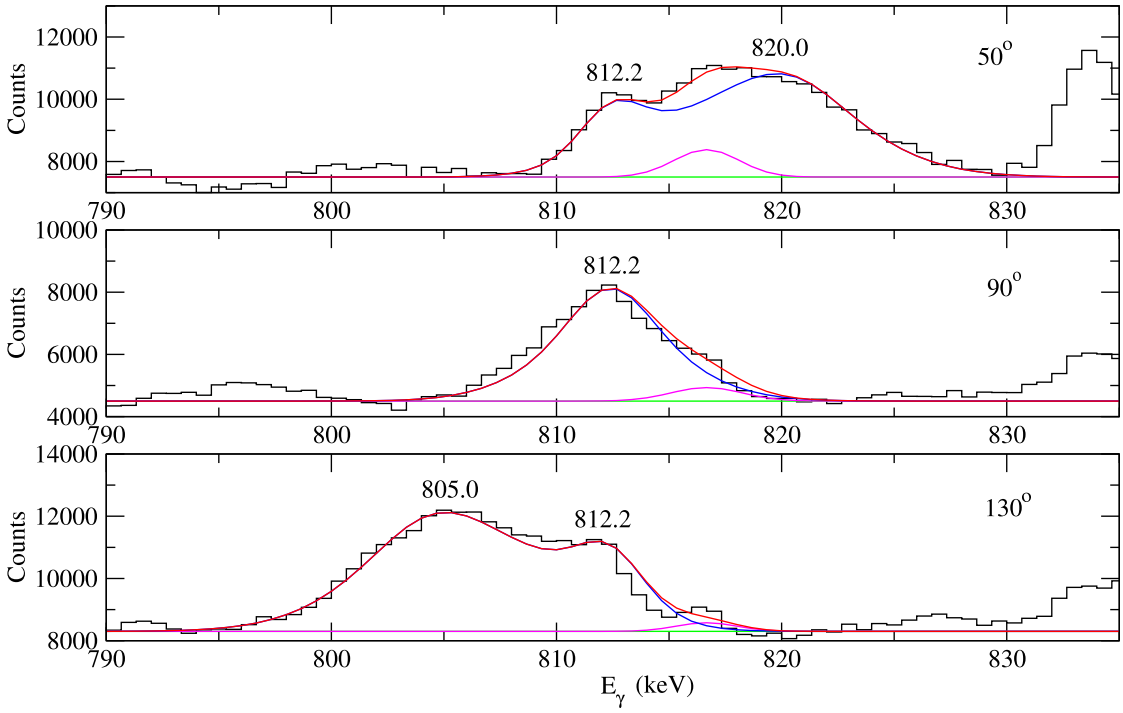

Figure 5.14: Line shapes of the E_γ = 812.2 keV transition in the band AB. Experimental data are shown as histogram, fitted shapes as red lines and the green lines show the fitted backgrounds with contaminants.

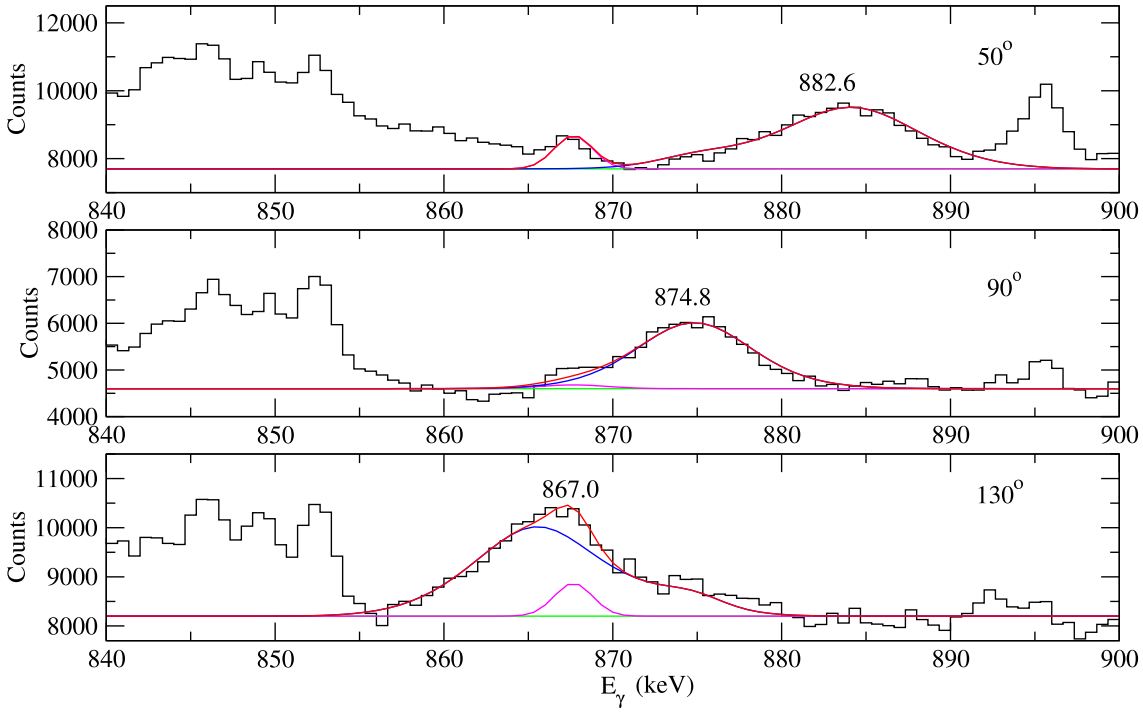

Figure 5.15: Line shapes of the E_γ = 874.8 keV transition in the band AB. Experimental data are shown as histogram, fitted shapes as red lines and the green lines show the fitted backgrounds with contaminants.

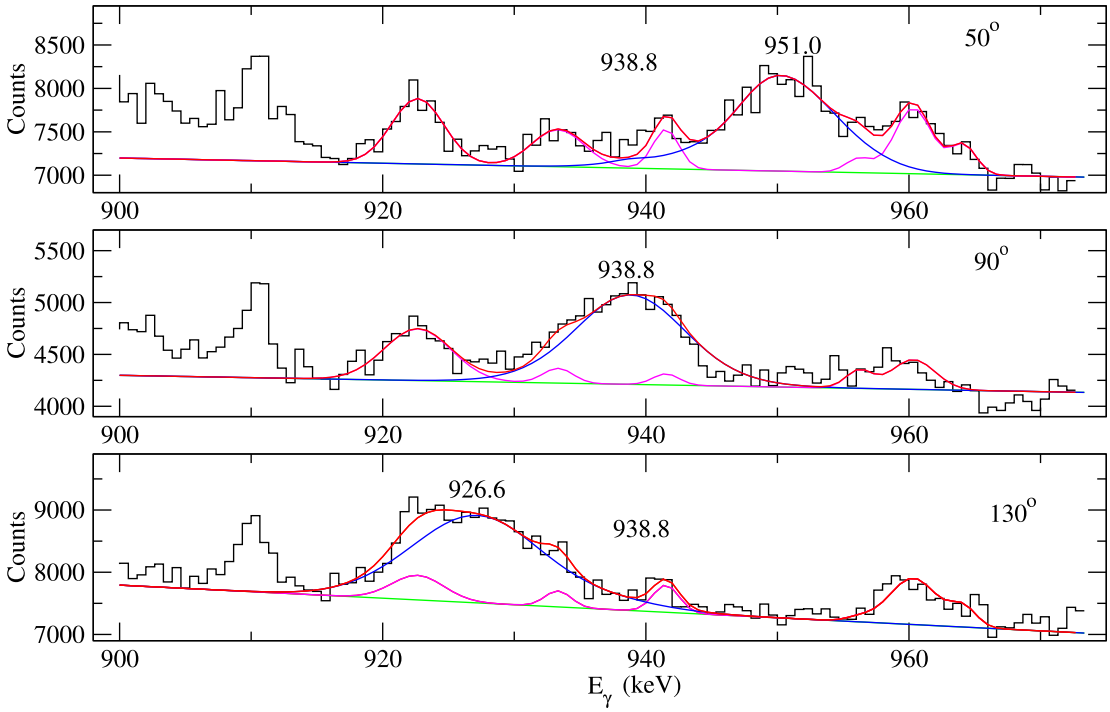

Figure 5.16: Line shapes of the E_γ = 938.8 keV transition in the band AB. Experimental data are shown as histogram, fitted shapes as red lines and the green lines show the fitted backgrounds with contaminants.

5.3.4 Measured Quadrupole Deformation of Band AB

Double gated spectra, used for lineshape fitting, were created for each angle of detectors using the program REBEL. The gate list includes the 261.3, 371.0, 522.4 and 551.1-keV transitions. Spectra at three angles (50°, 90° and 130°) were used for lineshape analysis. The detectors at 50° and 130° are referred to as the forward and backward directions and are symmetric about 90°. The 607.3 keV transition was the lowest-spin γ-ray to show any Doppler broadened lineshape. The data from the forward and backward detectors were fitted simultaneously. The fitted peak shapes of the band AB are shown in Fig. 5.11-5.16 for the 607.3, 684.1, 751.0, 812.2, 874.8 and 938.8-keV transitions. The results of the lifetimes and the corresponding quadrupole moments are listed in Table 5.2.

Table 5.2: Lifetimes and quadrupole moments of the transitions of the band AB in ^{168}Hf.

$I_i \rightarrow I_i$	E_γ (keV)	τ (ps)[a]	Q_t (eb)[b]	Q_s (eb)
$20^+ \rightarrow 18^+$	607.3	0.67±0.07	6.48±0.34	6.48±0.50
$22^+ \rightarrow 20^+$	684.1	0.34±0.04	6.73±0.35	4.66±0.42
$24^+ \rightarrow 22^+$	751.0	0.25±0.04	6.25±0.49	4.56±0.26
$26^+ \rightarrow 24^+$	812.2	0.18±0.04	6.01±0.67	4.57±0.27
$28^+ \rightarrow 26^+$	874.8	0.11±0.04	6.25±1.03	4.40±0.27
$30^+ \rightarrow 28^+$	938.8	0.07±0.01	6.56±0.29	3.99±0.30

[a] The symmetric error bars on τ are calculated using the propagation formula for errors, whereby the relative error on τ is twice that on Q_t.
[b] The symmetric error in Q_t are given by the computer code.

It should be noted that although several contaminant peaks are included in the fit (Fig. 5.11-5.16), the ratio of the calculated lineshape component to the total fitted curve remains unchanged. Moreover, whether or not this contaminant peak is included, the lineshape of the transition and hence the associated quadrupole moment

is unaffected. It is, therefore, only introduced to present the data in a better way. The relative error in the lifetime is small and most of the uncertainty comes from systematic errors in the stopping power during the slowing-down process, which could be as large as 15%.

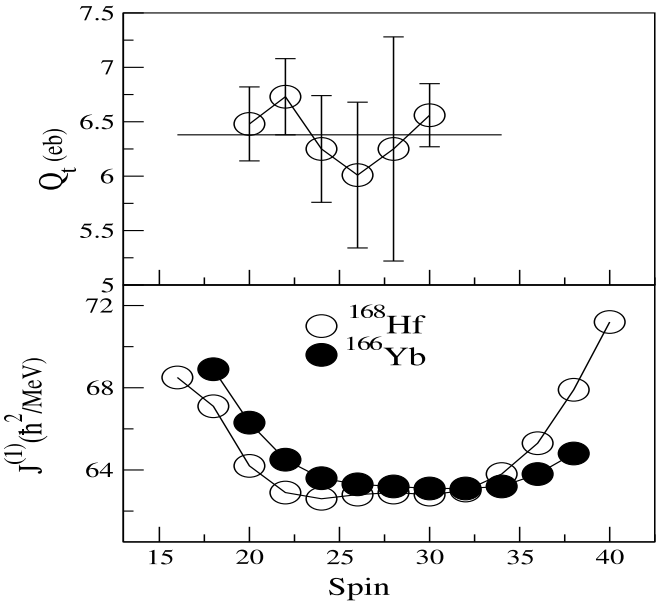

Figure 5.17: The quadrupole moment, Q_t, extracted from lifeshape analysis (top) and kinetic moment of inertia $J^{(1)}$ (bottom) as functions of rotational frequency for the band AB. The solid line in top panel represents the averaged Q_t.

Based on the measured lifetimes and extracted Q_t of the high-spin states in band AB, it is possible to achieve experimental information on the nuclear shape and to compare it with calculations. The deformation parameter β_2 was calculated using the expression

$$Q_t = 0.0126 Z A^{2/3} \beta_2 (1 + 0.36\beta_2) \cos(\gamma + 30^o), \tag{5.3}$$

which gives $\beta_2 = 0.24$ for $Q_t = 6.4$eb, assuming $\gamma = 0$. In ^{166}Yb, an isotone of ^{168}Hf, J.C. Bacelar et al. [78] report that the measured lifetimes suggest a change in shape around spin $30\hbar$. Our lifetime measurement doesn't provide any evidence of any change in shape between spin 20 and 30 for the yrast band in ^{168}Hf. Thus, there is no major loss of collectivity towards higher yrast states and the nucleus still remains very collective at spin 30^+, as can be seen from nearly constant Q_t values. This is also justified by Fig. 5.17 where a constant value for the kinetic moment of inertia, $J^{(1)}$, is observed over that range of spin. However, an upbend, as described in section 6.2.1, is seen around spin 32 due to the proton alignment which, presumably, did not cause a change in shape and deformation. It should be noted that any change in shape indicated by Q_t, if so, will alter $J^{(1)}$ too as $J^{(1)}$ is also influenced by the shape, alignments and pairing correlations. Due to the fact that, in the well-deformed region around ^{168}Hf, the alignment of the $i_{13/2}$ neutron does not affect the shape appreciably because of the stiffness of the potential and the higher position of the Fermi level, our experimental result is in excellent agreement with our theoretical understanding in this spin range. The measured quadrupole deformation, $\beta_2 = 0.24$, is also in satisfactory agreement with $\beta_2 = 0.25$ for the ND minimum obtained from the UC calculation.

CHAPTER VI

QUASIPARTICLE CONFIGURATIONS AND BANDCROSSINGS IN NORMAL DEFORMED BANDS

6.1 Cranking Calculations for ^{168}Hf Using the Ultimate Cranker Code

Cranked-shell model calculations have been carried out for ^{168}Hf using the Ultimate Cranker [79, 80] code, with the resulting Nilsson orbitals shown in the Quasiparticle diagrams (Fig. 6.1), indicating the neutron and proton orbitals relevant to our level scheme. Pairing was taken into account and the standard parameters were used from Ref. [81]. The quasiparticle Routhians for ^{168}Hf are depicted in Fig. 6.1. In this figure the adopted notation A, B, C, D are the first lowest unique-parity single-particle orbitals for neutrons while a, b, c, d are those for protons (Table 6.1). This is discussed in more detail later. Table 6.2 summarizes the experimental and calculated band crossings for most of the new bands. The configurations for the previously known bands will be discussed briefly and that for seven new bands will be discussed in detail.

Since there are only two good quantum numbers in the CSM, the Routhians can be labeled with one of four different assignments: $(\pi, \alpha) = (+, +\frac{1}{2})$ = solid line, $(+, -\frac{1}{2})$ = dotted, $(-, +\frac{1}{2})$ = dash-dotted, and $(-, -\frac{1}{2})$ = dashed. In order to avoid confusion, the trajectories are labeled with the Nilsson quantum numbers that are valid at $\hbar\omega$

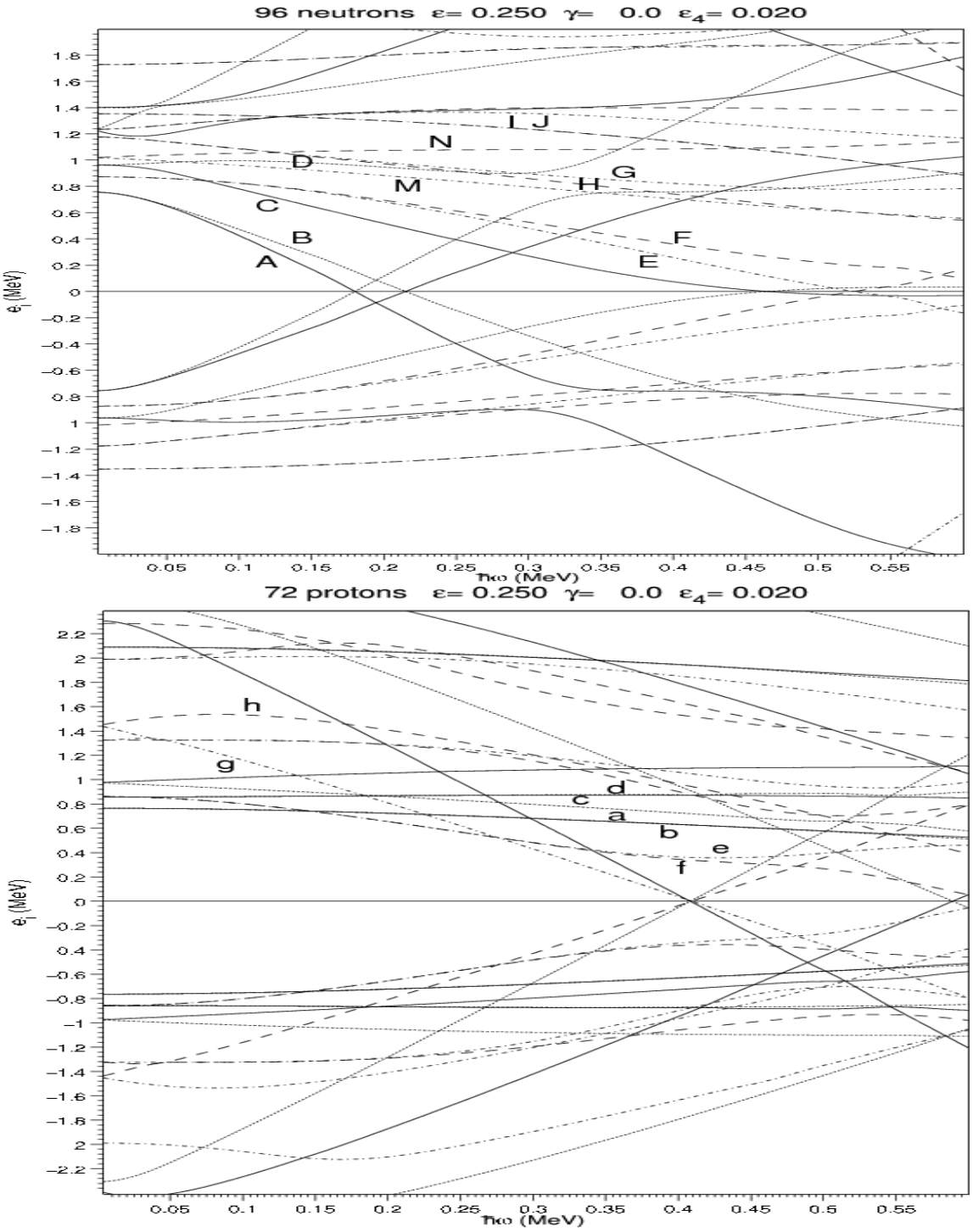

Figure 6.1: Quasiparticle diagram for neutrons (top) and protons (bottom) for ^{168}Hf calculated at β_2=0.254, β_4=0.002 and γ=0. The levels are labeled by parity and signature as (+, +1/2) solid lines, (+, -1/2) dotted lines, (-, -1/2) dashed lines, and (-, +1/2) dot-dashed lines.

Table 6.1: Quasiparticle labeling convention for ^{168}Hf.

Spherical shell Models States	Nilsson orbitals	Labels	
		$\alpha = +1/2$	$\alpha = -1/2$
$\nu i_{13/2}$	$\nu[642]\frac{5}{2}^+$	A	B
$\nu i_{13/2}$	$\nu[651]\frac{3}{2}^+$	C	D
$\nu h_{9/2}$	$\nu[523]\frac{5}{2}^-$	E	F
$\nu f_{7/2}$	$\nu[521]\frac{3}{2}^-$	G	H
$\nu p_{3/2}$	$\nu[521]\frac{1}{2}^-$	M	N
$\nu h_{11/2}$	$\nu[505]\frac{11}{2}^-$	I	J
$\pi g_{7/2}$	$\pi[404]\frac{7}{2}^+$	a	b
$\pi d_{5/2}$	$\pi[402]\frac{5}{2}^+$	c	d
$\pi h_{11/2}$	$\pi[514]\frac{9}{2}^-$	e	f
$\pi h_{9/2}$	$\pi[541]\frac{1}{2}^-$	g	h
$\pi i_{13/2}$	$\pi[660]\frac{1}{2}^+$	m	n

= 0 MeV. A convention of the lowest two positive-parity proton orbitals receiving the labels **a**...**c** and the two lowest energy negative-parity proton orbitals having the label **e**...**g** has been employed. The inverse convention is used for the neutrons and the lack of a lower case discriminates a neutron from a proton. This information is summarized in Tables 6.1 which should be used in conjunction with Fig. 6.1. One may notice from Fig. 6.1 that every trajectory has an equal and opposite trajectory reflective about e$\prime$ = 0 Mev. These negative energy trajectories, below $\hbar\omega = 0.25$ MeV, have been given the negative label since the signature has been inverted (*i.e.* e'_{α} = -$e'_{-\alpha}$). If the system has an even amount of particles, then one considers all of the negative energy levels are filled and all of the positive trajectories are open at low rotational energy ($\hbar\omega < 0.25$ MeV). If there is an odd number of particles, then all of the negative energy levels are filled at low energy and one particle may fill any

of the positive quasiparticle trajectories. Of course those levels which lie lowest in energy are the most likely to be filled. Characteristics of the experimental rotational bands may be predicted by extracting information from the associated trajectory. For example, alignment, which is the amount of angular momentum projected onto the axis of rotation by the unpaired particles of the nucleus, can be predicted from the Routhians. The alignment from a quasiparticle is equal to the negative slope of the Routhian trajectory [82]

$$\imath = -\frac{de'}{d\omega} \tag{6.1}$$

where $\imath$ is the alignment. Therefore, one may observe from Fig. 6.1 that the (**a**, **b**) band should have more alignment than either the (**e**,**f**) or (**g**,**h**) bands at low rotational energy in ^{168}Hf. This indeed is found to be experimentally true as will be discuseed in the following sections.

Table 6.2: Comparison of observed and calculated band crossing frequencies and experimental alignment gain in ^{168}Hf.

Band	Crossing	$\hbar\omega_{exp.}$ (keV)	$\hbar\omega_{cal.}$ (keV)	$\Delta\hbar\omega$	i_x gain ($\hbar$)
AE	BC	310	300	+10	3.0
AF	BC	280	300	-20	2.8
AG	BC	290	300	-10	5.0
	AD	400	325	+75	
AH	BC	275	300	-25	5.0
	AD	375	325	+50	
AM	BC	290	300	-10	4.5
HK-3	BC	290	300	+10	3.3
X2	AD	400	325	+75	2.8

6.1.1 Band Crossings

Multi-quasiparticle bands may interact and "cross" lower seniority[1] bands. Fig. 2.13 shows an example of such a crossing for ^{168}Hf. The plot displays the excitation energy of the levels in two bands minus the energy for a rigid rotor as a function of spin. The Coriolis and centrifugal forces pull in opposite directions on the two particles paired in a time reversed orbit. Therefore, as the nuclear rotation increases, these forces increase their strengths which will pull the particles out of their orbits and align them both with the rotational axis. The most susceptible particles to this alignment are those in high-j orbitals. The $i_{13/2}$ neutrons in the mass A$\approx$ 150 region are the highest j particles observed and thus are the first to align. One can observe from Fig. 2.13 that at higher spins the AE-band (which has two aligned $i_{13/2}$ and $h_{9/2}$ neutrons i.e. A and E) is energetically favored and thus more likely to be observed.

These band crossings are represented by the inflection points where the trajectories of similar parity and signature repel from each other in Fig. 6.1. The first occurrence is observed at $\hbar\omega \approx 0.28$ MeV in the quasineutron diagram. An interaction between the $\pm$A and $\pm$B levels results in the -A and -B quasineutrons crossing into the positive energy portion of the diagram. This represents the AB (two $i_{13/2}$ neutrons) particles aligning at a crossing frequency of $\hbar\omega \approx 0.28$ MeV. One may note that other band crossings are possible between the BC, AD, and CD neutrons. Experimentally, these band crossings are easily observed by the large amount of alignment gained in the band. This gain in alignment results from the once paired particles (whose angular momentum summed to zero) aligning their angular momentum in the same direction as the nuclear rotation. The CSM can predict how much alignment gain should occur in a particular band crossing. Alignment is an additive property, so to find

[1]Seniority defines the number of quasiparticles upon which the configuration of a band is based.

the amount of alignment gained from an AB crossing, one simply adds the negative slopes of the A and B trajectories. Extensive comparisons of the experimental band crossing frequencies ($\hbar\omega_c$) and alignment gains to the CSM will be discussed.

It is not necessary that all band crossings show up experimentally which appear in the quasiparticle diagrams of Fig. 6.1. For instance, let's consider the band based on the **a** proton. Since there is a particle in **a** trajectory, it would violate the Pauli principle to allow the -**b** particle to occupy the same level. Therefore the **ab** band crossing may not occur and is customarily known as a blocked band crossing. There will be no experimentally observed alignment gain at the predicted $\hbar\omega_c$ which will confirm the configuration assignment of that particular band.

6.1.2 Total Routhian Surface

Total routhian surface (TRS) calculations determine the total routhian through a surface of deformation parameters β_2, β_4 and γ for a given nucleus (Z, N). The calculations employ the Ultimate Cranker approach using UC code. These calculations can be performed on various nuclei and at various rotational frequencies ($\hbar\omega$). The total routhian is minimized with respect to the deformation parameters β_2, β_4 and γ, with β_2 and γ being transformed into the cartesian coordinates X and Y, given by [83]

$$X = \beta_2 \cos(\gamma + 30^\circ) \tag{6.2}$$

$$Y = \beta_2 \sin(\gamma + 30^\circ) \tag{6.3}$$

The total routhian is actually minimized at each (β_2, γ) lattice point with respect to β_4 after which the equilibrium deformation is minimized over the entire lattice. The calculations are such as to allow various nuclear configurations to be set up for

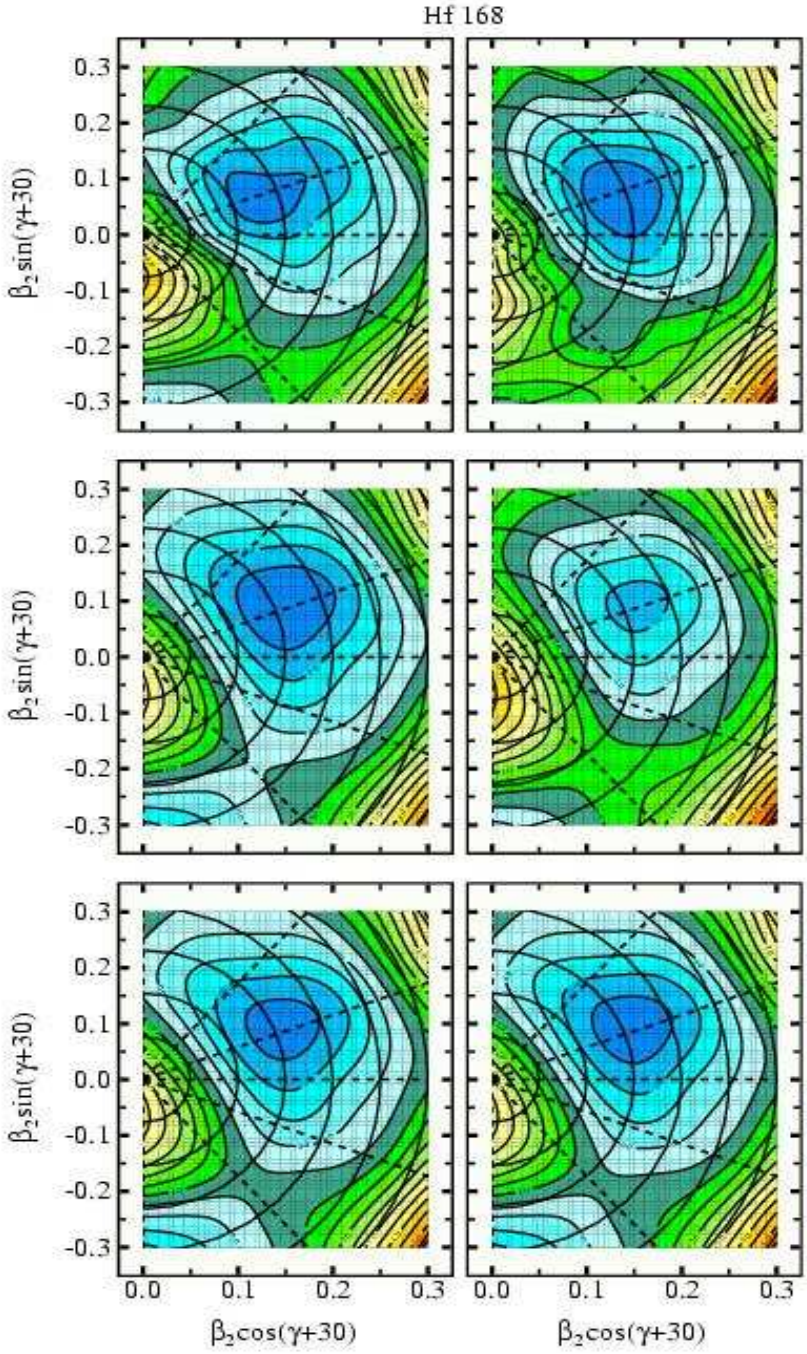

Figure 6.2: Total energy surfaces for ^{168}Hf, showing the ND minima. The contour line separation is 0.5 MeV.

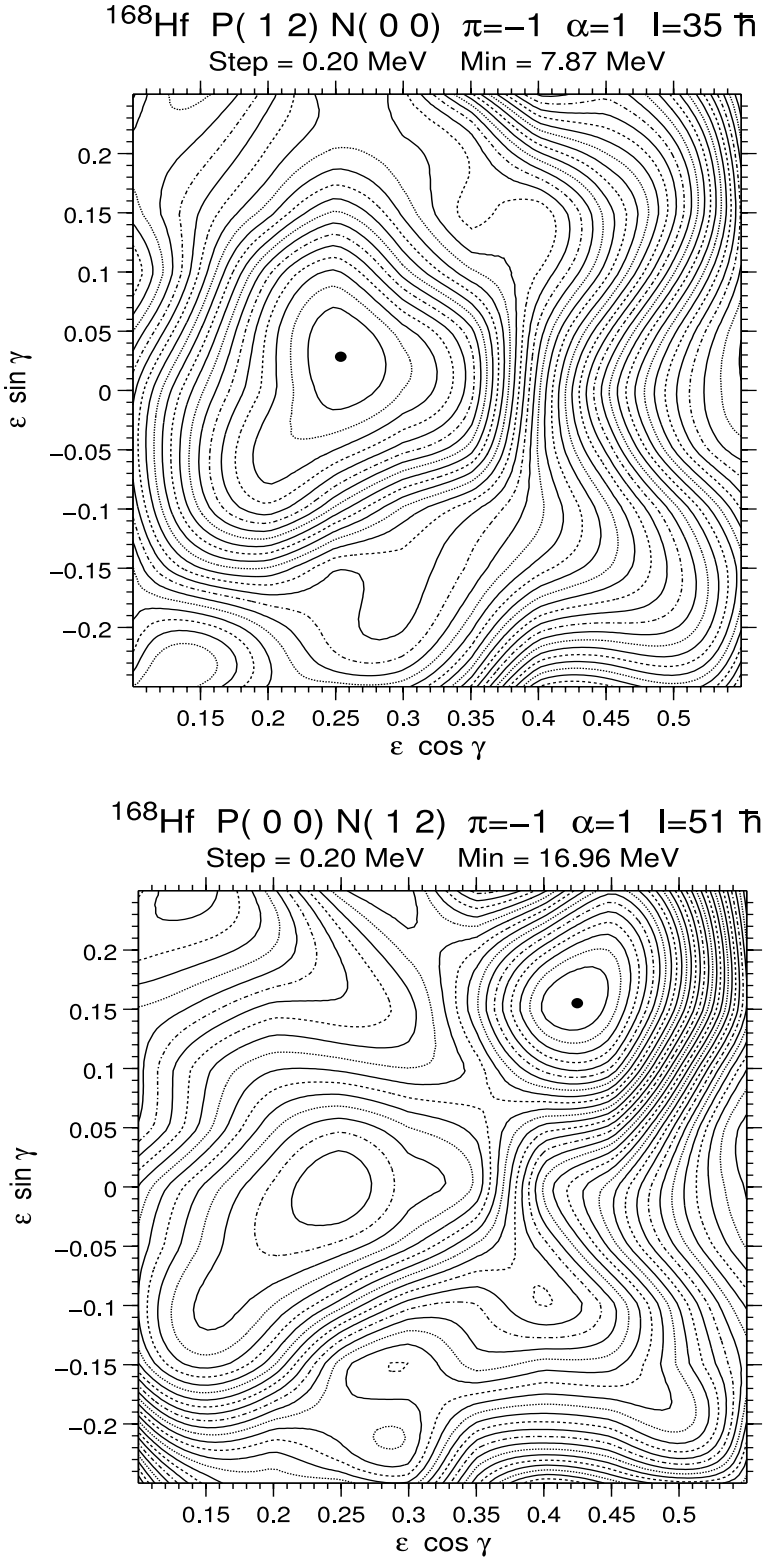

Figure 6.3: Total energy surfaces for the P(0,0)N(1,2) (lower) and P(1,2)N(0,0) (upper) configurations, which contain the lowest TSD and ED minima, respectively. The contour line separation is 0.2 MeV.

minimization, in that it is possible to perform the calculations for various signature and parity combinations in the nucleus of interest. The resulting TRS plots show the energy contours which result from the minimization procedure over the entire lattice. The potential-energy surfaces for ^{168}Hf are plotted in Fig. 6.2 and 6.3 for different rotational frequencies, showing ND, ED and TSD minima. The calculations used a Cranked Woods-Saxon potential with universal parameters [36].

6.2 Low-K Band Configurations

6.2.1 Bands AB, AE, AF and BE

Similar bands with configurations AB, AE, AF and BE were also reported previously for the isotones ^{166}Yb, ^{170}W and for the isotope ^{166}Hf [4, 12, 84]. Fig. 6.4 shows the alignment plot of bands G, AB, AE, AF and BE for isotones ^{166}Yb and ^{170}W, and isotope ^{166}Hf of ^{168}Hf as a function of the rotational frequency. For a better representation, an identical reference with Harris parameters ζ_0= 28$\hbar^2$ MeV^{-1} and ζ_1 = 42$\hbar^4$ MeV^{-3} has been chosen for all four nuclei. Band G is crossed by band AB at $\hbar\omega \sim 0.37$ MeV which represents the alignment of a pair of neutrons at the [642]5/2$^+$ orbital. The two strongest negative-parity bands, AE and AF, undergo BC crossing at $\hbar\omega \sim 0.3$ MeV, and there is little signature splitting thereafter (Fig. 6.4). The low-lying octupole vibrational band, as reported in Ref. [4], may have caused a gradual increase in the alignment of $\sim 4\hbar$ for these bands. They do not show any evidence for an AB band crossing near $\hbar\omega = 0.2$ MeV which is blocked by the already occupied orbital A. This observation, as well as the negative parity of the band, are all consistent with the characteristics of a neutron configurations for them *i.e.* AE and AF.

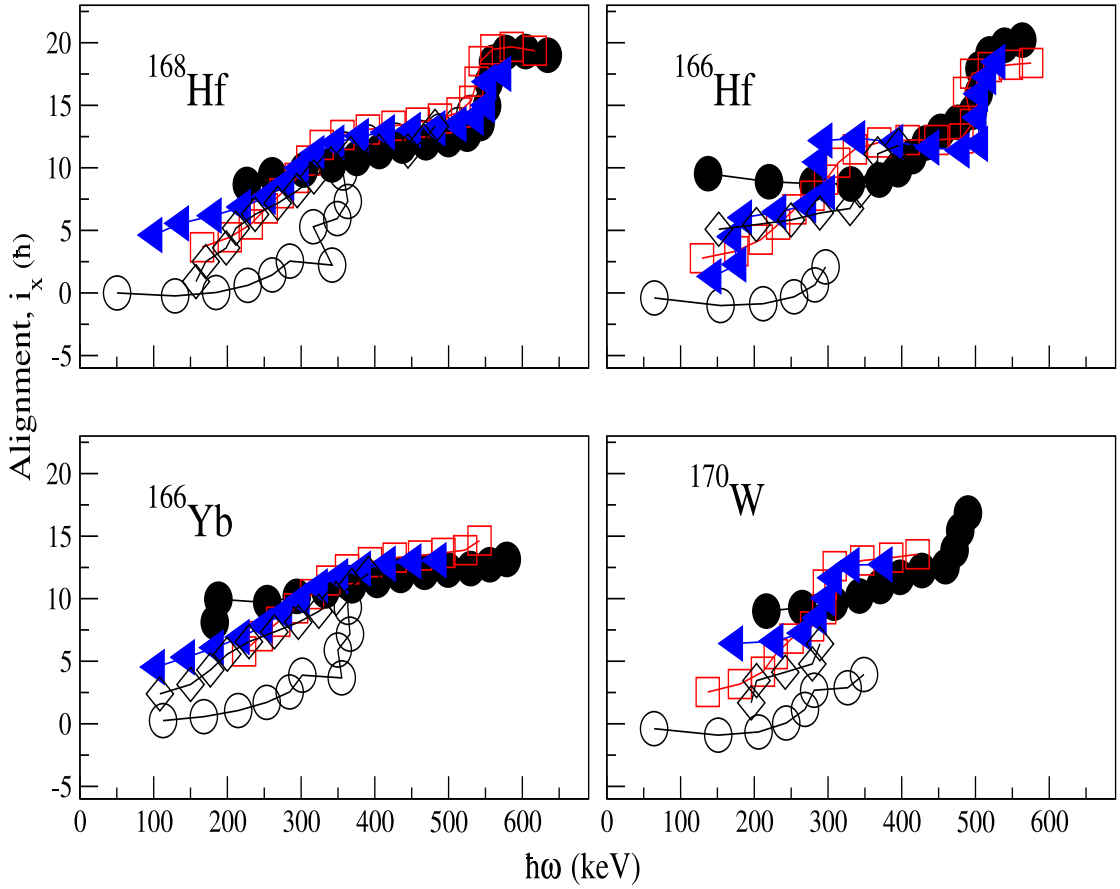

Figure 6.4: Alignment versus $\hbar\omega$ of bands G, AB, AE, AF and BE deduced from the experiment: ^{168}Hf [present work], ^{166}Hf [4], ^{166}Yb [84] and ^{170}W [12]. Open circles represent the band G, full circles the AB band, open squares the AE band, full squares the AF and open diamond the BE band.

Band BE does not show any indication of AB or BC alignment. Its excitation energies are above the AE and AF bands. As suggested by E. M. Beck [1] and S. Jonsson [85], this band is either mixed with or the continuation of the octupole band.

The bands AB, AE and AF exhibit another crossing at higher rotational frequency ($\hbar\omega \sim 0.5$ MeV) with the alignment of $\sim 6.2\hbar$ and we interpret this as the first proton crossing. Similar proton crossings have previously been proposed in ^{169}Hf [65], ^{167}Hf [86] and ^{166}Hf [87]. The proposed configuration of the proton pair responsible for the second upbend is gf, or $\pi([541]1/2^{-}(\alpha = +1/2) \otimes \pi([514]9/2^{-}(\alpha = -1/2)$. Should this configuration be responsible for the upbend in all three bands, the dispersion in crossing frequencies could possibly be explained by the fact that these crossing frequencies are sensitive to deformation changes since the $[541]1/2^{-}$ orbital is particularly deformation driving. Alternatively, one might also consider the configuration mb, or $\pi([660]1/2^{+}(\alpha = +1/2) \otimes \pi([404]7/2^{+}(\alpha = -1/2)$. The UC calculations show that the alignment of this pair may occur at frequencies similar to that of the mixed gf crossing. The pronounced down-sloping of the $\pi[660]1/2^{+}$ orbital as a function of rotational frequency is well known, and this orbital alone is expected to contribute about $5.7\hbar$ to the alignment. For the bands AE and AF in ^{166}Yb and ^{170}W, the full alignment cannot be ascertained as they have not been observed at sufficiently high spins. "Wiggles" can be seen in the curve for the ground-state band (G) because of its interaction with the AB band which is closest in energy [1, 84].

6.2.2 Bands AG and AH

Figures 6.5, 6.6 and 6.7 show the plots for excitation energy minus rigid-rotor references versus spins, aligned angular momentum and experimental routhians, respectively, for new bands observed in this study. The routhian diagram [Fig. 6.7] shows very little signature splitting between bands AG and AH for spins below 20, which strongly suggests that they are signature partners based on the same orbitals. They also interact with each other at the lowest spins. The bands undergo BC cross-

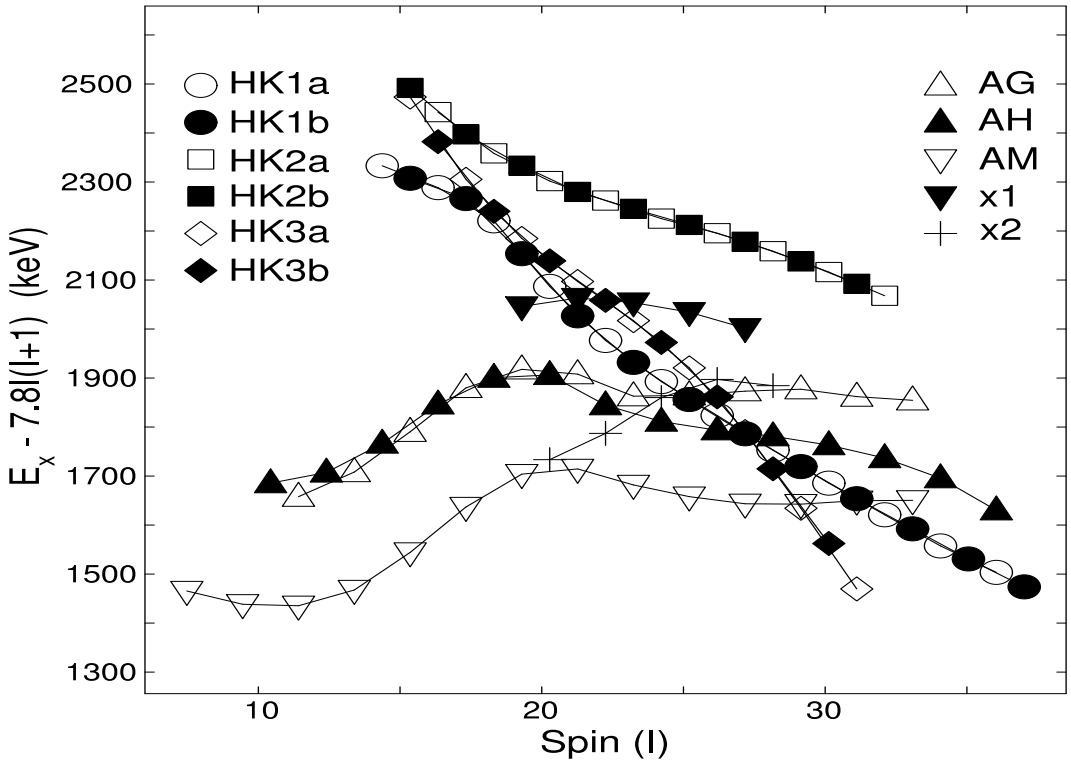

Figure 6.5: Excitation energies minus a rigid rotor reference as a function of spin for new bands in ^{168}Hf. The Harris parameters used are $\zeta_0 = 28\hbar^2$ MeV^{-1} and $\zeta_1 = 42\hbar^4$ MeV^{-3}.

ing (Fig. 6.6) at $\hbar\omega \sim 0.33$ MeV with an apparent alignment gain of $\sim 5\hbar$. The missing AB crossing is understood as a blocking phenomenon and consequently, this band must contain A neutron orbital. The neutron orbitals I and J (Fig. 6.1) lie far away from the Fermi surface and they are very unlikely. The presence of [521]3/2$^-$ (G, H) is justified from Figures 6.6 and 6.7, where very similar, both theoretically (Fig. 6.1) and experimentally, signature splitting between G and H can be observed around a rotational frequency of 0.3 - 0.5 MeV. Since the excitation energy of band AH is slightly smaller than that of the band AG, this is also in good agreement with the UC calculations (Fig. 6.1), where the orbit H lies below the orbit G. Thus, the two-quasiparticle configuration AG, AH are the most probable configuration.

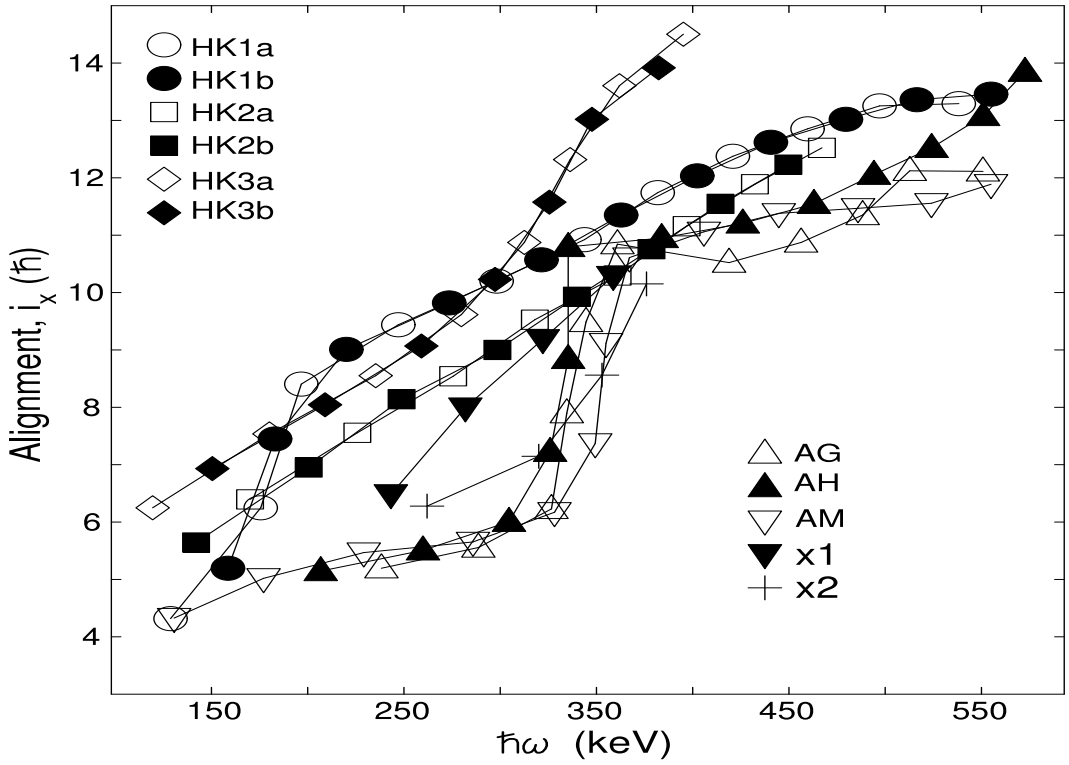

Figure 6.6: Alignments of new bands with Harris parameters $\zeta_0 = 28\hbar^2$ MeV^{-1} and $\zeta_1 = 42\hbar^4$ MeV^{-3}.

6.2.3 Band AM

The band AM does not show AB band crossing; however, BC crossing is present at $\hbar\omega \sim 0.3$ MeV with the alignment of $\sim 5\hbar$. In Fig. 6.8, the alignment and routhian of band A of ^{169}Hf is compared to that of band AM showing that they exhibit similar behavior. It points to the fact that the orbital A $[642]\frac{5}{2}^+$ is the prime configuration candidate for band AM. Its excitation energies are just above the AE and AF bands which rules out the coupling of A with E or F. Among the two possibilities, M or N from neutron orbital $[521]\frac{1}{2}^-$, orbital N can be ruled out as it pushes the band to higher excitation energy than that of the bands AG and AH (see Fig. 6.1), which is experimentally not true. Based on this argument, the possible two-quasineutron

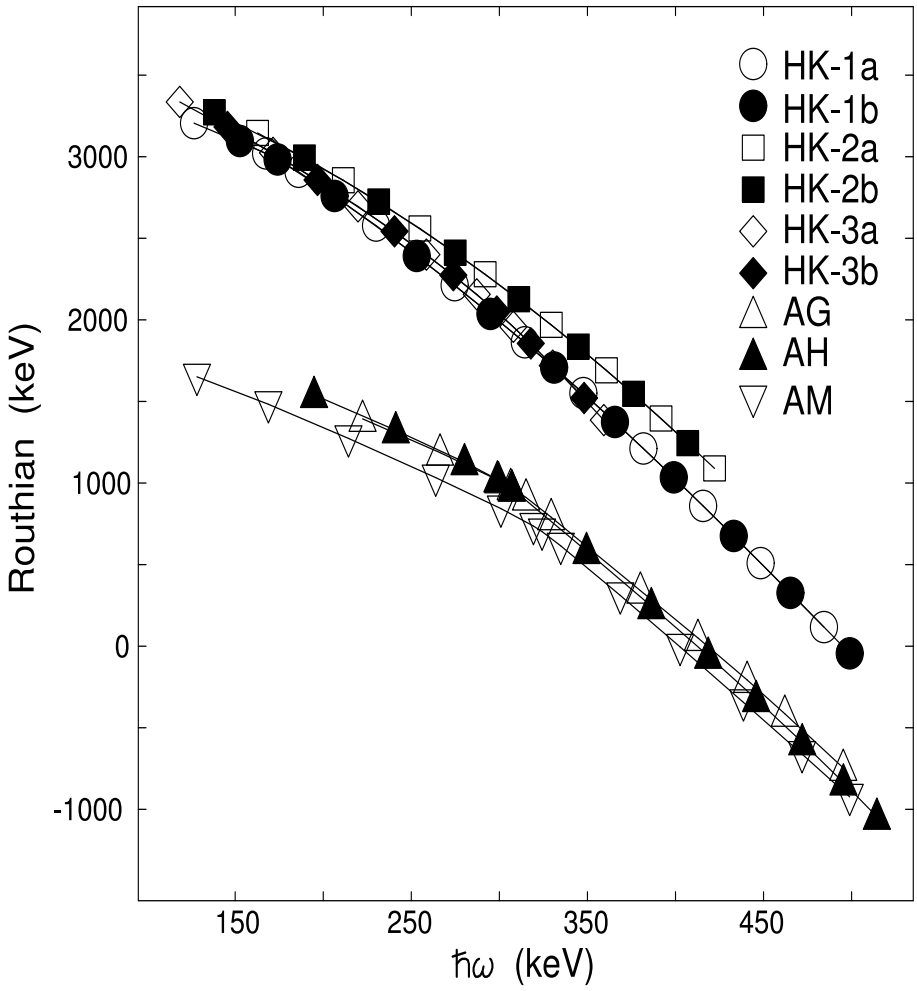

Figure 6.7: Routhians versus rotational frequency for new bands, except X1 and X2 relative to a reference with Harris parameters $\zeta_0 = 28\hbar^2$ MeV^{-1} and $\zeta_1 = 42\hbar^4$ MeV^{-3} in ^{168}Hf.

configurations could, therefore, be AM. The signature partner is not observed because of the expected strong signature splitting.

6.2.4 Bands X1 and X2

These two bands are very short. Band X1 seems to show AD crossing, and thus neutron orbital B could be involved in its configuration. Band X2 seems to undergo BC crossing, and thus neutron orbital A could be involved in its configuration.

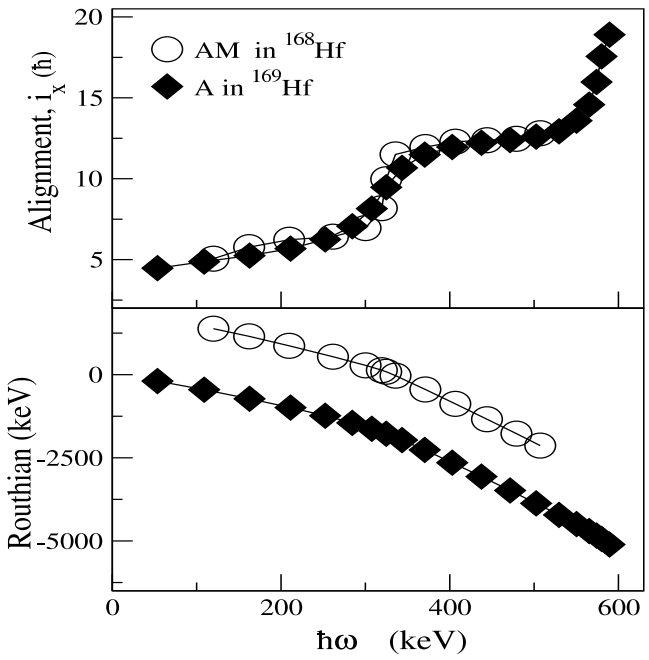

Figure 6.8: Alignments (top) and routhians (bottom) of band AM in ^{168}Hf and band A in ^{169}Hf with the same Harris parameters as in Fig. 6.5.

6.3 High-K Band Configurations

To find possible configurations on which high-K bands are built, their B(M1)/B(E2) ratios extracted from in-band M1/E2 branching ratios are compared with calculated values relevant to the possible configurations, as described below. Their alignment patterns, excitation energy, dynamic moment of inertia and the routhians are also compared with that of high-K bands of neighboring nuclei ^{167}Hf, ^{169}Hf, ^{166}Yb, ^{167}Yb and ^{168}Yb , where they exhibit similar characters.

Relatively large alignment, high excitation energy and strong M1 transitions suggest that the high-K bands in ^{168}Hf are associated with four quasiparticle structure consisting of two neutrons and probably two protons.

A high-K band, as the name refers, should be based on high-Ω orbitals which can boost high components of angular momentum along the symmetry axis (simply called K). Most neutron orbitals do not yield high-Ω in this mass region, except the neutron state $[505]11/2^-$ which is, however, slightly far below the Fermi surface[2] if one takes smaller β deformation into account. The proton high-Ω orbitals available are $[514]9/2^-$ ($h_{11/2}$), and $[404]7/2^+$ ($g_{7/2}$) (Table 6.1). Employing the tilted cranking model, J.R.B. Oliveira et al. [88] has suggested three high-K bands in ^{166}Yb, ^{167}Yb and ^{168}Yb, based on similar $[505]11/2^-$, $[523]7/2^-$ and $[404]7/2^+$ states which are also reported in several Er, Dy, Gd, and Sm odd-N isotopes, and in ^{149}Nd and ^{167}Yb [89]. Although the proton states are usually not active due to the gap at Z=70, a $I^\pi = K^\pi = 8^-$ state might have been created due to the excitation of two quasiproton states $[514]9/2^-$ and $[404]7/2^+$. As mentioned above, Ref. [88] has reported high-K bands built on a similar $K^\pi = 7^-$ state, which justifies their involvement in such high-K structures.

One of the best techniques to investigate the wavefunctions of nuclear states is to compare the experimentally determined γ-ray transition probabilities between states versus theoretical predictions. This is often possible by measuring directly the ratio of the intensities of γ-rays which de-excite collective states. Strongly coupled rotational bands with $K \neq 0$ are composed of two sequences of stretched quadrupole transitions (I $\rightarrow$ I-2) which are linked by stretched dipole transitions (I $\rightarrow$ I-1). Important quantities such as the deformation of the nucleus and what quasiparticles are associated with

[2]The Fermi surface is the highest energy orbital occupied by the last neutron or proton.

a given band can be deduced from these transition probabilities. The E2 transition is the most common transition in the deformed rotational structure of the rare-earth region. For coupled bands with connecting ΔI = 1 mixed M1/E2 transitions, the experimental values of B(M1, I $\rightarrow$ I-1)/B(E2, I $\rightarrow$ I-2) have been extracted from the expression

$$\frac{B(M1)}{B(E2)} = 0.693\frac{T_1}{T_2}\frac{E_2^5}{E_1^3}\frac{1}{1+\delta^2} \tag{6.4}$$

where subscripts 1,2 refer to the ΔI = 1 and ΔI = 2 transitions, respectively. E and T are respectively the intensity and γ-ray energy in MeV while δ is the E2:M1-mixing ratio given by

$$\delta = \sqrt{0.7}E_\gamma\frac{\langle I|M(E2)|I-1\rangle}{\langle I|M(M1)|I-1\rangle} \tag{6.5}$$

It is apparent from Eq. 6.5 that for a pure E2 transition, δ goes to infinity, while for the case of a pure M1 transition, δ vanishes. The effect of the mixing ratio on the branching ratio is the following: when the mixing is dominated by E2, the mixing ratios are large, and when the M1 dominates, the $(1+\delta^2)^{-1}$ term has essentially no effect. Moreover, the correction is in general less than 10% and has, therefore, been neglected. The calculated B(M1) values are based on an extension of the geometrical model of Ref. [90]:

$$B(M1, I \rightarrow I-1) = \frac{3}{8\pi I^2}\left\{\sqrt{I^2-K^2}\left[\sum_\jmath (g_\jmath - g_R)\Omega_\jmath\right] - K\left[\sum_\jmath (g_\jmath - g_R)\imath_\jmath\right]\right\}^2 \mu_N^2 \tag{6.6}$$

The value used for the collective gyromagnetic ratio is $g_R = 0.35$. The intrinsic g factors, $g_\jmath$, used for the different quasiparticle orbitals (see Table 6.1) are A, B, C, D: -0.28; E, F: 0.25; G, H: -0.61; e, f: 1.29; g:0.76; a, b: 0.63; c, d: 1.57; k: 1.35. The

values of g_J have been calculated from the wavefunctions in Ref. [91]. For the aligned quasineutron pair (BC) a summed alignment of $6\hbar$ together with K = 0 has been used. The theoretical B(E2) values have been calculated according to the expression [92]

$$B(E2, I \rightarrow I-2) = \frac{5}{16\pi} Q_o^2 \langle IK20|I-2K\rangle^2 \tag{6.7}$$

where Q_o is the transition quadrupole moment (often determined from lifetime measurements - see Chapter V).

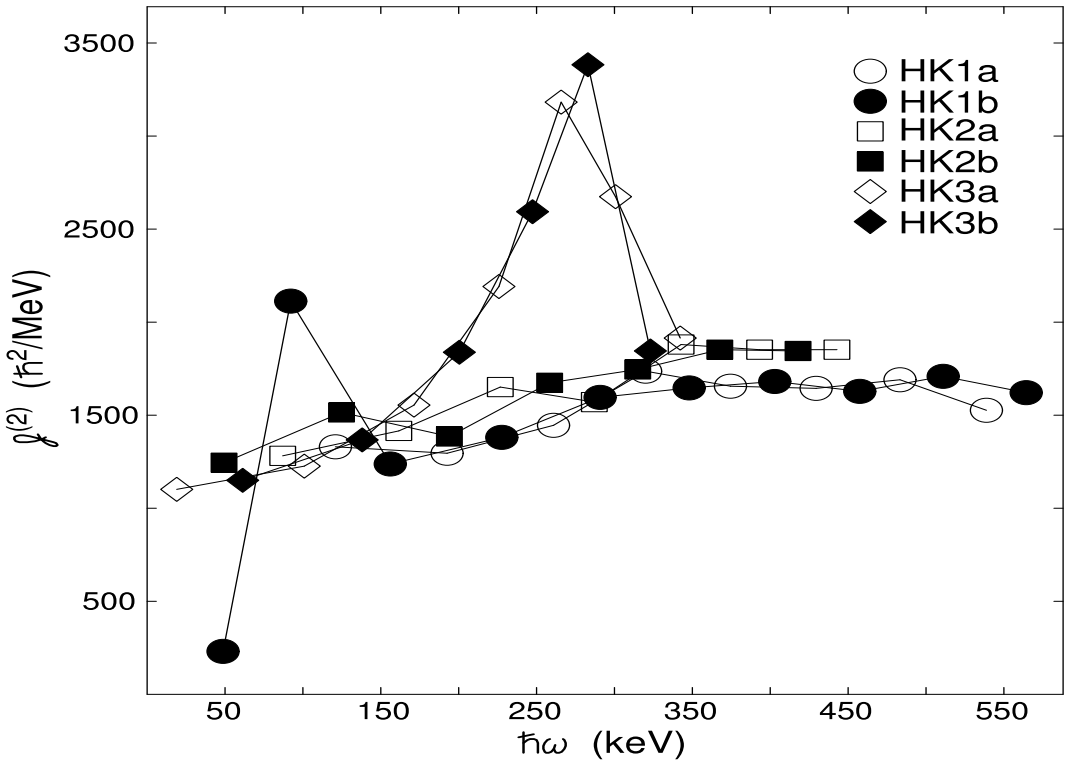

Figure 6.9: Dynamic moment of inertia $J^{(2)}$ as a function of rotational frequency for the high-K bands.

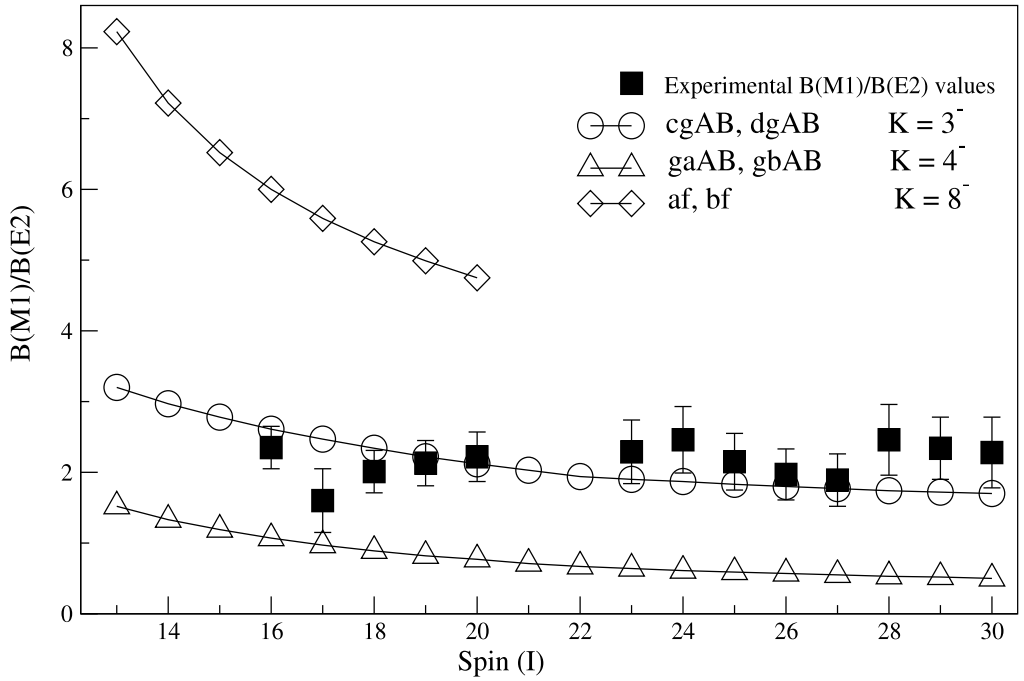

Figure 6.10: Experimental B(M1)/B(E2) ratios compared to theoretical calculations for the proposed configuration of the band HK-1.

6.3.1 Band HK-1

The dynamic moment of inertia for all high-K bands is depicted in Figure 6.9. The band HK-1 experiences a crossing at $\hbar\omega \sim 0.2$ MeV, which is interpreted as AB crossing (Fig. 6.5). The BC crossing around 0.3 MeV is clearly missing because of a blocking phenomenon, suggesting that the band must contain the B neutron orbital. Based on relatively large alignments and high excitation energy, the band should, as aforementioned, be composed of a four-quasiparticle structure involving protons which are supposed to play a major role for the corresponding alignment gain. The

alignment pattern follows that of band AB, and the initial alignment is higher than that of HK-2 and HK-3 which can only be caused by an AB neutron pair. Thus, the neutron configuration may involve AB. The full configuration proposed is (gaAB, gbAB), coupled to $K^{\pi} = 4^{-}$ as will be discussed in the following paragraphs. Figure 6.10 shows the experimental B(M1)/B(E2) values as a function of spin together with some relevant theoretical B(M1)/B(E2) values.

The quasiprotons having the lowest energies are c, f and g where two of them are negative parity. Therefore, the other possible configurations could also be (afAB, bfAB), (cfAB, dfAB) and (cgAB, dgAB) with $K^{\pi} = 8^{-}$, 7^{-} and 3^{-} respectively. However, for the configuration (afAB, bfAB), the experimental B(M1)/B(E2) value becomes too high and out of scale in Fig. 6.10. In addition, the AB crossing frequency is 0.21 MeV, lower than the 0.25 MeV in the yrast band. If we replace the proton 'a' by 'c', this makes the B(M1)/B(E2) ratio even higher for the configuration (cfAB, dfAB). The B(M1)/B(E2) ratio of (gaAB, gbAB) agrees much better with experimental values. The ratios for (cgAB, dgAB) are good too, but this configuration can be discarded based on the fact that one should see the lower orbital $[404]7/2^{+}$ first rather than $[402]5/2^{+}$. According to UC calculation, the proton $[541]1/2^{-}$ orbital is lower than the $[404]7/2^{+}$ and $[514]9/2^{-}$ orbitals above a frequency of ~ 0.25 MeV. This orbital can be seen in the HK-2 (geBE/gfBE) and HK-3 (geAE/gfAE) bands, and is also present in ^{167}Lu and neighboring nuclei. The proton $[404]7/2^{+}$ orbital is higher than the $[514]9/2^{-}$ orbital (e or f) seen in HK-2 and HK-3, and total proton parity changes to negative for the ga/gb combination. These could be the reasons that the $[541]1/2^{-}\otimes[404]7/2^{+}$ combination is not seen in neighboring nuclei. The neutron configuration AB for HK-1 is much lower than that in HK-2 and HK-3 (BE and AE). This could make the total excitation energy of HK1 lower than HK-2 and

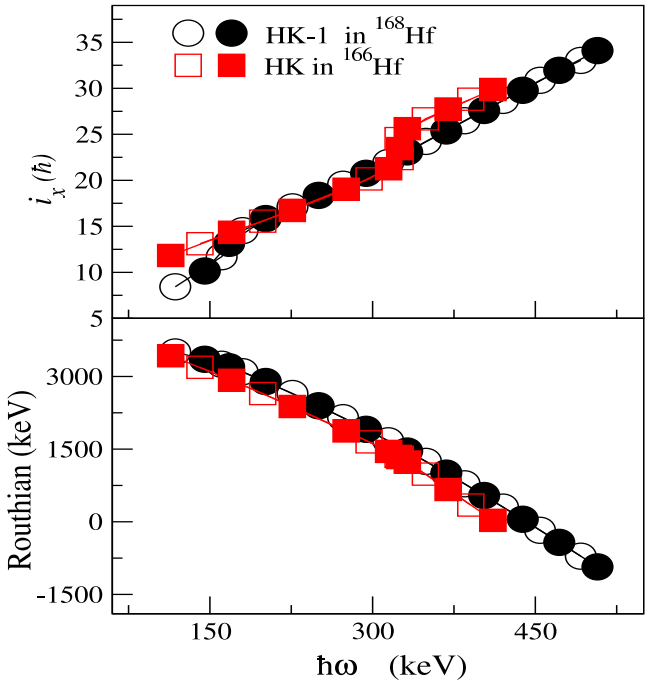

Figure 6.11: Alignments (top) and routhians (bottom) of HK-1 and a coupled band (HK) in ^{168}Hf and ^{166}Hf respectively, with the same Harris parameters as in Fig. 6.5.

HK-3. This is consistent with the fact that HK-1 has a lower energy than HK-2 and HK-3. The E1 decays out of HK-2 and HK-3 change the parities of the neutron wave functions, while in HK-1 these E1 decays change the parity for the proton wave functions.

The final choice of configuration of the band HK-1 is thus settled on (gaAB, gbAB). Using this low K-value (4), the AB crossing frequency is similar to that of the yrast band. The alignment gain looks fine too. The introduction of **g** *i.e.* the $[541]1/2^-$ proton orbital, is also supported by its involvement in a coupled band for

^{166}Hf [87]. In Fig. 6.11, the alignment and routhian of the HK-1 band in ^{168}Hf is compared to that of the coupled band in ^{166}Hf, where both bands exhibit similar alignments and routhians.

6.3.2 Band HK-2

The band HK-2 doesn't exhibit any band crossing (Fig. 6.5 and 6.6). The absence of both AB and BC crossing suggests that this band is likely to be built on a B neutron state. The alignment, before the BC crossing, is $\sim 1\ \hbar$ smaller than that in the band HK-3 which favors neutron configuration BE. Its alignment increases very smoothly and attains only the $\sim 3.5\ \hbar$ gain even during the long interval of rotational frequency. The initial angular momentum is around 6-7 $\hbar$. The B(M1)/B(E2) argument favors a configuration of two neutrons and two protons. The full configuration proposed is $\nu([642]5/2^{+}\otimes[523]5/2^{-})\otimes\pi([541]1/2^{-}\otimes[514]9/2^{-})$ (geBE, gfBE), coupled to $K^{\pi} = 10^{-}$, for which the calculated B(M1)/B(E2) ratios agree with the data (Fig. 6.12). Apart from HK-3, this will be another band based on deformation alignment. Other possible configurations are $\nu([642]5/2^{+}\otimes[523]5/2^{-})\otimes\pi([404]7/2^{+}\otimes[402]5/2^{+})$ (acBE, bcBE), coupled to $K^{\pi} = 11^{-}$ and $\nu([642]5/2^{+})^{2}\otimes\pi([404]7/2^{+}\otimes[514]9/2^{-})$ (aeAB, beAB), coupled to $K^{\pi} = 13^{-}$. However, (acBE, bcBE) can be discarded on the basis that the initial alignment is too small compared to the observed values. For (aeAB, beAB), this proton combination is also seen in heavier Hf isotopes, but the problem is that the band is extended to spins lower than the AB crossing frequency and maintain a pretty constant spin alignment. The neutron configuration is not AB.

The lowest state observed is 15^{-} which is greater than the calculated $K^{\pi} = 10^{-}$ band head, but this can be explained in terms of K-mixing. It is uncertain if the band has achieved the lowest observed state. Thus, either the lowest observed state

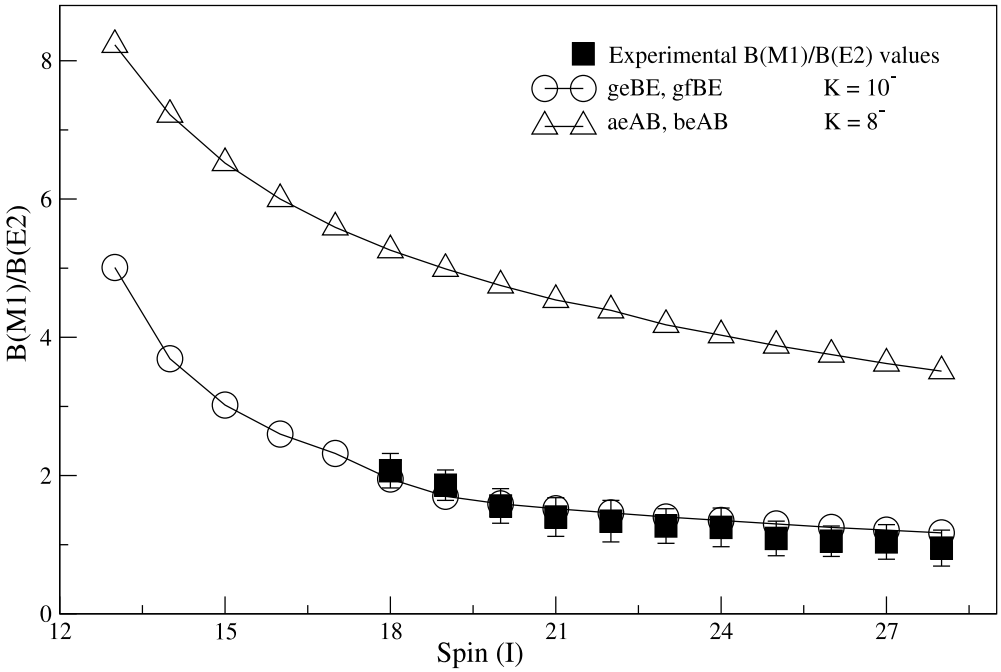

Figure 6.12: Experimental B(M1)/B(E2) ratios compared to theoretical calculations for the proposed configuration of the band HK-2.

$K^{\pi} = 15^{-}$ is not the true bandhead, or, if it is, the K-quantum number is strongly mixed [93].

Fig. 6.13 shows the alignment and dynamic moment of inertia of the HK-2 band in ^{168}Hf compared to that of a high-K band in ^{168}Yb where both bands exhibit similar characteristics. Both alignment curves rise very smoothly with rotational frequency, and they follow each other. None of their dynamic moments of inertia show any backbending and the points are just spread all over. Moreover, the four quasiparticle (two neutrons and two protons) structure of the high-K band in ^{168}Yb [88] with

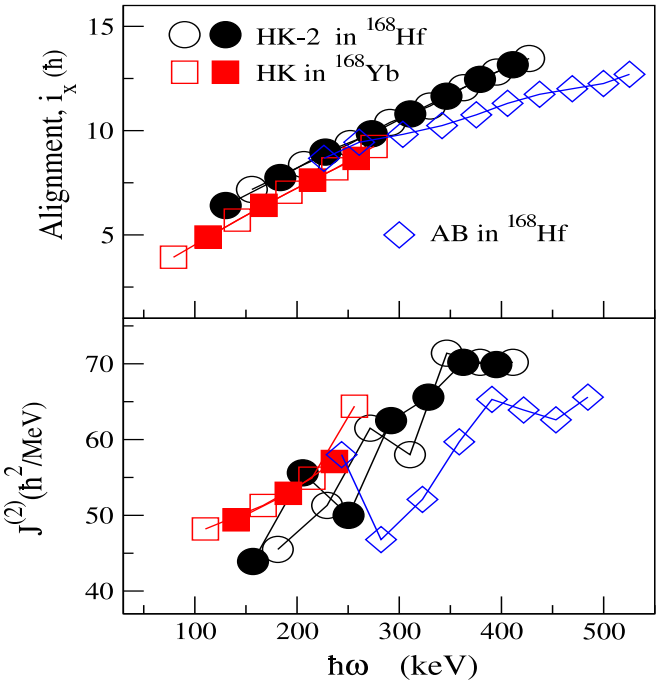

Figure 6.13: Alignments (top) and dynamic moment of inertia (bottom) of HK-2 and a high-K band in ^{168}Hf and ^{168}Yb respectively. The Harris parameters are kept identical.

the presence of identical $\nu[642]5/2^+$ orbitals provides supports to our configuration assignment of (geBE, gfBE) for HK-2 in ^{168}Hf.

6.3.3 Band HK-3

The band HK-3 has been assigned a similar configuration to the coupled band (geAE, gfAE) in ^{166}Hf [87]. The relatively large alignment and excitation energy (Figs. 6.5 and 6.6) suggest that this band is a four quasiparticle structure, probably also involving quasiprotons. The band undergoes BC crossing at $\hbar\omega \sim 0.3$ MeV, while

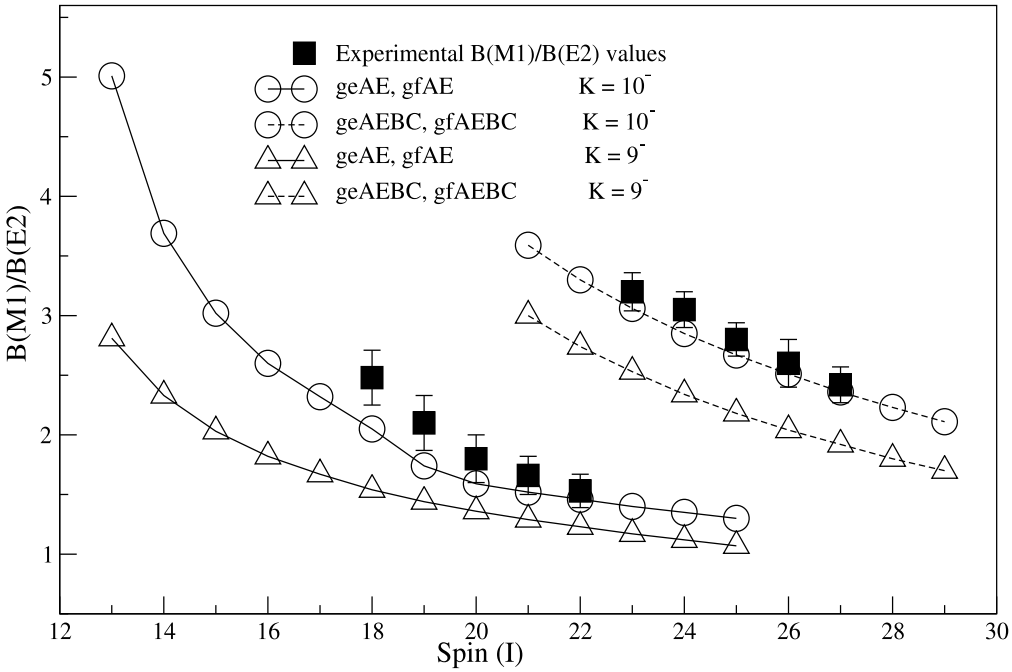

Figure 6.14: Experimental B(M1)/B(E2) ratios compared to theoretical calculations for the proposed configuration of the band HK-3, with and without an aligned (BC) neutron pair.

AB crossing around $\hbar\omega \sim 0.28$ MeV is clearly missing (see Fig. 6.6). Due to the fact that a BC crossing is observed, the band HK-3 must contain the A quasineutron. The other quasineutrons could therefore be D, E, F, G or H. The lowest combination of one of these with A is AE. The quasiprotons having the lowest energies are e, f and g, and are all of negative parity. A good candidate for the configuration is, therefore, $\nu([642]5/2^{+}\otimes[523]5/2^{-})\otimes\pi([541]1/2^{-}\otimes[514]9/2^{-})$, with different possibilities for the K quantum number. Another possibility, in which E is replaced by G, could be $\nu([642]5/2^{+}\otimes[521]3/2^{-})\otimes\pi([541]1/2^{-}\otimes\ [514]9/2^{-})$. Figure 6.14 shows the

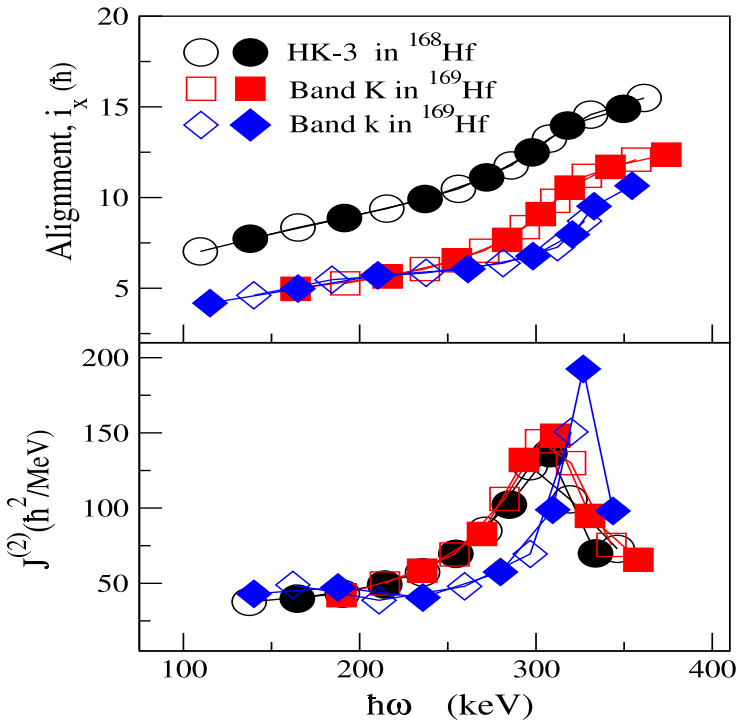

Figure 6.15: Alignments (top) and dynamic moment of inertia (bottom) of band HK-3 in ^{168}Hf and bands K and k in ^{169}Hf.

experimental B(M1)/B(E2) values as a function of spin together with some relevant theoretical B(M1)/B(E2) values. Accordingly, the configuration for the band HK-3 is proposed to be $\nu([642]5/2^{+}\otimes\ [523]5/2^{-})\otimes\pi([541]1/2^{-}\otimes[514]9/2^{-})$, (geAE, gfAE) coupled to $K^{\pi} = 10^{-}$. The agreement is striking also above $I = 23^{-}$, where the BC crossing must be included to match the observed experimental trend.

The other possible configuration, where the same orbitals couple to $K^{\pi} = 9^{-}$, has theoretical B(M1)/B(E2) values lower than the $K^{\pi} = 10^{-}$ configuration and the experimental values. If the E quasineutron is replaced by an F quasineutron corresponding

to the configuration (gfAF, geAF), the expected excitation energy becomes a little higher. The theoretical B(M1)/B(E2) values for this configuration are identical to those of (geAE, gfAE). If only E is interchanged with G or F with H, corresponding to the configurations (geAG, gfAG) or (gfAH, geAH), the theoretical B(M1)/B(E2) values become too small. The positive signature of the proton orbital $[660]1/2^+$, labeled m, is close to the Fermi surface as well, but B(M1)/B(E2) values of configurations involving this orbital together with $[404]7/2^+$ are too low compared to the experimental values.

Based on the arguments mentioned above, the final choice of configuration of the band HK-3 is settled on (geAE, gfAE) which has the lowest excitation energy of all candidates. Additional support can be gathered from Fig. 6.15 which exhibits very similar alignments and dynamic moments of inertia for the high-K bands k and K in ^{169}Hf, and for HK-3 in ^{168}Hf. It is impressive that all of them exhibit BC crossing while AB crossing is blocked. The roles of the $\nu[642]5/2^+$ and $\pi[514]9/2^-$ orbitals are justified by their presence in bands k and K, as suggested by K.A. Schimidt et al. [93].

6.4 Rotation and Deformation Alignment

The band HK-3 and the negative-parity band, AE, are both of six-quasiparticle nature at their highest spins, where they appear to have identical quasiparticles involved, namely gf AE BC and ge AE BC for the two signatures of the band HK-3, and AE BC gf for the band AE. The use of the same quasiparticle labels, though, can not be justified for both bands which are obviously quite different. In the band AE(BC) the two quasiprotons align their angular momenta along the rotational axis at high spin, as expected from the UC calculations in which principal axis cranking

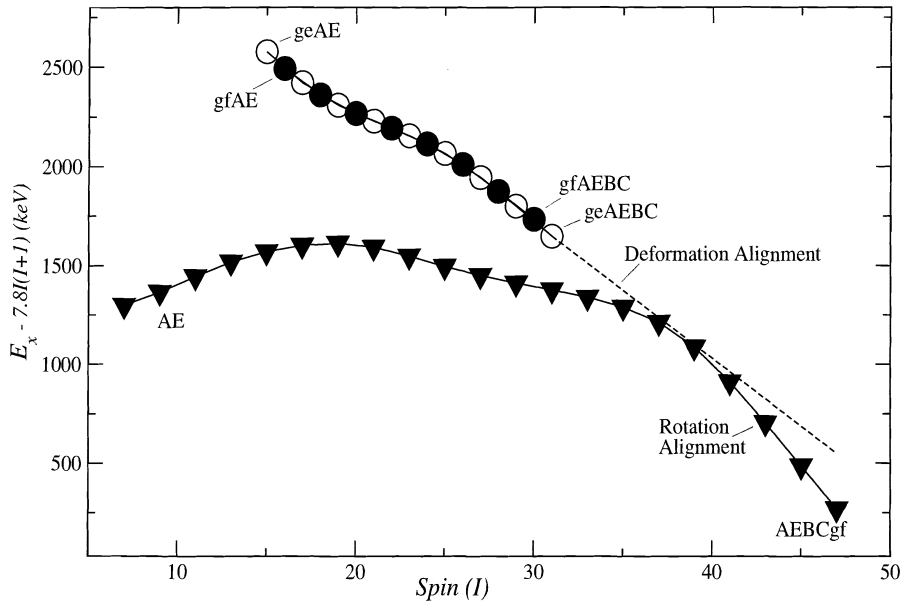

Figure 6.16: Excitation energy with a rigid rotor reference subtracted, as a function of spin, for the bands AE and HK-3 in ^{168}Hf.

(PAC) is realized. In the high-K band the quasiprotons must be coupled mainly to the deformation axis from the lowest spins. The high-K band is not a solution expected from PAC calculations. The high spin parts of the two bands, therefore, realize different coupling of particles in the same orbitals. These couplings apparently result in a difference in aligned angular momentum of $\sim 2.5\hbar$ (see Fig. 6.16). In Fig. 6.16, the two bands cannot be compared at identical spins, but a linear extrapolation of the energy for the coupled band, which may be justified from the constant alignment above $\hbar\omega \sim 0.3$ MeV, shows a preference of a few hundred keV for the rotation aligned coupling.

This case of co-existing coupling schemes is similar to the band (geAE, gfAE) in ^{166}Hf [87]. The four neutrons are most likely spectators, and the difference is to be traced to the coupling of the two protons. This is probably a resemblance to the cases

of s- and t-bands representing aligned and tilted coupling of the $i_{13/2}$ quasineutrons in some neutron-rich rare-earth nuceli [94]. As stated in Ref. [87], such rather exotic cases of six-quasiparticle bands call for more advanced theoretical considerations.

6.5 Summary

The current study of normal deformed bands in the even-even nucleus, ^{168}Hf, has led to the discovery of seven new bands and a substantial extension of the six previously known bands. Spins and parities of levels in the new bands have been assigned based on the measured DCO ratios of their decay-out transitions. All new bands, except X2, have been assigned negative parity. Of the seven new bands, three are high-K bands which form coupled pairs connected by strong M1 transitions. Based on our Cranked shell model calculations and a systematic comparison with neighboring nuclei, possible intrinsic configurations were suggested. High-K bands are proposed to be based on proton excitations and have been confirmed from B(M1)/B(E2) ratios. Bands AB, AE and AF have been extended to high spins where a second upbend can be seen clearly which are described by $h_{11/2}$ and $h_{9/2}$ proton alignment. It is concluded that these bands are associated with six quasiparticle configurations at higher spin.

Lifetimes of yrast states have been measured using the Doppler shift attenuation method. The extracted quadrupole deformation is in good agreement with predictions from TRS calculations. No reduction in collectivity has been observed. It is particularly interesting that the trend of collectivity at these high spin for yrast states in ^{168}Hf is different from that in ^{166}Yb where the B(E2) has been found to drop by $\sim 40\%$ [84].

CHAPTER VII

TRIAXIAL STRONGLY DEFORMED STRUCTURES

7.1 Introduction

The search for experimental signatures of triaxial nuclear shapes has proved to be very challenging. Potential energy surface (PES) calculations using different approaches, see e.g. Ref. [95, 96], predict that nuclei with Z$\sim$72 and N$\sim$94 constitute a region where such exotic shapes coexist with others associated with normal deformed (ND) prolate shapes. More systematic subsequent cranking calculations using the Ultimate Cranker (UC) code [79, 80] predict high-spin triaxial strongly deformed (TSD) minima with $(\varepsilon_2, \gamma) \sim (0.40, \pm 20^\circ)$ for nuclei in this region. These TSD minima are caused by large single-particle shell gaps associated with proton numbers $Z = 71$ and 72, and neutron numbers $N = 94$ and 97 [97, 98]. Indeed, TSD structures have been identified in several Lu isotopes and the wobbling[1] motion, a low-lying collective excitation mode characteristic of nuclei with stable triaxiality [99], has been established in ^{163,165,167}Lu [100-103] and, possibly, in $^{161}_{71}$Lu [104]. Further theoretical investigations based on the particle-rotor model [105, 106] and on the cranked shell model plus random phase approximation [107] pointed to the essential role of the rotation-aligned $i_{13/2}$ quasiproton which allows wobbling to compete in energy with quasiparticle exci-

[1] Like a failure of alignment causes wobbling in your car wheel, a triaxial-shaped rigid-body shows "wobbling motion" in its rotation.

tations in these Lu nuclei. An extensive search for TSD bands in Hf ($Z = 72$) nuclei has been carried out without success in proving triaxiality. The strongly deformed bands observed in $^{170-175}$Hf [108-111] were suggested to fall into two groups, labeled as ED and SD, based on their rotational properties and theoretical studies using the UC calculations and the Cranked Relativistic Mean-Field (CRMF) approach [109]. The ED bands are likely built on the proton $i_{13/2}h_{9/2}$ configuration, and are associated with near prolate shapes with $\varepsilon_2 \sim 0.3$, *i.e.*, deformations enhanced with respect to the normal deformed nuclear shapes, $\varepsilon_2 \sim 0.22$ characterizing the ground states. For the bands in the SD group, only band-2 in ^{175}Hf is linked to known structures [111]. The suggested intrinsic configurations of this band, and likely similar SD bands in $^{172-174}$Hf, involve the $\pi i_{13/2}$ (proton), as well as the $\nu j_{15/2}$ (neutron) orbitals originating above the $N = 126$ spherical shell closure. The SD bands are associated with superdeformed prolate shapes (CRMF calculated $Q_t \sim 11.6$ eb, compared to experimental values varying between 12 and 14 eb [110, 111]) with little triaxiality. Therefore, the UC and the CRMF calculations do not support a TSD nuclear shape for the reported SD bands in the heavier $^{170-175}$Hf isotopes. Pronounced triaxial minima exist in the calculations, but they would result in even smaller calculated quadrupole moments. Three candidate TSD bands were also reported in ^{168}Hf [2] which is closer to the UC predicted neutron shell gap, however, none of the bands were linked to the known structures. The second motivation of this dissertation research is to search for possible decay pathways of these bands and investigate their properties in order to understand their nature.

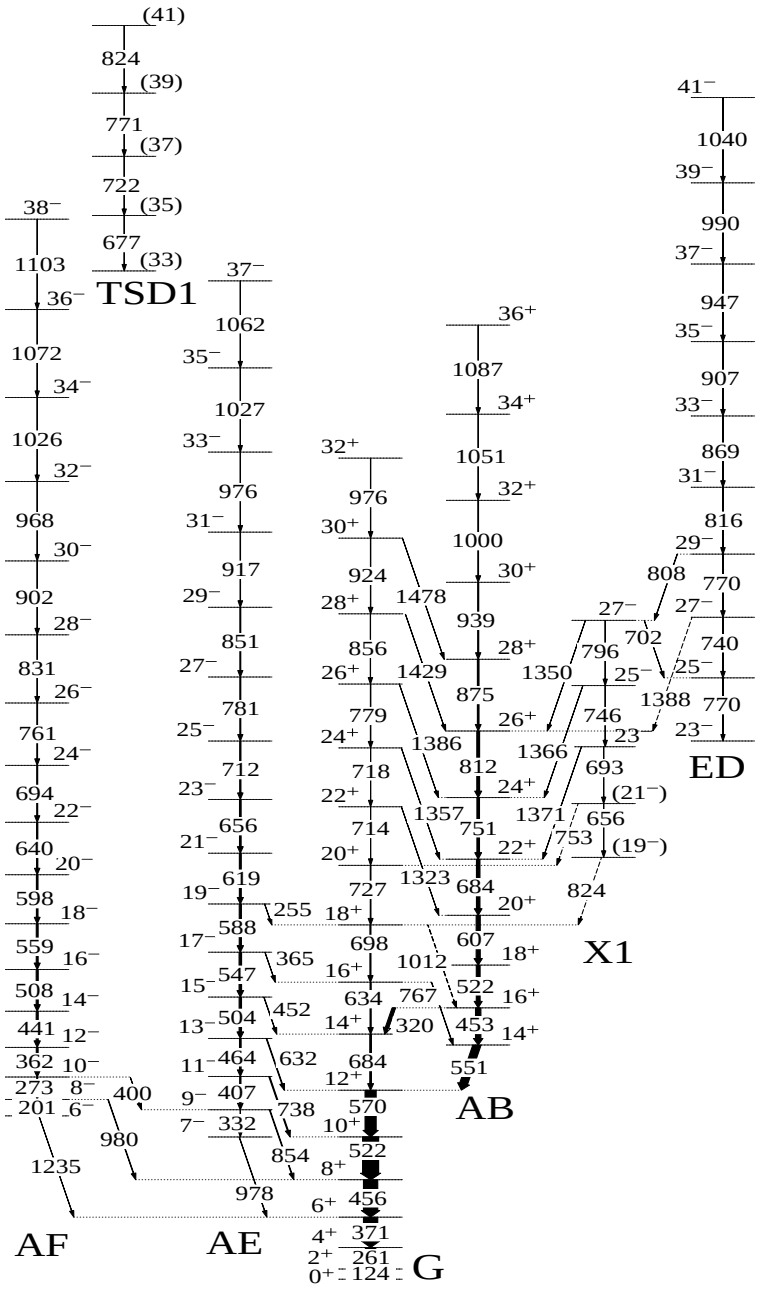

Figure 7.1: Partial level scheme of ^{168}Hf from this work. Gamma ray energies are in keV. Dashed lines represent tentative transitions. Gamma-ray energies of higher spin transitions in bands TSD1 (up to tentative 61 $\hbar$) and ED (former TSD2, up to 49 $\hbar$) are given on the spectra shown in Fig. 7.2. The spin, parity, and excitation energy of TSD1 are uncertain, see text for a detailed discussion. Band TSD2 (former TSD3) is not shown in the figure, its transition energies can be found in Ref. [2].

7.2 Experimental Results

A partial level scheme of ^{168}Hf from this study is presented in Fig. 7.1. The two weaker bands reported in the previous publication [2], TSD2 and TSD3, were renamed to ED and TSD2, respectively. The reason for the change will be discussed below. Other new results about ND structures are discussed in Chapter VI and will be published in an upcoming full paper [112]. The strongest depopulating transition from band ED to lower-spin ND structures is the 808 keV γ ray, which feeds the $I = 27\ \hbar$ level in the intermediate structure, band X1, before decaying to the yrast band AB. The intensities of the 808 keV decay-out and the 770 keV in-band transitions from the 29^- state are almost equal. Band X1 decays mainly to the band AB between the 26^+ and 22^+ levels with the 1371 keV γ ray being the strongest linking transition. Band X1 also feeds the bands G and AE. However, the linking transitions to band AE could not be established. Several depopulating transitions from bands ED and X1 can be seen in the spectrum of Fig. 7.2.

DCO ratios were measured for all transitions in the three candidate TSD bands, except for those very weak transitions at the highest spins, and the results were consistent with expectations for E2 cascades. The 1371 and 1366 keV transitions depopulating band X1 have DCO ratios of 0.49(9) and 0.69(10), respectively, consistent with a stretched dipole character. Furthermore, we suggest negative parity for band X1 because the linking transitions most likely have an E1 multipolarity. An M1 transition of such high energy would be expected to exhibit an E2 admixture resulting in a larger DCO ratio. The 808 keV decay-out transition from ED has a DCO ratio of 0.91(11) indicating either a stretched E2 or a $\triangle I = 1$ M1/E2 character. The large error in the DCO ratio, caused by the low statistics, does not allow us to make further

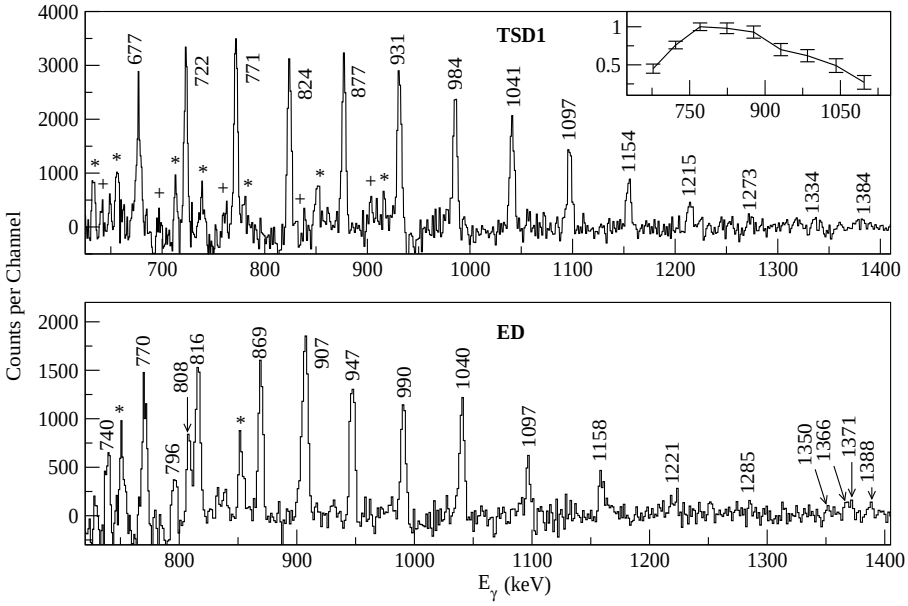

Figure 7.2: Gamma-ray coincidence spectra of bands TSD1 and ED in ^{168}Hf, doubly gated by the band members which are labeled by $\gamma-$ray energies. In the TSD1 spectrum, the stars and plus signs indicate transitions in the normal deformed bands AE and AF, respectively. The transition with the highest spin marked in band AE is 917 keV ($31^- \rightarrow 29^-$), and in band AF is 902 keV ($30^- \rightarrow 28^-$). The inset shows the intensity profile of band TSD1. In the ED spectrum, the decay-out transitions of bands ED and X1 are also labeled by energies, with the stars denoting the transitions in ND structures.

distinction between the two scenarios. However, the latter possibility can be ruled out since it would require the 702 keV γ ray, deexciting the 27^- level in X1 to a lower level in ED, to be an M3 transition, which is highly unlikely. Therefore, both the 808 and 702 keV γ rays are E2 transitions. The mixing of the two 27^- states in bands X1 and ED, which are 37.4 keV apart, causes the decay from ED to X1 and vice versa. This provides additional support for the spin/parity assignments for ED. Therefore, the band ED has a parity and signature $(\pi, \alpha) = (-, 1)$, i. e., it is associated with odd spins.

The band TSD1 decays mainly to the negative parity bands AE and AF, whose members can be seen in the coincidence $\gamma-$ray spectrum, doubly-gated on TSD1 transitions, as shown in Fig. 7.2. The intensity of band TSD1 decreases in the two lowest transitions, 722 and 677 keV (see inset of Fig. 7.2). Therefore, the decay-out from TSD1 occurs over the lowest three levels of the band. This fact, together with the observation that TSD1 decays to at least two different bands, must result in a highly fragmented decay pattern. The exact decay pathways from TSD1 to these two bands could not be established. However, all γ rays in TSD1, including the lowest 677 keV transition, are in coincidence with transitions in band AE below spin 31^- and in band AF below spin 30^-. The spin of the lowest TSD1 level would, most likely, be 32 $\hbar$ if this level decays to the 31^- state in band AE through a dipole transition, like the high-energy dipole γ rays in the statistical decay of the superdeformed bands in mass 150 and 190 regions [113, 114]. Such a one-step direct link is not observed. Another, possibly more plausible, scenario would be a two-step link between the lowest TSD1 level and the states in bands AE and AF, e.g., a situation similar to the decay from band ED to X1 through level mixing, with subsequent decay to the yrast line. This would result in a spin of 33 or 34 $\hbar$ for the lowest TSD1 level. Therefore, the spin of this level can only be determined approximately to be ~ 33 $\hbar$, or higher. Consequently, the highest level in TSD1 is 61 $\hbar$, which is typical for the highest spins observed for nuclei in this region, or higher. The possibility of a three-step link cannot be ruled out, but is less likely, since it would further raise the spin of band TSD1. The band decays to bands AE and AF, indicating its closer connection to the negative parity structures, but the parity of TSD1 could not be determined. Band TSD2, consisting of 9 transitions [2], is likely located at a higher excitation energy than TSD1 because it is more weakly populated. It feeds the yrast band, as well as

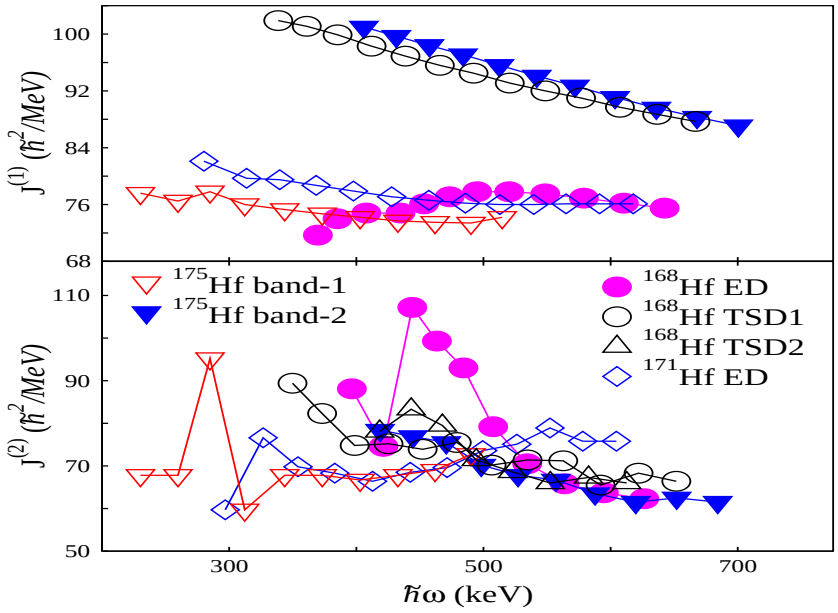

Figure 7.3: Kinematic ($J^{(1)}$) and dynamic ($J^{(2)}$) moments of inertia for highly-deformed bands in ^{168,171,175}Hf. The values for the $J^{(1)}$ moment of band TSD1 in ^{168}Hf are plotted based on the adopted spin values, see text for details.

another negative-parity ND band found in the present study (not shown in Fig. 7.1) [112], but its decay pathways could not be established.

7.3 Discussion

7.3.1 Band ED

The kinematic ($J^{(1)}$) and dynamic ($J^{(2)}$) moments of inertia are presented in Fig. 7.3 for the three bands in ^{168}Hf, the ED bands in ^{171,175}Hf [109, 111] and the SD band-2 in ^{175}Hf. The ED bands start from spins as low as $I \sim 15 - 20\ \hbar$. Their $J^{(2)}$ moments increase slightly with rotational frequency, excluding the low-spin region where the $J^{(2)}$ values are affected by paired band crossings and/or by interactions with ND bands. Over the entire frequency range, the $J^{(1)}$ moment of band ED in

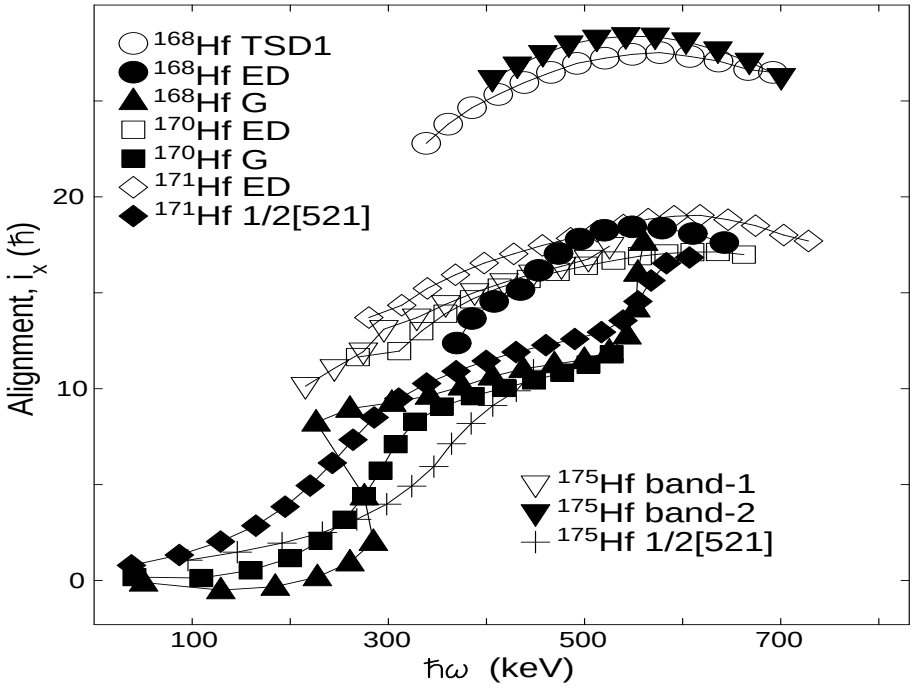

Figure 7.4: Aligned angular momenta as a function of rotational frequency for the highly deformed bands and some ND bands in ^{168}Hf and ^{170,171,175}Hf. The band TSD1 in ^{168}Hf is plotted with the adopted spin values. Identical Harris parameters, $I_0 = 30\ \hbar^2/MeV$ and $I_1 = 40\ \hbar^4/MeV^3$, were used for all bands.

^{168}Hf is similar to those of the ED bands in the heavier Hf isotopes, which are ∼20% larger than those of the ND bands in these nuclei. The $J^{(2)}$ moment of band ED in ^{168}Hf exhibits large irregularities, partly indicating a character change at lower spins, and partly reflecting the interaction with band X1. Its aligned angular momentum i_x (see Fig. 7.4) is comparable to those of the ED bands in ^{170}Hf [108] and ^{171,175}Hf, and is clearly larger than that of the yrast band AB, which is an extension of ground state band G after the first $i_{13/2}$ neutron band crossing at a rotational frequency $\hbar\omega \sim 0.28$ MeV. The large initial alignment at low frequencies is typical for structures with aligned high-j quasiparticles. Band ED in ^{168}Hf starts at a higher rotational frequency ($\sim$ 0.38 MeV) than other ED bands, and its alignment increases gradually to 6.5 $\hbar$ above that of the yrast band, possibly due to a changed character at the lowest spins.

The first proton alignment observed around $\hbar\omega \sim 0.55$ MeV in the ND bands is clearly missing in all ED bands.

In order to understand the intrinsic configurations of the ^{168}Hf bands, we performed cranking calculations using the UC code. Pairing is taken into account in the code, and the standard parameters [81] were used for the Nilsson potential. The calculated configurations are labeled as P(π_1, α_1)N(π_2, α_2). For protons, $\pi_1 = 0$ (or 1) represents the positive (or negative) parity, and $\alpha_1 =$ (signature $\times$ 2). The π_2 and α_2 symbols are defined similarly for neutrons. There are four theoretical bands with an aligned angular momentum close to that of band ED. They all have the proton configuration P(l,2), see Fig. 7.5. Of the four neutron configurations, N(0,0) is energetically favored, lying about 0.5 MeV below the nearly degenerate configurations N(l,0) and N(l,2). The N(0,2) configuration has the highest energy, lying about 0.7 MeV above the N(0,0) configuration. The P(1,2)N(0,0) configuration has $(\pi, \alpha) = (-, 1)$, i.e., negative parity and odd spins, in agreement with the values established for band ED. The configurations P(l,2)N(l,2) and P(l,2)N(1,0) are signature partners with practically no signature splitting. Such bands are not observed experimentally. Therefore, band ED is likely associated with the configuration P(1,2)N(0,0), or $\pi(i_{l3/2}h_{9/2}) \otimes \nu(i_{13/2})^2$. The UC calculated excitation energies for such a band, minus a rigid-rotor reference, are compared with the experimental values in Fig. 7.6. The experimental bands are shifted down by 3.4 MeV so that the average energies of levels between 14 - 36 $\hbar$ in the yrast band overlap with those of the calculated band. The calculated ED band fits the observed band ED well, but with a slightly lower excitation energy. In addition, the calculated aligned angular momenta are 5.6, 2.5, 6.1 $\hbar$ for the $\pi i_{13/2}$, $\pi h_{9/2}$, and $\nu(i_{13/2})^2$ orbitals, respectively, with a total alignment of 14.2 $\hbar$. This amount is slightly higher than the 12.3 $\hbar$ initial alignment of band ED which actually approaches

this value with increasing spin, as shown in Fig. 7.4. The potential energy surface for the P(1,2)N(0,0) configuration is presented in Fig. 6.3 for $I = 35\ \hbar$. The ED minimum is located at $(\varepsilon_2, \gamma) = (0.26, 9.3^o)$. This deformation is slightly enhanced compared to the ND bands, but similar to deformations calculated for the ED bands observed systematically in ^{170,171,175}Hf [109]. These bands are all built on the proton $i_{13/2}h_{9/2}$ configuration, but are coupled to different neutron configurations.

7.3.2 Band TSD1

Band TSD1 and the SD band-2 in ^{175}Hf [111] are located at higher spins than the ED bands. Their $J^{(1)}$ moments are considerably larger than the $J^{(2)}$ values and both $J^{(1)}$ and $J^{(2)}$ moments decrease smoothly with increasing rotational frequency. The large

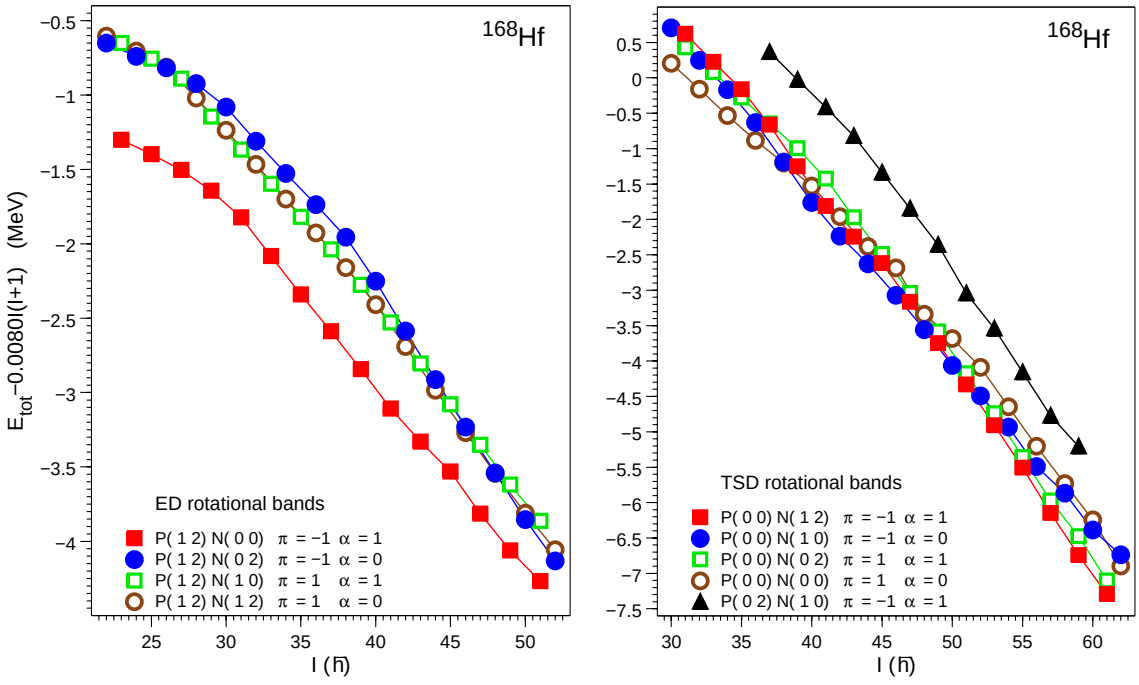

Figure 7.5: Theoretically calculated energies of ED bands (left) and TSD bands (right). A rigid-rotor reference energy has been subtracted.

aligned angular momentum of TSD1 in ^{168}Hf can be achieved in configurations involving one or two $i_{13/2}$ protons and at least one $j_{15/2}$ neutron. In UC calculations, all sixteen configurations which represent the lowest energy for all possible combinations of proton and neutron parity and signature, fulfill this requirement at a TSD shape for at least a part of the experimentally observed spin range. The calculations, as depicted in Fig. 7.5, show that the proton configuration P(0,0) is energetically favored by 1 MeV or more, compared to other proton configurations. The four neutron configurations, on the other hand, lie much closer in energy; over most of the experimental spin range they are within 0.3 MeV of each other. It is, therefore, likely that the observed band TSD1 will have the P(0,0) proton configuration, combined with a neutron configuration which cannot be specified further in view of the small energy differences just noted. Thus, four configurations are possible for band TSD1. If the band has negative parity, the configuration is either P(0,0)N(1,2) (odd spin) or P(0,0)N(1,0) (even spin). If the band has positive parity, the configuration is either P(0,0)N(0,0) (even spin) or P(0,0)N(0,2) (odd spin). The proton configuration is always the same, namely $\pi(i_{13/2})^2$, and all four neutron configurations contain one neutron in the $j_{15/2}$ subshell. The negative parity bands have a slightly lower energy than the positive parity ones, suggesting that the observed band TSD1 may have negative parity. The most probable intrinsic configuration is then $\pi(i_{13/2})^2 \otimes \nu(j_{15/2}i_{13/2})$. The excitation energies of the P(0,0)N(1,2) configuration are plotted in Fig. 7.6 together with that of band TSD1 with a bandhead spin $I = 33\ \hbar$ and an assumed energy of 12.55 MeV, which fits the calculated band the best. The uncertainties in the assumed energy of the lowest TSD1 level will change the vertical position of the plotted band. With the rigid-rotor reference energies chosen in the plot, the band TSD1 appears like a straight line. The slope of the line is closely related to the moment of inertia and

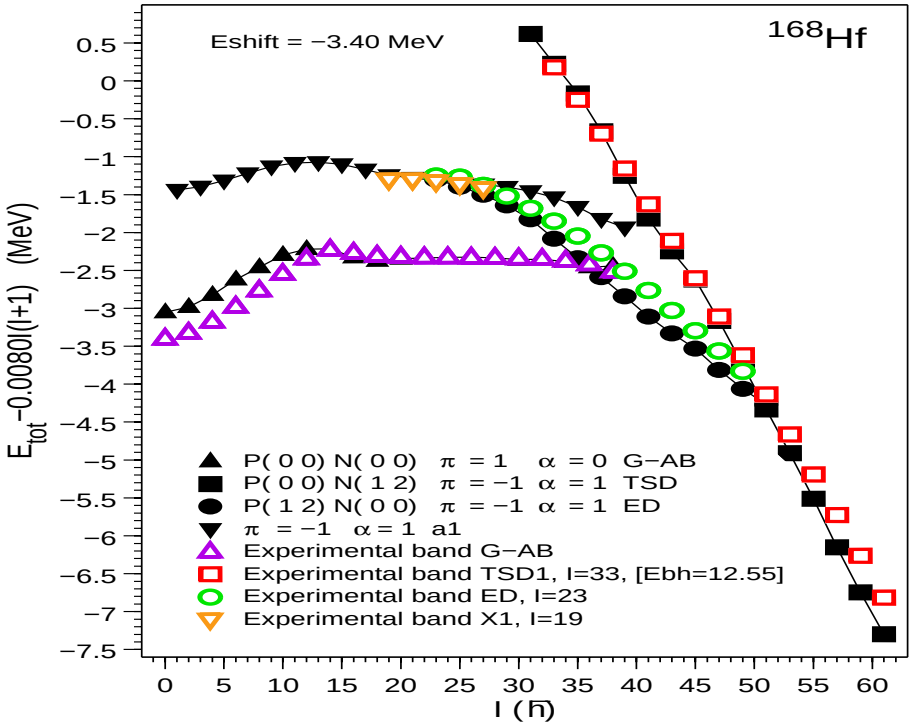

Figure 7.6: Experimental and UC calculated excitation energies minus a rigid-rotor reference for bands in ^{168}Hf. The experimental bands are shifted down by 3.4 MeV so that the average energy of levels between 14 - 36 $\hbar$ in the yrast band overlaps with that of the calculated band. The zero point of the energy scale corresponds to the spherical non-rotating liquid drop energy. Band TSD1 is plotted with assumed bandhead spin and energy values, as discussed in the text. The calculated band a1 is a prime candidate for the ND band X1.

to the spin assumed for the bandhead. If the adopted spin of TSD1 is changed by 1 $\hbar$, the slope of the line changes by $\sim 5.3\%$. The calculated quadrupole moment of such a band is ~ 10.5 eb, in agreement with the experimentally measured value of $Q_t = 11.4^{+1.1}_{-1.2}$ eb [2], and is substantially larger than $Q_t \approx 6.4(0.5)$ eb for the yrast band [112]. As seen in the potential energy surface in Fig. 6.3, the calculated band is associated with a TSD minimum at $(\varepsilon_2, \gamma) \sim (0.43, 20°)$. A neutron shell gap at large triaxiality for $N = 97$ is essential for this TSD minimum [98]. When going above $N \sim 97$, rotational bands with similar moments of inertia and aligned angular momentum are predicted to appear in several Hf isotopes, but not necessarily at the

same triaxial deformation. For example, similarities are seen in Figs. 7.3 and 7.4 when comparing the band TSD1 in $^{168}Hf_{96}$ and band-2 in $^{175}Hf_{103}$. However, our UC calculations, as well as previous CRMF calculations [109], show that the rotational properties of the band-2 are reproduced by a band built on a prolate minimum. The calculated quadrupole moment, $Q_t \sim 12$ eb, agrees reasonably well with the preliminary values of $Q_t \sim 13$ eb measured for the band [111]. The same characteristic high-j orbitals as in TSD1 of ^{168}Hf, $\pi i_{13/2}$ and $\nu j_{15/2}$, are occupied. Details of the UC calculations will be published elsewhere [115].

The configuration of band TSD1 is very different from that of the wobbling bands observed in neighboring Lu isotopes, where only one aligned high-j intruder orbital, the $i_{13/2}$ proton, is involved. The zero-phonon bands in Lu isotopes start from spins as low as 6.5 - 12.5 $\hbar$ (rotational frequency $\hbar\omega \sim$ 100 - 200 keV), with excitation energies less than 100 keV above the yrast line at low spins. These bands are strongly populated, e.g., ∼10% and ∼8% relative to yrast band in ^{163}Lu [100] and ^{167}Lu [103], respectively. The wobbling excitations built on these zero-phonon bands are more favored in energy than the TSD bands based on quasiparticle excitations in the TSD minimum which are located at higher energies, e.g., about 1 MeV higher than the zero-phonon band in ^{163}Lu [116]. The band TSD1 in ^{168}Hf is located at much higher spin and excitation energy than the zero-phonon bands in the Lu isotopes. Consequently, its intensity, 0.26(10)% relative to yrast band, is very weak as compared to those of the Lu bands. Furthermore, the calculations suggest that there are several quasiparticle configurations located very close to TSD1, including those shown in Fig. 7.5, which may compete with wobbling excitations more favorably. Therefore, it will be difficult to observe collective wobbling excitations built on band TSD1. A similar situation was suggested to be present for the TSD bands of ^{163}Tm [117]. Band TSD2 could

correspond to one of the four low-lying TSD bands predicted by the UC calculations, considering the fact that the $J^{(2)}$ moments of TSD2 and TSD1 are similar (see Fig. 7.3), and that TSD2 is likely located at a higher excitation energy than TSD1 because it is more weakly populated. If band TSD2 was plotted in Fig. 7.6 with an assumed bandhead spin of 40 $\hbar$ and energy about 2 MeV higher than that of the suggested 33 $\hbar$ bandhead of the band TSD1, band TSD2 would follow the behavior of TSD1 very closely.

7.4 Summary

Decay pathways of previously reported candidates for TSD structures in ^{168}Hf were analyzed. Discrete links were firmly established for band ED. The spin of the lowest level in TSD1 was determined to be 33 $\hbar$ or higher, based on the observed γ-ray coincidence relationships. Detailed rotational properties of the bands were investigated. The results of cranking calculations using the UC code reproduce all experimental observables rather well. The measured properties and the overall agreement with a theoretical analysis provide strong support for an interpretation where band TSD1 is associated with a TSD minimum with $(\varepsilon_2, \gamma) \sim (0.43, 20^\circ)$, involving the $\pi(i_{13/2})^2$ and the $\nu(j_{15/2})$ high-j orbitals. This constitutes a confirmation of the existence of a first TSD band, long-predicted in Hf isotopes. Band ED is likely associated with a near-prolate shape and a deformation slightly enhanced with respect to the normal deformed bands. It is proposed to be built on the $\pi(i_{13/2}h_{9/2}) \otimes \nu(i_{13/2})^2$ configuration. Such ED bands have recently been observed systematically in several heavier Hf isotopes. The results discussed in chapter 7 have been published in a paper [118].

CHAPTER VIII

CONCLUSION AND OUTLOOK

8.1 Summary of Results

This dissertation research comprises a γ-ray spectroscopic investigation of normal deformed (ND) and triaxial strongly deformed (TSD) bands in ^{168}Hf, based on coincidence data acquired in two experiments performed at Argonne National Laboratory (ANL) using Gammasphere.

Seven new normal-deformed rotational bands have been established and six previously known bands have been extended to substantially higher spins. Spin and parity of new levels have been assigned based on the DCO ratio measurements. Furthermore, possible intrinsic configurations were proposed with the help of cranking model calculations. High-spin structures involving up to six quasiparticles (four quasineutrons and two quasiprotons) have been observed. The co-existing coupling schemes in six-quasiparticle structures of band HK-3 involve identical orbitals. This is similar to the first observation of such co-existing coupling schemes reported in ^{166}Hf [87]. Out of the three previously observed candidate TSD bands, band TSD1 has been confirmed as the first TSD band in Hf isotopes. TSD2 has been firmly linked to normal deformed structures and has been renamed to band ED, because of its enhanced deformation, with the aid of "Ultimate Cranker" calculations.

Lifetime measurements using the Doppler-shift Attenuation Method (DSAM) have revealed the transition quadrupole moment of $Q_t \sim 6.4$ eb up to spin $28\hbar$ for the yrast band. This provides a direct measurement of deformation associated with normal deformed shapes in ^{168}Hf.

8.2 Future Directions

The first high-spin triaxial strongly deformed band in Hf isotopes, band TSD1, has been identified, but its discrete decay pathways are not established. Even though Gammasphere is currently the most powerful gamma ray facility in the world for nuclear structure study, its sensitivity pales in detecting very weak γ-rays. There is a major effort to build GRETA (Gamma-Ray Energy Tracking Array) in USA and AGATA (Advanced GAmma Tracking Array) in Europe, which have about 100-1000 times the sensitivity of Gammasphere. Once GRETA or AGATA is operational, even weaker transitions may be detected, and thus the TSD bands in ^{168}Hf can be further studied.

Band ED, similar to bands systematically observed recently in several Hf isotopes, is proposed to be associated with an enhanced deformation relative to the ND bands. This is supported by theoretical calculations, but an experimental lifetime measurement is needed to confirm this presumption.

It should also be emphasized that further investigation of the high-K bands is necessary. The tilted-axis cranking calculations (see, e.g., Ref. [88]) may provide more insights for the quasiparticle configurations involved.

REFERENCES

[1] E.M. Beck, M.A. Deleplanque, R.M. Diamond, R.J. McDonald, F.S. Stephens, J.C. Bacelar, J.E. Draper, Z. Phys. A **327**, 397 (1987).

[2] H. Amro *et al.*, Phys. Lett. B **506**, 39 (2001).

[3] R.Chapman, J.C. Lisle, J.N. Mo, E. Paul, A. Simcock, J.C. Willmott, J.R. Lestlie, H.G. Price, P.M. Walker, J.C. Bacelar, J.D. Garrett, G. B. Hagemann B. Herskind, A. Holm, P.J. Nolan, Phys. Rev. Lett. **51**, 2265 (1983).

[4] K. P. Blume, H. Hübel, M. Murzel, J. Recht, K. Theine, H. Kluge, A. Kuhnert, K. H. Maier, A. Maj, M. Guttermsen and A. P. de Lima, Nucl. Phys. **A464** 445 (1987).

[5] H. Hübel, M. Murzel, E.M. Beck, H. Kludge, A. Kuhnet, K. H. Maier, J. C. Bacelar, M.A. Deleplanque, R.M. Diamond, F.S. Stephens, Z. Phys. A. **329**, 289 (1989).

[6] Y.K. Agarwal, J. Recht, H. Hübel, M. Guttormsen, D.J. Decman, H. Kluge, K.H. Maier, J. Dudek, W. Nazarewicz *et al.*, Nucl. Phys. **A399**, 199 (1983).

[7] G. D. Dracoulis, P. M. Walker, Nucl. Phys. **A330**, 186 (1979).

[8] E. S. Paul, R. chapman, J. C. Lisle, J. N. Mo, S. Sergiwa, J. C. Willmott, A. holm, *et al.*, J. phys. G **11**, L53 (1985).

[9] J.C. Bacelar, M. Diebel, C. Ellegaard, J.D. Garrett, G.B. Hagemann, B. Herskind, A. Holm, C. -X. Yang, J. -Y. Zhang, P.O.Tjøm, J.C.Lisle, Nucl.Phys. **A442**, 509 (1985).

[10] N. Roy, S. Jónsson, H. Ryde, W. Walús, J. J. Gaardhøje, J. D. Garret, G. B. Hagemann, B. Herskind, Nucl. Phys. **A382**, 125 (1982).

[11] J. Kownack, J. D. Garrett, J. J. Gaardhøje, G. B. Hagemann, B. Herskind, S. Jónsson, N. Roy,H. Ryde, W. Walús, Nucl. Phys. **A394**, 269 (1983).

[12] J. Recht, Y.K. Agarwal, K.P. Blume, M. Guttormsen, H. Hübel, H. Kluge, K.H. Maier, A. Maj, N. Roy, D.J. Decman, J. Dudek, W. Nazarewicz, Nucl. Phys. **A440**, 366 (1985).

[13] R. A. Bark, G. D. Dracoulis, A.E. Stuchbery, Nucl. Phys. **A514**, 503 (1990).

[14] P. E. Hodgson, E. Gadioli, and E. Gadioli Erba, Introductory Nuclear Physics, Clarendon Press, Oxford (1997).

[15] W. Pauli, Naturwiss **12**, 741 (1924).

[16] M.G. Mayer, Phys. Rev. **76**, 185 (1949).

[17] O. Haxel, T.H.D. Jensen, and H.E. Suess, Phys. Rev. **75**, 1766 (1949).

[18] S.M. Polikanov, A. Druin, V.A. Karnaukhov, V.L. Mikheev, A.A. Pleve, N.K. Skobelev, G.M. Ter-Akopyan, and V.A. Fomichev, Sov. Phys. JETP **15**, 1016 (1962).

[19] H.J. Specht, J. Weber, E. Konecny, and D. Heunemann, Phys. Lett. B **41**, 43 (1972).

[20] C.G. Andersson, S.E. Larsson, G. Leander, P. Möller, S.G. Nilsson, I. Ragnarsson, S. Åberg, R. Bengtsson, J. Dudek, B. Nerlo-Pomarska, K. Pomorski and Z. Szymanski, Nucl. Phys. A **268**, 205 (1976).

[21] I. Ragnarsson *et al.*, Nucl. Phys. A **347**, 287 (1980).

[22] P.J. Twin *et al.*, Nucl. Phys. A **409**, 343 (1983).

[23] B.M. Nyako, J.R. Cresswell, P.D. Forsyth, D. Howe, P.J. Nolan, M.A. Riley, J.F. Sharpey-Schafer, J. Simpson, N.J. Ward, and P.J. Twin, Phys. Rev. Lett. **52**, 507 (1984).

[24] P. Ring and P. Schuck, The Nuclear Many-Body Problem, Springer-Verlag Publishers, New York (1980).

[25] M.A. Preston and R.K. Bhaduri, *Structure of the Nucleus*, Addison-Wesley Publishing Company Inc., Reading, Massachusetts (1975).

[26] J.M. Eisenberg and W. Ereiner, *Nuclear Models*, North Holland, Amsterdam (1970).

[27] N. Bohr and N.A. Wheeler, Phys. Rev. C **56**, 426 (1939).

[28] H.A. Bether and R.F. Bacher, Rev. Mod. Phys. **8**, 82 (1936).

[29] C.F. Von Weizsacker, Zeit. fur Phys. **96**, 431 (1935).

[30] W.D. Myers and W.J. Swiatecki, Nucl. Phys. **81**, 1 (1966).

[31] R.F. Casten, *Nuclear Structure from a Simple Perspective*, Oxford University Press, New York (2000).

[32] M.G. Mayer and J.H.D. Jensen, *Elementary Theory of Nuclear Shell Structure*, John Wiley and Sons, Inc., New York (1955).

[33] S.G. Nilsson, Dan. Mat. -Fys. Medd. **29**, No. 16 (1955).

[34] B.R. Mottelson and S.G. Nilsson, Phys. Rev. **29**, 1615 (1955).

[35] J. Dudek, A. Majhofer, J. Skalski, T. Werner, S. Cwiok, and W. Nazarewicz, J. Phys. G **5**, 1359 (1987).

[36] S. Cwiok, J. Dudek, W. Nazarewicz, J. Skalski, and T. Werner, Comp. Phys. Comm. **46**, 379 (1987).

[37] R. Bengtsson, J. Dudek, W. Nazarewicz, and P. Olanders, Physica Scripta **39**, 196 (1989).

[38] S.G. Nilsson and I. Ragnarsson, *Shapes and Shells in Nuclear Structure*, Cambridge University Press, Cambridge (1995).

[39] Yang Sun, Ani Aprahmaian, Jing-ye Zhang, and Ching-Tsai Lee, Phys. Rev. C **68**, 061301(R) (2003).

[40] R.F. Casten, Nucl. Phys. A **443**, 1 (1985).

[41] J. Bardeen, L.N. Cooper, and J.R. Schrieffer, Phys. Rev. **108**, 1175 (1957).

[42] A. Bohr, B.R. Mottelson, and D. Pines, Phys. Rev. **110**, 936 (1958).

[43] D.J. Hartley, Ph.D. thesis, Florida State University (1998).

[44] W. Gelletly. The Nuclear Whirling, *Nuclear Physics News*, 2(1), 1992. 2.1, 3.7.5.

[45] B.R. Mottelson and J.G. Valatin. Effect of Nuclear Rotation on the Pairing Correlation, *Physical Review Letters*, 5:511-512, 1960. 3.7.5.

[46] A. Johnson, H. Ryde and J. Sztarkier. Evidence for a "Singularity" in the Nuclear Rotational Band Structure. *Physics Letters* B, 34:605-608, 1971. 12, 3.76.

[47] B. Olaniyi, A. Shor, S.C. Cheng, G. Dugan, and C.S. Wu, Nucl. Phys. A **403**, 572 (1983).

[48] R.V. Jolos, P. von Brentano, A. Dewald, and N. Pietralla, Phys. Rev. C **72**, 024310 (2005).

[49] P.J. Nolan and J.F. Sharpey-Schafer, Rep. Prog. Phys. **42** (1979).

[50] J. Lindhard, M. Scharff, and H.E. Schiott, K. Dan. Vidensk. Selsk. Mat. Fys. Medd. **33**, No. 10 (1963).

[51] K.B. Winterbon, Can. J. Ohys. **46**, 2429 (1968).

[52] A.E. Blaugrund, Nucl. Phys. **88**, 501 (1966).

[53] W.M. Currie, Nucl. Inst. and Meths. **73**, 173 (1969).

[54] L.C. Northcliffe and R.F. Schilling, Nucl. Data Tables **7**, 256 (1970).

[55] T.E. Pierce and M. Blann, Phys. Rev. **173**, 390 (1968).

[56] D. Ward et al., Atomic Energy of Canada Ltd. Rept. AECL-4914 (1975).

[57] J.F. Ziegler and W.K. Chu, Atomic Data and Nucl. Data Tables **13**, 463 (1974).

[58] J. C. Wells and N. R. Johnson, LINESHAPE: A computer program for Doppler-broaded lineshape analysis, Oak Ridge National Laboratory Physics Division Progress Report for period ending September 30, 1991, ORNL-6689 (1991) P. 44.

[59] J.C. Bacelar, A. Holm, R.M. Diamond, E.M. Beck, M.A. Deleplanque, J. Draper, B. Herskind, F.S. Stephens *et al.*, Phys. Rev. Lett. **57**, 3019 (1986).

[60] J. Gascon, C. H. Yu, G. B. Hagemann, M. C. Carpater, J. M. Espino, Y. Iwata, T. Komatsubara, J. Nyberg, S. Ogaza, G. Sletten, P. O. Tjøm, and D. C. Radford, Nucl. Phys. **A513**, 344 (1990).

[61] F. James and M. Roos, Comput. Phys. Commun. **10**, 343 (1975).

[62] J. A. Nelder and R. Mead, Comput. J. **7**, 308, (1965).

[63] R. Fletcher, comput. J., **13**, 317 (1970).

[64] R. Fletcher and M. J. D. Powell, Comput. J. **6**, 163 (1963).

[65] W. B. Gao, I. Y. Lee, C. Baktash, R. Wyss, J. H. Hamilton, C. M. Steele, C. H. Yu, N. R. Johnson, F. K. McGowan *et al.*, Phys. Rev. C **44**, 1380 (1991).

[66] D. M. Cullen, A. T. Reed, D. E. Appelbe, A. N. Wilson, E. S. Paul, R. M. Clark, P. Fallon, I. Y. Lee, A. O. Macchiavelli, R. W. MacLeod *et al.*, Nucl. Phys. **A638**, 662 (1998).

[67] D. M. Cullen, A. T. Reed, D. E. Appelbe, A. N. Wilson, E. S. Paul, M. H. Bergström, J. F. Sharpey-Schafer, C. Baktash, I. Frosch, I. Y. Lee, A. O. Macchiavelli, R. W. MacLeod, D. Prevost, Ch. Theisen, D. Curien *et al.*, Nucl. Phys. A **673**, 3 (2000).

[68] T. K. Alexander and J. S. Forster, Adv. Nucl. Phys. **10**, 197 (1979).

[69] R.W. Laird, Ph.D. thesis, Florida State University (2000).

[70] H. Ejiri and M.J.A. de Voigt, *Gamma-Ray and Electron Spectroscopy in Nuclear Physics*, Oxford Science Publication, Oxford (1989).

[71] http://fsunuc.physics.fsu.edu/∼riley/gamma/.

[72] R. Brock, Ed., *Heavy ion Collisions*, Vol.**2**, North Holland Publishing Company; Amsterdam (1980).

[73] I. Y. Lee, Nucl. Phys. A **520**, 641 (1990).

[74] D.C. Radford, Nucl. Inst. and Meth. A **361**, 306 (1995).

[75] D.C. Radford, Nucl. Inst. and Meth. A **361**, 297 (1995).

[76] K. Starosta, D.B. Fossan, T. Koike, C. Vaman, D.C. Radford, C.J. Chiara, Nucl. Inst. and Meth. A **515**, 771 (2003).

[77] G. Palameta and J.C. Waddington, Nucl. Inst. and Meth. A **234**, 476 (1985).

[78] J.C. Bacelar, A. Holm, R.M. Diamond, E.M. Beck, M.A. Deleplanque, J. Draper, B. Herskind, F.S. Stephens, Phys. Rev. Lett. **57**, 3019 (1986).

[79] R. Bengtsson, www.matfys/lth/se/ ragnar/ultimate.html.

[80] T. Bengtsson, Nucl. Phys. A **512**, 124 (1990); A **496** 56 (1989).

[81] T. Bengtsson and I. Ragnarsson, Nucl. Phys. A **436**, 14 (1985).

[82] R. Bengtsson and S. Frauendorf, Nucl. Phys. A **314**, 27 (1979).

[83] W. Nazarewicz, J. Dudek, R. Bengtsson, T. Bengtsson and I. Ragnarsson, Nucl. Phys. A **435**, 397 (1985).

[84] E.M.Beck, J.C.Bacelar, M.A.Deleplanque, R.M.Diamond, F.S.Stephens, J.E.Draper, B.Herskind, A.Holm, P.O. TjØm, Nucl.Phys. **A464**, 472 (1987).

[85] S. Jonsson, N. Roy, H. Ryde, W. Walus, J. Kownacki, J. D. Garrett, G. B. Hagemann, B. Herskind, R. Bengtsson, S. Åberg, Nucl. Phys. **A449**, 537 (1986).

[86] M.B. Smith, G.J. Campbell, R. Chapman, P.O. Tjøm, R.A. Bark, G.B. Hagemann, N. Keeley, D.J. Middleton, H. Ryde, K.-M. Spoh, Eur. Phys. J. A **6**, 37 (1999).

[87] D. Ringkjøbing Jensen, J. Domscheit, G.B. Hagemann, M. Bergstrøm, B. Herskind, B.S. Nielsen, G. Sletten, P.G. Varmette, S. Törmänen, H. Hübel, W. Ma, A. Bracco, F. Camera, F. Demaria, S. Frattini, B. Million, D. Napoli, A. Maj, B.M. Nyakó, D.T. Joss, M. Aiche, Eur. Phys. J. **A 8**, 165-176 (2000).

[88] J.R.B. Oliveria, S. Frauendorf, M.A. Deleplanque, B. Cederwall, R.M. Diamond, A.O. Macchiavelli, F.S. Stephens, J. Burder, J.E. Draper, C. Duyar, E. Rubel, J.A. Becker, E.A. Henry, M.J. Brinkman, A. Kuhnert, M.A. Stoyer, T.F. Wang, Phys. Rev. C **50**, 3 (1994).

[89] D.H. Smalley, A.G. Smith, S.Y. Araddad, C.W. Beausang, R. Chapman, J. Copnell, A. Fitzpatrick, S.J. Freeman, S. Leoni, F. Lidén, J.C. Lisle, J.F. Sharpey-Schafer, J. Simpson, J.P. Sweeney, D.M. Thompson, W. Urban, S.J. Warburton, J. Wrzesinski, J. Phys. G: Nucl. Part. Phys. **22** (1996) 1411-1420.

[90] F. Dönau, Nucl. Phys. A **471**, 469 (1987).

[91] B.E. Chi, Nucl. Phys. A **83**, 97 (1966).

[92] A. Bohr, B.R. Mottelson, *Nuclear Structure*, Vol. **2** (W.A. Benjamin, New York, 1975).

[93] K.A. Schmidt, M.Bergström, G.B. Hagemann, B. Herskind, G. Sletten, P.G. Varmette, J. Domscheit, H. Hübel, S.W. Ødegård, S. Frattini, A. Bracco, B. Million, M.P. Carpenter, R.V.F. Janssens, T.L. Khoo, T. Lauritsen, C.J. Lister, S. Siem, I. Wiedenhöver, D.J. Hartley, L.L. Riedinger, A. Maj, W.C. Ma, R. Terry, Eur. Phys. J. A **12**, 15 (2001).

[94] C.J. Pearson, P.M. Walker, C.S. Purry, G.D. Dracoulis, S. Bayer, A.P. Byrne, T. Kibédi, F.G. Kondev, T. Shizuma, R.A. Bark, G. Sletten, S. Frauendorf, Phys. Rev. Lett. **79**, 605 (1997).

[95] I. Ragnarsson, Phy. Rev. Lett. **62**, 2084 (1989).

[96] S. Åberg, Nucl. Phys. A **520**, 35c (1990).

[97] H. Schnack-Petersen, R. Bengtsson, R. A. Bark, P. Bosetti, A. Brockstedt, H. Carlsson, L. P. Ekström, G. B. Hagemann, B. Herskind, F. Ingebretsen *et al.*, Nucl. Phys. A **594**, 175 (1995).

[98] R. Bengtsson and H. Ryde, Eur. Phys. J. A **22**, 355 (2004).

[99] A. Bohr and B. R. Mottelson, Nuclear Structure, Vol. II, Benjamin, New York, 1975.

[100] S. Ødegård, G. B. Hagemann, D. R. Jensen, M. Bergström, B. Herskind, G. Sletten, S. Törmänen, J. N. Wilson, P. O. Tjøm, I. Hamamoto *et al.*, Phys. Rev. Lett. **86**, 5866 (2001).

[101] D. R. Jensen, G. B. Hagemann, I. Hamamoto, S. W. Ødegård, B. Herskind, G. Sletten, J. N. Wilson, K. Spohr, H. Hübel, P. Bringel *et al.*, Phys. Rev. Lett. **89**, 142503 (2002), and references therein.

[102] G. Schönwaßer, H. Hübel, G. B. Hagemann, P. Bednarczyk, G. Benzoni, A. Bracco, P. Bringel, R. Chapman, D. Curien, J. Domscheit *et al.*, Phys. Lett. **B552**, 9 (2003).

[103] H. Amro, W. C. Ma, G. B. Hagemann, R. M. Diamond, J. Domscheit, P. Fallon, A. Görgen, B. Herskind, H. Hübel, D. R. Jensen *et al.*, Phys. Lett. **B553**, 197 (2003).

[104] P. Bringel, G. B. Hagemann, H. Hübel, A. Al-khatib, P. Bednarczyk, A. Bürger, D. Curien, G. Gangopadhyay, B. Herskind, D. R. Jensen *et al.*, Eur. Phys. J. A **24**, 167 (2005).

[105] I. Hamamoto, Phys. Rev. C **65**, 044305 (2002).

[106] I. Hamamoto and G. B Hagemann, Phys. Rev. C **67**, 014319 (2003).

[107] M. Matsuzaki, Y. R. Shimizu, and K. Matsuyanagi, Phys. Rev. C **69**, 034325 (2004).

[108] A. Neußer-Neffgen, H. Hübel, P. Bringel, J. Domscheit, E. Mergel, N. Nenoff, A. K. Singh, G. B. Hagemann, D. R. Jensen, S. Bhattacharya *et al.*, Phys. Rev. C **73**, 034309 (2006).

[109] Y. C. Zhang, W. C. Ma, A. V. Afanasjev, G. B. Hagemann, J. Begnaud, M. P. Carpenter, P. Chowdhury, D. M. Cullen, M. K. Djongolov, D. J. Hartley, *et al.*, Phys. Rev. C **76**, 064321 (2007).

[110] D. J. Hartley, M. K. Djongolov, L. L. Riedinger, G. B. Hagemann, R. V. F. Janssens, F. G. Kondev, E. F. Moore, M. A. Riley, A. Aguilar, C. R. Bingham *et al.*, Phys. Lett. B**608**, 31 (2005).

[111] D. T. Scholes, D. M. Cullen, F. G. Kondev, R. V. F. Janssens, M. P. Carpenter, D. J. Hartley, M. K. Djongolov, G. Sletten, G. B. Hagemann, C. Wheldon *et al.*, Phys. Rev. C **70**, 054314 (2004).

[112] R. B. Yadav, W. C. Ma, G. B. Hagemann, H. Amro, P. G. Varmette, B. Herskind, G. Sletten, J. N. Wilson, *et al.*, to be published.

[113] T. Lauritsen, M. P. Carpenter, T. Døssing, P. Fallon, B. Herskind, R. V. F. Janssens, D. G. Jankins, T. L. Khoo, F. G. Kondev, A. Lopez-Martens *et al.*, Phys. Rev. Lett. **88**, 042501 (2002), and references therein.

[114] A. Lopez-Martens, F. Hanachi, A. Korichi, C. Schück, E. Gueorguieva, Ch. Vieu, B. Hass, R. Lucas, A. Astier, G. Baldsiefen, *et al.*, Phys. Lett. B **380**, 18 (1996).

[115] R. Bengtsson and H. Ryde, to be published.

[116] D. R. Jensen, G. B. Hagemann, I. Hamamoto, B. Herskind, G. Sletten, J. N. Wilson, S. W. Ødegård, K. Spohr, H. Hübel, P. Bringel *et al.*, Eur. Phys. J. A **19**, (2004) 173.

[117] N. S. Pattabiraman, Y. Gu, S. Frauendorf, U. Garg, T. Li, B. K. Nayak, X. Wang, S. Zhu, S. S. Ghugre, R. V. F. Janssens *et al.*, Phys. Lett. **B647**, 243 (2007).

[118] R. B. Yadav, W. C. Ma, G. B. Hagemann, R. Bengtsson, H. Ryde, H. Amro, A. Bracco, M. P. Carpenter, J. Domscheit, S. Frattini, D. J. Hartley, B. Herskind, H. Hübel, R. V. F. Janssens, T. L. Khoo, F. G. Kondev, T. Lauritsen, C. J. Lister, B. Million, S. Ødegård, L. L. Riedinger, K. A. Schmidt, S. Siem, G. Sletten, P. G. Varmette, J. N. Wilson, and Y. C. Zhang, Phys. Rev. C **78**, 044316 (2008).

APPENDIX A

THE PROCEDURE FOR DCO RATIO MEASUREMENT

Introduction

Theoretically, we have defined how to calculate the DCO ratio in Chapter II. In this appendix, we present the procedures to calculate it practically. There are four programs (matedco, slice, subbgmat, m2mat and gf3) that are used.

Steps:

(1) A gate list is made by selecting strong and clean gating transitions: the matrices used for the DCO ratio are single-gated matrices.

(2) The program "matedco" is used to scan the database and to build the matrix "dcomat.mat". An event is placed in the matrix if there is a coincidence between a detector in group 'x', including detectors in rings 2,3,15,16 and 17, and a detector in group 'y', including detectors in rings 5, 6, 7, 8, 9, 10, 11, 12 and 13.

(3) The program "slice" is used to obtain the total projection spectra on the two axes. The program "gf3" is used to read the total projection spectra and then the command "bg" is used to generate the smooth background spectra.

(4) The program "subbgmat" is used to subtract the smooth matrix background to get the background-subtracted matrices. While running this program, total projection spectra and smooth one-dimension background spectra are required as inputs. In addition, a unit efficiency spectrum will be required as well.

(5) Based on background-subtracted matrices and the output factor from "subbgmat", the program "m2mat" is used to multiply matrices by this output factor:

m2mat -o output.mat input.mat -s scalefactor

(6) The commands "sl" and "wi" in "gf3" are used to generate a gate list (the .win file).

(7) The program "slice" is run, taking the "*.win" file as input, to slice the matrix to

obtain the final spectra. Based on these final spectra, the areas of peaks of interests are found.

(8) Finally, the ratio of the peak areas obtained from the x- and y- directions is calculated.

APPENDIX B

THE PROCEDURE FOR THE PLOT OF ALIGNMENTS, MOMENT OF INERTIA, ROUTHIANS ETC.

Introduction

In this appendix, we will explain the procedure for plotting the graphs for alignment, moment of inertia, routhians etc. These quantities are theoretically defined in Chapter II.

Steps:

(1) Run the program dixie_gls.

(2) Give the .gls file.

(3) Enter the appropriate values for Harris parameters (for example, 35, 40).

(4) Use the commands xa, xm, xe, xr etc to get the displayed plots for alignment, moment of inertia, energy and routhian respectively.

(4) Use the command wp to write a dixie-type (.pdc) file.

(5) Stop and exit the program using the command st.

(6) Run the program plot to obtain .psc and .psg files.

(7) Run the program pedit to edit the plot. We can add or delete any text using this program.

(8) Finally, run the program plot2ps to obtain the .ps file for the plot.

(9) Use the command ggv to view the plot.

APPENDIX C

LINESHAPE: A COMPUTER PROGRAM FOR DOPPLER-BROADENED LINESHAPE LIFETIME ANALYSIS

Introduction

A set of general-purpose computer programs for analysis of Doppler-broadened gamma-ray lineshapes for deducing nuclear lifetimes has been developed at ORNL incorporating several existing programs. The following is a brief description on how to run the program "LINESHAPE".

Getting Started

1. Run the program DECHIST_OR. It simulates by Monte Carlo techniques the slowing-down process of the recoils in the target and in the backing. It reads input data from a data file, filename.DAT, and produces a list file, filename.LIS, and a history file, filename.HIS, that contains the velocity and direction of the recoils at every time step for each simulated recoil. The .LIS file also contains some statistical information about the recoil histories. These two output files are given the same filename as the .DAT file.

The following input information is needed: the Z and A of the projectile, target, backing, and recoil nucleus, the densities of the target and backing in g/cm^3, the target thickness in mg/cm^2, the angle between the target and beam in degrees, and the beam energy in MeV. These may be read from a .DAT file or entered interactively in response to the program's questions (and saved in a .DAT file). One must also give the time step in ps, an integer seed to start the random number generator, and the number of recoil histories desired. Suggested values: for the time step, 0.01 times the shortest expected life-time; and 3000 or more histories. A disk quota of 100,000 blocks may be necessary.

Stopping powers are generated internally from one of several models. Your choice

of models can be selected from a menu. A file STOPP.OUT is generated which contains a tabulation of stopping powers as a function of ion energy for (1) recoil in target, (2) recoil in backing, and (3) projectile in target.

2. Run the program HISTAVER_OR. It takes the output from the .LIS file and .HIS file generated by DECHIST_OR and produces another .LIS file and .HIS file containing, for each time step, the velocity profile as seen by a detector at a certain angle. You will need to run this program once for every angle used in the analysis, and for each of these a .LIS and .HIS file will be generated. The program requests a filename for these output files. It should be different from the filename of the input .LIS and .HIS files so that these will not be overwritten.

The following input information is needed: the target-detector distance, the detector radius, the detector angle theta in degrees, the number of detectors at that angle, and, for each detector, its relative efficiency and angle phi.

3. Select the level scheme which contains the transitions you wish to analyze. Obtain energies for the E2 transitions between these levels. Number the levels consecutively starting with the lowest. If you are analyzing two coupled bands, number the levels in order of increasing energy, which means that one band will have even numbers and the other odd. Determine the spin of the lowest level and the K value of the band.

For coupled bands, determine the M1/E2 branching ratios out of each level. These must be greater than zero and less than one. For a single band, set all of the branching ratios equal to 1.0. This is how the LINESHAPE tells which case to analyze.

Determine the intensity of the side-feeding (in relative units) into each level included in the analysis. This should be obtained, if possible, from spectroscopic data for the same reaction at the same beam energy. Choose the side-feeding model for

each level, either a rotational band or a cascade whose transitions will have independently varied lifetimes. For rotational bands, choose the number of transitions in the bands (from 1 to 6), and the moment of inertia ($I/\hbar^2$ in 1/MeV). A value of 65/MeV is typical. These must be the same for all rotational bands. For independently varied side-feeders, the number of transitions in the cascade (from 1 to 5) and the initial lifetimes (which must all be different) must be specified for each level being fed. The number of transitions in the feeding cascades may be different for different levels being fed. It is possible to use rotational band feeding for some levels and independently varied cascade feeding for others.

4. Select the spectra that you will use for the analysis, one per angle. Including the 90 degree angle in the analysis is recommended, as it helps to identify contaminants. Gates can be summed. It is also possible to use different spectra for different transitions. Obtain a linear energy calibration (slope (in MeV/ch) and intercept (in MeV)). All spectra must have the same energy calibration.

For each data spectrum, construct an error spectrum which contains, for each channel, the SQUARE of the error in the corresponding data channel. If these errors are not accurate, the error results of MINOS analysis will not be valid. For a singles spectrum, the spectrum itself may serve as the error spectrum. This is the default if no error spectrum is provided. For a gate spectrum from which a (weighted) background spectrum has been subtracted, the error spectrum may be generated by adding the original raw gate spectrum to the (weighted) background spectrum.

LINESHAPE can read spectra in the (ORNL) .SPK format and in the (NBI) .SPE format. A filename with no extension is assumed to be .SPK.

For each gamma-ray transition you wish to analyze, select the low-channel and high-channel limits of a 'window' which contains the Doppler-broadened photopeak

and sufficient channels on each side to fit a linear background. Making the window wider than necessary will increase the running time and dilute the normalized chi-square. Determine the FWHM (in channels) for stopped (unbroadened) peaks in the window for each angle.

If two or more Doppler-broadened photopeaks overlap, they must be fitted together in the same window. To do this you must use the same low- and high- channel limits for each transition in the window. It is permissible, however, for two different windows to overlap in the background area as long as the peaks being fitted to not overlap.

If there are any contaminant peaks in the window, determine their centroids accurately, and the program will include them in the fit. It can handle up to eight peaks per window. If any of the contaminant peaks do not overlap the peak whose lineshape is being fitted, they can be eliminated from the fit by specifying regions to be excluded. The FWHM of contaminant peaks may be different from that of the broadened photopeak.

5. Obtain an .eff file for the efficiency calibration. You will have to divide each spectrum by this file.

6. Run LINESHAPE. Use the SETUP command to setup the entire level scheme. Supply the information as the program asks for it. Save (DUMP) that setup. Next, use the CALCULATE command. It creates shape-versus-time matrices for each of the gamma-rays included in the analysis for which there is data. Save those shapes with DU/S (dump/shape). You can look at those shapes on a graphics terminal with the DS command.

7. Start the least_squares fit. Start from the top, using the SW (Select Window) command to exclude the lower levels from the analysis, and then move down the

band fitting successive windows in turn. It is recommended that you save your fitted parameters after each step to avoid losing results if there is a computer or program malfunction. To minimize disk space usage, you can over- write previous dump files, since all parameters are saved each time, not just the ones currently being fitted.

LINESHAPE contains three minimization routines from the program MINUIT developed at CERN. These are SEEK, SIMPLEX, and MIGRAD. SEEK searches randomly over a region around the starting values of the parameters, SIMPLEX moves in quickly to the region of the minimum and MIGRAD converges very closely to the minimum when starting not too far away. The recommended fitting procedure is to call SEEK if the starting values of the parameters are only "wild guesses", then call SIMPLEX and MIGRAD in that order. If the starting values of the parameters are reasonable, then start with SIMPLEX followed by MIGRAD.

You can observe the quality of the fit on a graphics terminal with the DD command, which displays the data, followed by the DF command, which overlays the fit. You can also observe the decay curves with the DC command.

Using ALT (Alter) you can change the values of parameters and observe the effect on the fit, on the decay curves, etc.

8. At the initial stage of the analysis, you should try to obtain the best values of the peak widths for each window, and also the best positions of the contaminant peaks ("best" meaning the values that give the lowest chi-squares). These parameters can be varied with the ALT command but not least-squares fitted.

9. After obtaining the best fits for each window separately, you should fix the window parameters (NORM, A, B, and PA) and vary Q and TS and/or QS for several adjacent levels; perhaps for the entire level scheme. The command FW or FIX/WIN is useful for fixing all window parameters.

10. The errors on the parameters after MIGRAD has converged are derived from the covariance matrix, and should be reasonably good if the parameters are not strongly correlated. However, since the Q and TS and/or QS for a given transition are probably correlated (e.g. one could increase and the other decrease without changing chi-square much), one should call the MINOS error analysis routine only after obtaining the best fits to all of the parameters. When running MINOS, all of the Q and TS and/or QS parameters above the state of interest should be free.

APPENDIX D

BIOGRAPHICAL SKETCH

Ram Babu Yadav

The author was born in a farmer family on September 20, 1974 at Janakpur Dham, Nepal which is also known as the birth place of goddess "Sita" and the capital of the ancient state of Mithila, as described in Hindu holy books. After completing two year undergraduate degree from the R.R.M campus in 1993, the author moved to Kathmandu, the capital of Nepal from where he finished his B.Sc. degree at Tri-Chandra college in 1996. In 1997, he enrolled in M.Sc. program at the Central Department of Physics, University Campus (Tribhuvan University) at Kirtipur located southwest of Kathmandu. After graduating in 1999, the author was offered a lecturer position to teach electronics at the same department because of his excellent grade in this course. He had taught both lab and theory courses to M.Sc. students for three years. Starting from Spring 2003, the author enrolled in the Ph.D. program at Mississippi State University where he had the privilege of working closely with Professor Wenchao Ma while engaging in nuclear physics research. Recently, he has been rewarded with outstanding Ph.D. student performance award (2009) from Sigma Xi Scientific Research Society, MSU.